1-1-2017

Characterizing Coastal Marsh Groundwater Hydrology with Multichannel Electrical Resistivity Tomography

Matthew R. Kestner
Coastal Carolina University

Characterizing Coastal Marsh Groundwater Hydrology with Multichannel Electrical Resistivity Tomography

Matthew R. Kestner

Submitted in Partial Fulfillment of the
Requirements for the Degree of Master of Science in
Coastal Marine and Wetland Studies in the
College of Science
Coastal Carolina University
Summer 2017

Advisor:
Dr. Richard F. Viso
Committee Members:
Dr. Jenna C. Hill
Dr. Richard N. Peterson

Acknowledgements

I would like to thank Dr. Rich Viso, for giving me the opportunity to conduct research under him. Without your guidance and input, I would not have developed into the scientist I am today. I would also like to thank Dr. Jenna Hill and Dr. Rick Peterson for being on my committee; your input and ideas were greatly appreciated. Thank you to all the faculty and staff at Coastal Carolina University for giving me the opportunity to expand my knowledge and for facilitating the incredible experiences that I would never have had the opportunity or resources for.

To my Mom, I would not be where I am today without your strength, perseverance, and motivation as a mother to guide and encourage me to do what I love. Your unconditional love and support, has been invaluable. To the rest of my friends and family, thank you for your constant support and encouragement.

To my fellow colleagues, thank you for waking up at all hours of the night to stand out in a salt marsh for 12+ hours at a time. Without your willingness to get attacked by bugs, get muddy, freeze or sweat to death, I could have never managed to collect the data needed for this research. I think we all have a newfound respect for how harsh Waties Island can be.

Lastly I would like to thank Waties Island for showing me the beauty and harshness of coastal environments.

Table of Contents

List of Tables

List of Figures

Figure 9: ArcGIS satellite view of the creek channel and marsh. The RTK GPS points are shown in 2-meter increments to show what electrode number is correspondent with that measuring point. The hand auger and vibracore locations are also located adjacent to the resistivity transect. Also note the white line indicates the channel boundaries while the red lines indicate the extent of the Spartina alterniflora vegetation.

Figure 10: Image A is the processed data for 151030I_spring utilizing the .trn file. The maximum resistivity value is 4.8 Ω-m, which is well similar to the laboratory observed resistivities. Image B is the processed data for151030I_spring utilizing the .uwt file. Its maximum resistivity value is 1208.0 Ω-m, which falls well outside the range that has been physically observed in laboratory experiments. Also note the statistical difference in the processed figures, resulting in the use of only the terrain and not the water layer to give the most statistically accurate representation of field conditions.

Figure 11: Temperatures inverse effect on resistivity. As temperature increases the resistivity of a material decreases.

Figure 12: Synthetic Models that where developed using AGI EarthImager software to determine what type of artifacts would be developed having a 1 Ω-m background resistivity and 0.3 Ω-m hyporheic zone. The processed data reveals similarities in artifacts located in the subsurface near the creek banks, high and low resistivity bodies.

Figure 13: Typical processed Electrical Resistivity data including the Measured Apparent Resistivity Psuedosection at the top followed by the Calculated Apparent Resistivity Psuedosection in the middle, with the interpreted geological cross section, Inverted Resistivity Section at the bottom.

Figure 14: The numerical mesh generation by QPS Fledermaus DMagic.

Figure 15: Screenshot of the numerically generated mesh imported from Fledermaus, with the accompanying electrode surface position from the RTK-GPS data.

Figure 16: ArcGIS 2-color contour surround the 0.604 Ω-m line that separates the maximum extent of the hyporheic zone and ambient background noise.

1. Introduction

Coastal hydrology has grown rapidly in recent years in response to resource demands and recognition of the broad influence of submarine groundwater discharge in the coastal system (e.g. Capone and Bautista, 1985; Simmons, 1992; Moore, 1996; Shaw et al., 1998; Wilson, 2005; Burnett et al., 2006; Swarzenski et al., 2006; Santos et al., 2009; Peterson et al., 2010). Salt marshes offer a host of ecosystem services such as natural storm buffers, a natural filtration system, habitat and nurseries for many different organisms (Boesch and Turner, 1984; Cullinan et al., 2004; Gedman et al., 2009). Salt marsh ecosystems also play a substantial role in climate change studies cycling carbon, nitrogen, and sulfur (Cai and Wang, 1998; Cullinan et al., 2004; Wang and Cai, 2004; Cai, 2011), and are a source of a greenhouse gas, methane (Bartlett et al., 1987).

Examination of salt marsh hydrology leads to a robust understanding of the complex interconnected processes (e.g. nutrient cycling) and redox and salinity gradients that occur. Tidally driven groundwater flow drives significant solute exchange between marsh sediments and tidal creek channels in coastal environments (King et al., 1982; Moore, 1999; Moore et al., 2002; Taniguchi, 2002). This solute exchange can influence salinity gradients, nutrient concentrations, and redox conditions within the marsh sediments and surface waters, playing a vital role in marsh ecology (Wilson and Gardner, 2006). Near surface pore waters are highly enriched in nutrients compared to surface waters in the coastal salt marsh environment and may, therefore, have a disproportionately (in terms of volume) large effect on biogeochemical processes (Whiting and Childers, 1989; Gleeson et al., 2013). Creek channel seepage alone could provide enough sulfate and oxygen for decomposition of below-ground Spartina

production and the removal of dissolved sulfide and remineralized nitrogen and phosphorous in near creek bank sediment (Gardner, 2005). To accurately estimate material and nutrient fluxes within wetlands, a comprehensive understanding of hydrological transport processes is needed (Harvey et al., 1987).

Salt marsh hydrology has many understudied details that can lead to a better understanding of biogeochemical interactions. Aspects of groundwater-surface water exchange, hyporheic zone processes, large scale groundwater movement (from upland to ocean), and localized groundwater movement are poorly constrained and make generalizations difficult due to localized and complex interactions (Figure 1). Fortunately, coastal hydrology can be studied through various methodologies including numerical modeling, direct observation (geochemical, piezometers, monitoring wells, water quality stations), and indirect observation (geophysical imaging).

Recent modeling studies have focused on near-channel marsh platform and creek bank interaction with tidally-driven groundwater flow and the resulting solute exchange between pore water and surface water (Harvey et al., 1987; Gardner, 2005; Wilson and Gardner, 2006; Moffett et al., 2012; Wilson and Morris, 2012; Xin et al., 2013). A simulation by Harvey et al., (1987) demonstrated that the main driver for replacing water discharged at the creek bank was vertical infiltration from tidal flooding (66%) while the remainder came from groundwater located within the marsh interior (31%) and horizontal recharge at the creek bank (3%). They concluded that change in marsh elevation was the primary driver of pore water discharge at the creek bank, and a higher elevation would lead to a more rapid turnover of pore water (Harvey et al., 1987). Gardner (2005) confirmed that two-thirds of total seepage over a tidal cycle came from the creek bank,

while the other one-third came from the channel bottom. Numerical modeling studies have further demonstrated that without large-scale permeable groundwater pathways and inundation of the marsh platform, significant pore water exchange is limited to the creek bank (Wilson and Gardner, 2006).

The use of naturally occurring geochemical tracers also has helped place constraints on determining volumetric discharge of nutrient rich submarine groundwater to coastal environments (e.g. Schwartz, 2001; Santos et al., 2009; Peterson et al., 2010). Peterson et al. (2010) used radon-222 to assess tidally-influenced rivers that discharged into Indian River Lagoon, Florida and determine the amount of groundwater discharging from each river. Focusing on the Sebastian River system, a box model determined that there is an increase of 1 - 2 orders of magnitude from a dry period to a wet period in the amount of groundwater discharging into the rivers (Peterson et al., 2010). In addition, geochemical tracers have been proven effective in determining spatial variability of groundwater discharge in various water bodies. For example, a study along the Delaware River and estuary shows a spike in radon activity or submarine groundwater discharge where known aquifers outcrop (Schwartz, 2001).

Piezometers and water monitoring stations help constrain flow rates by providing direct measurements of hydraulic head differences (e.g. Osgood, 2000; Wilson, 2015). Such studies provide highly dependable information at specific point locations, though heterogeneity in marsh systems makes up-scaling and extrapolation challenging. Using multiple well nests located along transects throughout two marshes, Wilson et al. (2015) determined that flow direction of groundwater is a control on ecological zonation within the marsh. In general, this and other studies (e.g. Moffett et al., 2012) show that

ecohydrological zones form where the groundwater hydrology of a specific area creates an environment that is ideal for the growth of a specific marsh species. Areas within the high marsh, where there is a mixture of saline and freshwater, will be conducive to marsh plants that can survive large variations in salinity, while areas in the mid-marsh where salts concentrate favor plants that are adapted to hypersaline environments. Such studies demonstrate that direct observations of flow phenomena are necessary to provide modeling constraints and to guide interpretations of spatially and temporally variable pore water characteristics within the marsh system.

The addition of geophysical imaging techniques (Electrical Resistivity Tomography (ERT)) can potentially provide spatially continuous information on variability in pore water salinity as a result of ocean water mixing with marsh platform groundwater and fresh water from upland sources. In addition, complex pore water flow pathways resulting from geological controls may be imaged, thus informing the spatial extent to which results from other approaches (e.g. piezometers) may be extrapolated. Repeated electrical resistivity measurements at a fixed location can provide insight into a variety of time transient groundwater processes. Tidally induced groundwater flow has been imaged in a variety of settings including beachfaces (Swarzenski et al., 2006; Swarzenski and Izbivki, 2009), and salt marshes (Carter et al., 2008; Carter, 2014). In addition to tidally induced groundwater flow imaged utilizing electrical resistivity, seasonal (monthly) variability in the subterranean mixing zone was identified in North Inlet, SC (Carter et al., 2008).

Electrical resistivity surveys have evolved from traditional vertical borehole soundings to horizontal techniques that allow for two-dimensional, and even three-

dimensional, subsurface analysis (Colella et al., 2004). ERT measures the ability of a subsurface material to pass an electrical current by recording the resistivity value in Ω-m. The subsurface material and pore water are the dominant controls on resistivity values. A lower resistivity value will be recorded from a substrate with a high percentage of clay, while bedrock will have a very high resistivity value. The saturation of the sediment will also control the resistivity values of the subsurface. If the sediment is fully saturated there will be lower resistivity values compared to unsaturated sediment, which will have a very high resistivity value. The chemical makeup of the pore water determines the resistivity of the measured medium. Saline waters will have a lower resistivity value compared to fresh water (Figure 2).

ERT can be used to visually assess the changes and composition in pore water fluids, making it an ideal technique to examine coastal groundwater interaction and dynamics (Dimova et al., 2012). In coastal areas, where hydraulic head in the surficial aquifer may be reversed during the daily rise and fall of the tide, the interface between intrusion from ocean water and pore water moves laterally and vertically within the aquifer throughout the tidal cycle. Since the aquifer matrix sediments remain consistent in terms of geologic composition over such short time scales, observed changes in subsurface electrical resistivity are a result of changes in pore water composition.

A combination of Wenner and Dipole-Dipole arrays was chosen for this study because they provide the highest resolution and are most sensitive to horizontal layers (Griffiths and Barker, 1993). The Wenner array focuses electrical sensitivity in a vertical gradient, facilitating detection of horizontally layered structures (Loke, 2000). The opposite is true for the Dipole-Dipole array that has an electrical potential contour pattern

geometrically favorable for detecting vertical structures (Loke, 2000). The combination of Wenner and Dipole-Dipole arrays provide the highest spatial resolution and the best opportunity to detect small-scale changes in tidal variability of the tidal creek zone.

For electrical resistivity surveys in general, the electric current (*I*) is transmitted into the ground via a pair of current injection electrodes, and the potential drop (change in voltage, ΔV) is measured between other pairs of electrodes. Increasing separation between electrode pairs results in the increasing depth measurement of the change in voltage, ΔV. Coastal Carolina University's AGI Supersting R8 multichannel resistivity meter and accompanying 56-electrode array were used to perform the ERT measurements. The apparent resistivity, ρ_a (Ω-m) from a homogenous subsurface is calculated by solving Ohm's Law using these equations (1 and 2):

$$\rho_a = K \frac{\Delta V}{I} \qquad (1)$$

where

$$K = \frac{1}{2\pi}\left[\frac{1}{\left(\frac{1}{r_1}-\frac{1}{r_2}\right)-\left(\frac{1}{r_3}-\frac{1}{r_4}\right)}\right] \qquad (2)$$

The geometric factor, K, is dependent upon electrode spacing (r_n), and r_1, r_2, r_3, and r_4 are the distances between the two current electrodes and the two potential electrodes. For a known current (*I*) and a measured voltage drop (ΔV), apparent resistivity can be determined for known survey geometries.

While there is a substantial number of studies (e.g. Bollinger and Moore, 1993; Moore, 1999; Osgood, 2000; Moore et al., 2002; Taniguchi, 2002; Wilson and Gardner, 2006; Carter et al., 2008; Peterson et al., 2010; Henderson et al., 2010; Carter, 2014; Wilson, 2015) that examine marsh platform hydrology through a variety of methods,

there is a lack in information on the hyporheic zone within tidal creeks in coastal salt marsh environments. The hyporheic zone can be defined theoretically by the saturated pore water beneath the channel and into the banks that is influenced by advection of channel water (Figure 3) (White, 1993). The definition of the hyporheic zone seems simple, but characterizing and sampling this zone is challenging in a tidal setting. With potentially large areas of influence in well-developed salt marshes with extensive creek networks, tidal creek hyporheic exchange is an underexplored process.

Biogeochemical and physical characteristics of the hyporheic zone in freshwater river systems have been much more thoroughly explored than in salt marshes. Studies by Wondzell and Swanson, 1996a; Wondzell and Swanson 1996b; Battin 1999; Battin 2000; Haggerty et al. 2002; Anderson et al. 2005; Gooseff et al. 2006; Boulton et al. 2010; Gooseff, 2010; Krause et al. 2011 address the complex interaction of the subsurface aquifer and channel waters in non-tidal settings. Recent studies have applied electrical resistivity tomography to image the hyporheic zone in a cross-sectional view by injecting a saline tracer into freshwater settings (Ward et al., 2010; Ward et al., 2012; Ward et al., 2014). The use of ERT as a technique for hyporheic zone analysis provides spatial and temporal assessment of solute transport, while identifying mobile and immobile areas of hyporheic zone flow (Ward et al., 2010). This study has laid a foundation for understanding hyporheic exchange processes and for attempting to quantify the extent and exchange dynamics of the hyporheic zone.

Ward et al. (2012) build upon this foundation to further characterize the hyporheic zone in a mountain stream. The authors were able to successfully image a saline tracer with ERT at different flows within a mountain stream. In unconstrained flat sections of

the stream, the tracer appears quickly in hyporheic pathways and persists for days following first arrival within the sediment (Ward et al., 2012). Further work concluded that stream channel discharge is a primary control on hyporheic transport (Ward et al., 2014). They also noted that different geological units impact rates and variability of hyporheic flow paths (Ward et al., 2014). These studies have been able to continually reproduce temporal and spatial images of the hyporheic zone during multiple stream flows and seasons and have begun to characterize how the hyporheic zone functions and behaves in a mountain stream setting.

The work that Ward et al. (2012, 2014) completed in a freshwater setting provides a basis for studying the hyporheic zone in a complex salt marsh environment using ERT. The mixing of fresher and more saline waters, and tidally driven flow conditions are ideal circumstances for the application of ERT to image hyporheic transport as surface water pumps in and out of shallow sediments surrounding the creek channels. At present, the extent of hyporheic transport is unknown in salt marsh tidal creek environments except for a study by Acworth and Dasey (2003) who concluded that there is infiltration of seawater into the bottom and banks of the creek channel and extensive mixing of groundwater and channel water within the near creek sediment.

Successful imaging of the hyporheic zone throughout a tidal cycle provides a basis for developing the maximum and minimum extent of the hyporheic zone interface in the shallow subsurface. This study uses ERT to observe and examine hyporheic flow over semidiurnal, fortnightly, and seasonal time scales in a typical salt marsh tidal creek located landward of an undeveloped barrier island in northeastern South Carolina (Figure 4). Discrete pore water samples were collected in conjunction with resistivity

experiments in an attempt to develop an empirical relationship between electrical resistivity measured in the field and actual pore fluid salinity for shallow marsh sediments. Vibracores and auger samples were collected and logged to determine the geological characteristics of the marsh creek setting. The processed resistivity data reveals a low resistivity anomaly in the sediments surrounding the creek channel that is defined as the hyporheic zone. Given the works done by Ward et al. 2010, 2012, and 2014 in a freshwater setting with a saline tracer, the hyporheic zone boundary was expected to be captured using electrical resistivity tomography in a tidal creek setting.

Study Site

The Anne Tilghman Boyce Coastal Reserve, Waties Island, South Carolina, is an undeveloped barrier island (Figure 4). The island is located on the northeastern coast of South Carolina, bounded by Little River Inlet to the north and Hog Inlet to the south. The island is roughly 0.5 km wide and 4.0 km long with an extensive back barrier marsh and tidal creek system. There is a semidiurnal mesotidal regime with a maximum range of 2.6 m. Separating the mainland and the island is an ocean-dominated lagoonal marsh comprised of Eden Saltworks Creek and Dunn Sound Creek that are fed and drained by the two inlets. In the back barrier setting of the southern spit of Waties Island are two distinct wooded barrier island remnants known as hammocks. These hammocks contain tall pine trees, surrounded by salt marsh on all sides, and are likely remnants of a relict beach dune system. The unnamed hammock nearest the marsh creek system examined in this study is 0.10 km wide by 0.25 km and is located at 33° 50'43" N and 78° 35'49" W (Figure 4).

The tidal creek examined in this study connects directly into Hog Inlet ~120 m downstream of the study site (Figure 4). The surrounding creek sediments are generally characterized by fine to silty sands. The marsh platform closest to the sand dunes toward the ocean contains generally muddier sediment and is lower in elevation than the hammock/upland side marsh platform (Figure 5). The site selected for the ERT time series is near a bend in the creek channel that contains a cut bank side with surficial sediments comprised of sandy mud and oyster shells, opposite a point bar side made of fine sand. The larger more extensive hammock/upland adjacent marsh platform is comprised of fine sand with some silty muddy areas (Figure 6). On both banks of the

creek there are fine sand levees, likely from over wash processes during high-energy storm events.

The levees contain the tallest Spartina alterniflora vegetation nearest the creek channel, and progress to shorter Spartina 3 – 5 meters into the adjacent marsh platforms. Interspersed with Spartina alterniflora is Borrichia frutescens. This vegetation zone is affected by the sand levees and transitions away from tall Spartina to short Spartina from the creek channel to the marsh platform lower in elevation. The main vegetation located on the marsh interior is Salicornia virginica, a halophytic succulent common in southeastern marshes.

Between the marsh platform and Hog Inlet is a large sand deposit that is constantly being shaped by the tides. Ocean water is introduced into the marsh system through the creek channel that cuts through this sand body. Ocean water entering the creek channel will spill over the banks and inundate the marsh platform when the tidal height reaches above 1.5 meters above mean water level. Throughout the fortnightly oscillation there are multiple tidal cycles that do not overtop the creek banks and inundate the marsh platform allowing for a build up in salinity in the marsh platform through evapotranspiration.

2. Methods

2.1 Data Acquisition

Electrical Resistivity

During field surveys with the multichannel resistivity meter and 56-electrode array, a matrix of voltage drops can be constructed as K values are changed by a series of commands programmed into the eight-channel controller/receiver unit. The electrodes

were placed at 0.5 meter intervals in a creek channel perpendicular transect. Time-series measurements were collected during spring and neap tides from September 2015 through January 2016 (Table1). Each date corresponds with 14 to 19 individual tomograms that span the course of a tidal cycle capturing two low tides and one high tide. Data collection days were selected around the peak spring and neap tides, depending on weather. All data from each sampling date has been processed and the complete time series images can be viewed in Appendix A. A typical field day required the installation of the electrode cable and ancillary equipment during low tide, allowing access to the creek bottom when the water level was at its lowest. The rest of the equipment was placed on a table at the highest elevation on the creek bank (Figure **7**). During data collection, a matrix of voltage change measurements was completed every 35 – 45 minutes. Each 35-45 minute measurement cycle produced data that could be inverted and represented as a tomogram of the resistivity conditions beneath the creek channel-marsh platform system. Continuous logging occurred throughout complete tidal cycles from low tide to low tide, resulting in up to 19 resistivity tomograms.

Water and Sediment Samples

In order to groundtruth electrical data, we collected sediment cores, discrete water samples, and auger samples along the measured transect (Figure 8). Two permanent sampling wells were placed adjacent to the channel on the landward (north) side marsh platform (electrode 38, Figure 9) at depths of 1 m and 2 m. Water samples were collected with a peristaltic pump from the wells and the surface water in the creek channel throughout the entire tidal cycle. During each measurement, wells were purged until dry during the midpoint of each resistivity data set. The water collected after the recharge of

the well was then collected until the sample was large enough to fully submerge the YSI probe. The YSI handheld meter was borrowed from Coastal Carolina University Environmental Quality Lab (EQL), and was initially calibrated by the EQL, and then with YSI 3168 Conductivity calibrator fluid before each field date, as well as in the field if instrument drift was occurring.

Soil samples were collected with a hand auger in 0.5 meter depth increments and sealed in a watertight bag for laboratory analysis. These samples were collected down to depths of -2.75 m at 5 locations along the ERT transect (Figure 8). In an effort to gain additional geological data at a greater depth, vibracores were also collected along the transect. Vibracores were logged (Appendix B) and correlated to reveal stratigraphic layering within the near creek marsh platform (Figure 8). The stratigraphic cross section was derived from 5 vibracores in a creek perpendicular transect line adjacent to the electrical resistivity transect. The cores were used to determine the stratigraphy of the subsurface and identify laterally consistent horizontal facies changes.

2.2 Sediment Analysis

Hand auger samples were analyzed to calculate bulk density, grain size, and porosity of various sediments across the creek channel (Figure 9 and Appendix C). Laboratory analysis of the sediment samples was carried out with a Beckman Coulter LS 13 320 Laser Diffraction Particle Size Analyzer. The accompanying software was used to determine grain size, sorting, kurtosis, and skewness. Analysis of bulk density, water content, and porosity were done as follows.

The fully saturated sediment samples were weighed, dried, and reweighed to measure the amount water content as shown:

$$Water\ Content\ \% = \frac{Mass\ of\ Wet\ Sediment\ (g) - Mass\ of\ Dry\ Sediment\ (g)}{Mass\ of\ Wet\ Sediment\ (g)} \times 100$$

(3)

To calculate the bulk density of the sediment, a graduated cylinder was filled to a specific volume, while a known amount of dry sediment was placed in the cylinder. The mass of the dry sediment added to the graduated cylinder divided by the amount of water displaced yields the bulk density of the sediment sample.

$$Bulk\ Density\ (\frac{g}{ml}) = \frac{Mass\ of\ Dry\ Sediment\ added\ to\ the\ Cylinder\ (g)}{Volume\ of\ Water\ displaced\ by\ Dry\ Sediment\ (ml)} \qquad (4)$$

The density of fresh and salt water was used in the calculation to give a range of porosity. The amount of water lost in the initial drying process divided by the density of salt water or fresh water gave a range in the volume of the void space in the sediment.

$$Volume\ of\ Voids = \frac{Total\ Water\ Lost\ on\ Initial\ Drying\ Mass\ (g)}{Density\ of\ Fresh\ or\ Salt\ Water\ (\frac{g}{ml})} \qquad (5)$$

The volume of the sediment was calculated by using the mass of the dry sediment divided by the density of each sediment sample.

$$Volume\ of\ Sediment = \frac{Mass\ of\ Sediment\ Dry\ (g)}{Bulk\ Density\ (\frac{g}{ml})} \qquad (6)$$

The total volume of sediment and porosity were then calculated as follows.

$$Total\ Volume = Volume\ of\ Voids\ + Volume\ of\ Sediment \quad (7)$$

$$Porosity = \frac{Volume\ of\ Voids}{Total\ Volume} \quad (8)$$

2.3 Electrical Resistivity Processing

Assumptions made in ERT processing

AGI EarthImager 2D software was used to create inverted resistivity sections and interpret groundwater features in the context of the geological cross-section developed from cores and auger samples. Loke et al. (2003) and Loke and Lane (2004) suggest there is significant impact on resistivity results when water is overlying the resistivity cable, dampening or smoothing the resistivity values. In this study, the entire system was saturated with salt water during high tides. The assumption of adding a layer of saltwater over the terrain correction resulted in statistically unrealistic modeling results (Table 2). Tomograms with the water layer recorded high resistivity values, while resistivity of insitu sediments in a test box analysis revealed a narrow range of resistivity values (0 – 4 Ω-m). Therefore the surface water layer was excluded from the model. The model calculated highly localized features of high resistivity in order to try to resolve the very narrow range of resistivity values measured (Figure 10). Groundtruth data were collected to help produce more realistic inversions of the electrical data.

Soil sample resistivity was measured directly with a soil resistivity test box. The range of resistivities measured on discrete samples in the lab fell well within a 0 – 4 Ω-m range (Table 3). Figure 2 was created utilizing hand auger sample 1A to view the electrical resistivity over a range of pore water salinities. The sediment was flushed and dried multiple times between each test to make sure that there was no cross contamination from each sample. Hand auger sample 1A was mixed with 100ml of 0 ppt, 5ppt, 10ppt, 15ppt, 25ppt, 35ppt, and 45ppt waters. The test box was then hooked up to the resistivity equipment and the resistivities were recorded for each sample. Figure 2 shows that a 0ppt water and sediment combination has a resistivity of 109.9 Ω-m, while 5ppt water and sediment combination has a resistivity of 5.865 Ω-m. The range from 25ppt to 45ppt is between 1.371 Ω-m and 0.8176 Ω-m. For a large change in salinity of the pore water, there is in response a relatively low change in measured resistivity. Differentiating the typical changes in salt marsh salinities (25 – 45ppt) with electrical resistivity is pushing the limits of the technique due to the small change in resistivity over the values. Imaging the interface between two similar salinity bodies with electrical resistivity on a larger scale is opening up the data to processing errors in the inversion model.

Figure 11 shows the temperature effects on creek water at 32ppt, as well as temperature effects on hand auger sample 1A. From both of these graphs, the relationship between resistivity and temperature can be concluded that with increasing temperature there is a decrease in resistivity values. This effect is more pronounced with water only, with a smaller change in resistivity of pore water and sediment combination. When interpreting the data with the water layer this relationship needs to be considered.

To further test the validity of excluding the water layer, synthetic models were constructed in an effort to simulate measured resistivity data by using a priori geological knowledge. The a priori models included a mesh with resistivity values assigned from the soil test box measurements (Figure 12). The a priori model was then inverted and visually compared to field transect electrical measurements. It was determined that the most realistic model results were achieved by excluding the surface water layer in order to avoid generating spurious anomalies (Figure 10). The processing methodology of the resistivity images and interpretation from this point on make the assumption to excluded the water layer from the processing to analyze the simpler more uniform layer of mixing in the near creek sediments.

Data Inversion

The inversion output includes the measured apparent resistivity psuedosection, which is the raw stg data, and the calculated apparent resistivity psuedosection, which is the simulation of raw data that is modeled from the inverted resistivity section (Figure 13). The inverted resistivity section is the geologic cross-section view of the subsurface that can be interpreted. Once the inverted section is created and the apparent resistivity pseudo section is calculated, root mean square (RMS) and least square (L2) statistics are calculated to determine how similar the calculated apparent resistivity psuedosection is to the measured apparent resistivity psuedosection. The model will add or remove complexity to the inverted resistivity section, which will change the calculated apparent resistivity psuedosection through multiple iterations (around 5) until convergence upon acceptable statistical boundaries of RMS less than 10 and L2 less than 1.0.

Once statistical convergence is achieved, the image properties (min/max contour level, number of colors, and color pallet) are adjusted to a specific and consistent color palette for direct comparison between subsequent images. Changing the properties allows the user to highlight specific resistivity values of interest, and makes visual inspection of the data more obvious. For visual inspection, changing the color contours to 256 intervals allowed for easy identification of ambient background resistivity and hyporheic zone processes (Figure 13). Exporting the processed stg files in XYZ format allowed the data to be used for quantitative analysis.

Hyporheic Zone Analysis

In order to examine the hyporheic zone, the processed ERT data was inspected for visual evidence of pore water changes within the near channel area. The QPS Fledermaus DMagic software program was used to convert XYZ files into scalar grid files in the WGS 1984 UTM Zone 17 North coordinate system to correspond with the RTK-GPS data. Mesh parameters were selected as weighted moving average, weight diameter was set at 4, mesh cell size was 0.14 units creating 47 rows and 193 columns, and the vertical datum was selected to be unspecified meters. These parameters were selected to give the highest resolution mesh size without creating unnecessary data gaps (Figure 14). The grids were exported as ASCII output files that could be easily manipulated in ArcGIS.

ArcToolbox has a suite of data measurement tools that can quantify specific geometries of the cross-sectional view of the interpreted hyporheic zone. ArcGIS projects were created for each data set. Terrain files used in EarthImager were also brought into ArcGIS to give an accurate representation of the land surface in areas where the gridding process smeared the elevations (Figure 15).

Calculating the cross sectional area of the hyporheic zone allowed us to quantify the area of subsurface that was affected by pore water advection throughout a tidal cycle. The 10 m-wide creek channel is located between electrodes 17 and 37 (Figure 16). Defining the creek channel by electrode can differentiate what was influenced by advection from the creek channel and percolation of water through the marsh platform. This separation was necessary to create a boundary zone for the area calculation in ArcGIS. Selecting each individual ASCII file and applying the raster calculator tool within the spatial analyst toolbox prompted the raster calculator screen to create a raster

image defining the hyporheic zone area to the ambient background resistivity (0.604 Ω-m).

The output of this tool created a two-color raster image of any resistivity values less than 0.604 Ω-m (hyporheic zone) and any resistivity value greater than 0.604 Ω-m (ambient background) (Figure 16). The 0.604 Ω-m contour was selected as the outer most boundary between what visually appeared to be the ambient background resistivity and hyporheic zone water infiltrating the sediment. This boundary was a major assumption in the processing methodology. This could be an overestimate of the change in salinity boundary line thus overestimating the extent of the area of influence. Limitations in the processing methodology of electrical resistivity create a smoothing effect on the subsurface layers. The edge of the hyporheic zone was defined by the 0.604 Ω-m contour no matter what the tidal cycle stage.

Converting the newly made raster image into a polygon was accomplished by using the conversion toolbox, from raster, raster to polygon. The polygon defining the hyporheic zone was manually adjusted to exclude excessive background areas in the tomograms that fell within the 0.604 Ω-m contour, but were related to other phenomena not associated with hyporheic exchange such as percolation of water on the marsh platform. While much of the data appears to fall within this range, it is important to note the low data density limitations of the resistivity method in the deepest areas on either end of the transect. This is due to the lack a data points from the apparent resistivity psuedosection and extrapolation of the model in the creation of the inverted resistivity section (Figure 13).

Calculating the thickness and width of the hyporheic zone enabled a better understanding of how pore fluid propagates into the creek bed and surrounding marsh sediment over a tidal cycle. To better resolve the differences between horizontal and vertical changes in salinity through the sediments, changes in the thickness and width of the hyporheic zone were measured for each time step in each resistivity survey. A new polyline shapefile was created in Arc Catalog. The midpoint of the channel was defined to be at electrode 27, while the edges of the creek remained at electrode 17 and 37. Electrode 27 was selected using the snapping feature and the bottom of the hyporheic zone to create the vertical line measurement of the hyporheic zone, which is the thickness of the hyporheic zone at the midpoint of the creek channel. Selecting the midpoint of the newly created vertical thickness line and constructing a horizontal line extending to the 0.604 Ω-m contour defined the width of the hyporheic zone. This was repeated on the opposite side to complete the measurement for the width (Figure 1**7**).

3. Results

Two major controls on electrical resistivity are subsurface mineralogy and pore water composition. In order to determine the signal contribution from mineralogy, sediment cores were collected along the transect line and used to create a stratigraphic cross section. Pore water samples were collected from wells adjacent to the creek bank in order to determine any variability in salinity with depth in the sediment. These data sets provide a basis to support the assumption that spatial and temporal changes in resistivity within the sediments surrounding the creek bank are due to changes in the pore water composition in the hyporheic zone. The hyporheic zone can then be further analyzed for seasonal, fortnightly, and hourly changes observed within the data sets.

3.1 Marsh Platform Geology

Hand auger samples and vibracores were collected to groundtruth the electrical resistivity transect and to develop a detailed view of horizontal layering and varying depositional environments within the near creek marsh platform. The geology of the marsh adjacent to Waties Island is typical for the southeastern US. Similar marshes usually contain fine sand or mud deposits overtopping older sand layers from relict beach-ridges as observed in North Inlet estuary in South Carolina (Carter et al., 2008), and between Cabretta Island and Sapelo Island, Georgia (Wilson et al., 2015).

Core lengths varied from 3.23 m to 3.78 m. Detailed visual analysis of the vibracores exposed a topmost marsh layer, overlying a muddier paleomarsh layer overtopping a sandy beach system (Appendix B). The topmost layer is a 0.5 to 0.75 m thick modern marsh that contains brown to dark brown fine sand to muddy fine sand with root remnants and other organic material (Figure 18). The modern marsh layer overlies an old marsh platform that is a 0.5 m thick unit of black, silty mud containing plant remnants and oyster shells (Figure 19). The next unit is a 2.5 m thick dark grey-to-grey, fine sand unit that contains whole coquina shells and crushed shell fragments, increasing in abundance with depth (Figure 20). This unit could be part of an old beach system containing the littoral zone at the bottom of the unit, progressing to the dune system toward the top. This sequence is indicative of a littoral zone progressing to the modern marsh during falling sea level.

Grain size, porosity, water content, bulk density, and relevant grain size statistics of the hand auger samples offer more detailed characterization of sediments along the resistivity transect (Appendix C). Sediment analysis indicates that very fine-grained sand

is the most abundant, with a substantial percentage of silty, clay (Table 4). The average porosity of the sediment is between 0.44 – 0.45 which falls well within the expected bounds for unconsolidated fine sand outlined by Morris and Johnson (1967).

3.2 Marsh Creek and Pore water Salinity Variablility

Water samples collected at the midpoint of each tomogram where recorded and plotted in an attempt to differentiate the resistivity boundary movement during a fortnightly tidal cycle (Figure 21). Separating the spring and neap tides, based on tidal amplitude, was an attempt to capture the movement of this boundary past the water sampling wells. During the neap tide, it was hypothesized that the boundary would not pass through the well pore space due to the tide or surface waters never influencing the well location. In contrast, the spring tides inundate the entire marsh platform moving this boundary past the well location and into the marsh platform

3.3 ERT time series

Time series analysis of ERT data, from low tide to low tide, provides a visual method for interpreting processes that control pore water exchange during a tidal cycle. A consistent change in the resistivity signal, between tomograms, within the sediment surrounding the creek channel provides visual evidence of hyporheic exchange. Under the assumptions laid out in the methodology, the extent of the resistivity boundary of what is believed to be the hyporheic zone can be visualized in the tomogram images. The ERT data reveal a tidally variable hyporheic zone with a maximum area of 23.32 m^2 from the ArcGIS calculations (Table 5).

Examination of hyporheic zone area, thickness, and width reveal characteristics of the process of surface water infiltration into tidal marsh creek channel sediments. There is

a linear relationship between the hyporheic zone area and tidal level, with the cross sectional area ranging from 23.24 m^2 to the smallest at 0.08 m^2 (Figure 22). This suggests that hyporheic zone area develops in direct and immediate response to tidal infiltration. The difference in spring and neap tidal ranges is reflected in the variability of hyporheic zone areas. The larger range in water level during spring tide results in development of the largest and smallest hyporheic zone areas.

The midpoint thickness of the hyporheic zone ranged anywhere from 0.3 m at low tide to 2.7 m at high tide. This formed a strong linear relationship with the tidal height with a resultant R^2 value of 0.97 (Figure 23). The cross sectional width of the hyporheic zone ranged from 2.4 m at low tide to 8.1 m at high tide. The relationship between the width and area was logarithmic in nature, indicating that the change in width was largest when the tidal height was below the 1 m level, once it was above that level; the change in width was smaller than the thickness (Figure 24).

4. Discussion

4.1 Salinity of the Near Creek Marsh

In order to better understand the impact of salinity on the resistivity tomogram time series, surface and pore water samples were collected. The combination of pore water and geologic characteristics has the largest influence on an electrical resistivity signal. Since the the geology is not changing, the change from one resistivity image to the next is due to changing pore water composition.

Sampling the pore water salinity of the shallow subsurface reveals a two layer hydrogeologic system coupled for exchange with each other under certain tidal conditions (Figure 21). Evapotranspiration likely contributes substantially to the

variability, concentrating salts in the shallow marsh sediments. The lower bound of 32 ppt likely represents complete flushing of the sediments with surface water (blue dots, Figure 21). The deeper layer is less affected by the root zone or precipitation on a short time frame, and is therefore more consistent in salinity.

Throughout the fortnightly tidal cycle, the salinity drops and is clearly influenced by the infiltration of surface water into the shallow layer (yellow dots) during spring tide (Figure 25). Less complete flushing during neap tides is indicated by constant salinity throughout the tidal cycle (yellow dots) (Figure 26). Salinity values from all neap tide measurement periods show no obvious response to changing water levels throughout the tidal cycle (Figure 21). Trend lines for both shallow and deep creek bank wells show no correlation with tidal amplitude, unlike the spring tide plot where shallow well salinity consistently approaches surface water salinity at the highest tides (Figure 21 and 25). During neap tide, the water level is never high enough to overtop the creek channel banks and inundate the marsh platform. The channel water never mixes far enough into the marsh sediment to fully inundate the creek bank and flush the sediments sampled by the shallow well.

This meant that the observed change in tomogram images from one image to another is a change in the pore water composition (salinity). Figure 27 shows a cartoon figure that at T1 the boundary between two different salinity masses to be at a specific location. From T1 to T2, this boundary has changed to the left side of the block diagram. From this image the only observable differences in the two images is that the boundary has changed. There can be no assumptions made about the direction of groundwater movement or velocity of fluid moving through the subsurface. This cartoon model is

comparable to what is captured in the resistivity tomograms. From image to image this salinity boundary beneath the creek channel is changing as the tides are changing but there can be no assumptions to the velocity or direction of fluid flow.

The frequency of inundation of the salt marsh controls the flushing of the near-creek sediment, potentially creating larger nutrient flux into and out of the system. Marsh vegetation such as Spartina alterniflora is dependent upon the tidal flushing of near-creek sediments (Osgood, 2000; Gardner, 2005). This can be observed at Waties Island, where elevation of the marsh also contributes to flushing frequency. The lower elevation side (Figure 5) of the creek channel in the study area contains tall Spartina alterniflora, while the higher elevation side (Figure 6) contains the shorter variety. In some areas, zonation of marsh vegetation may be affected by the frequency and extent of the hyporheic zone expanding into the near creek sediment. The lower marsh side is inundated by the tides more often, flushing the sediment more regularly allowing for the removal and addition of oxygen and nutrients to the subsurface.

4.2 Hyporheic Zone Morphology

The range of observed variability in width of the hyporheic zone is much larger than the variability in thickness, suggesting lateral transport is the dominating process (Figure 28). The large amount of pore water – surface water exchange assumed to occur based on results in this study is consistent with the findings of Gardner (2005). He suggested that two-thirds of total seepage over a tidal cycle comes from the creek bank (width), while the other one-third comes from the channel bottom (thickness).

Figure 28 plots thickness verses width to reveal the channel and hyporheic zone morphology. From the figure, the hyporheic zone thickness-width curve reveals a

logarithmic relationship with a R^2 value of 0.73. There is a sharp increase in width then followed by a dominant increase in thickness. This indicates that the salinity boundary beneath the creek channel first increases in width then in thickness as the tide or channel water increases and decreases. These results suggest the possibility that surface water infiltrates the creek channel sediments moving the boundary more rapidly in the horizontal direction than the vertical. As the tide continues to rise, a limit is reached where the horizontal boundary direction does not increase. This is possibly due to frictional effects as suggested by Schultz and Ruppel (2002).

The channel morphology appears to follow a similar trend with a logarithmic pattern with a R^2 value of 0.95. The width of the channel increases at lower tides, followed by a transition to consistent lateral spreading while the thickness increases. The lateral spreading of the creek channel will eventually break from the banks and spill onto the marsh platform. Electrode 17 and 37 is the separation between platform and creek channel at 9.81m wide. There are similarities of the channel morphology width and thickness and the hyporheic zone width and thickness following same type of trend. This would be expected that the hyporheic zone morphology would be similar to the channel morphology. The difference between the two is that the hyporheic zone thickness at its largest is almost two times larger that the thickness of the creek channel. This similarity could be due to the smearing of the data set suggested by Loke and Lane (2004). It can be concluded that the data set is not yet refined enough to differentiate between the overtopping waters and the subsurface processes due to the similarities of the trends. Due to the slight difference, there needs to be more refinement in the processing of the

resistivity images to include the water layer to differentiate what is the surface and subsurface signal contribution to the resistivity images.

4.3 Addition of a Water Layer

There are two discrepancies in the processing of electrical resistivity images. The first scenario is using just the terrain file, which makes the assumption that the overlying water layer does not influence the subsurface resistivity processing. This simplifies the mixing boundary as seen in Figure 29 B and D. Reversing the hydraulic gradient with the rising tide with porous sediments that are laterally uniform, it is reasonable to assume that the water will saturate the formation uniformly (B and D). Gardner (2005), Wilson et al. (2006) and Wilson and Morris (2012) have modeled this reversal in flow with discharge into the creek during low tide and recharge during rising tides. This simplified mixing boundary was assumed in the processing of the tomograms.

The more complex scenario is to include the water layer that creates spurious high resistivity anomalies (Table 2), and further complicates interpretation of the subsurface interaction of surface water with subsurface waters (A and C). One explanation of the complex mixing observed by including water layer can be from temperature changes. Figure 30 shows the channel and pore water temperatures of September and January field days. In September, there is warmer channel water moving into a cooler subsurface. Understanding the relationship between temperature and resistivity (Figure 11) reveals that a warmer mass of the same composition has a lower resistivity value. This could lead to the interpretation that the changing resistivity values could be attributed to this temperature difference between the surface and subsurface masses. During the January field date, the subsurface reveals higher resistivity values indicating that the cooler

channel water is moving into the warmer subsurface causing a rise in resistivity. The complicated resistivity results with the water layer could reveal the complexity of subsurface mixing while imaging a blend of salinity and temperature changes, making interpretations of the tomograms difficult. Work is still needed to resolve the high resistivity anomalies of the tomograms including the water layer. Utilizing either method, ERT is recording a subsurface change in resistivity attributed to two different water masses mixing and interacting within the near creek subsurface.

5. Conclusion

Electrical resistivity as a viable tool to measure changes in pore water composition in a salt marsh environment needs more refinement in differentiating different saline and/or temperature boundaries. There are multiple issues that arise to successfully image a change in subsurface pore space composition beneath a tidal marsh creek channel. The major assumption to exclude a water layer from the processing simplified the interpretation and created a uniform mixing boundary in the subsurface that was easily identifiable and replicable.

While the exclusion of the water layer created statistically more accurate results (Table 2) and was more representative of the hand auger sample analysis (Table 3). There was too much of a similarity in the channel morphology and the defined hyporheic zone morphology to determine if this uniform boundary was an artifact of the overtopping water layer. The issue of including the water layer gave rise to spurious resistivity bodies that did not align with ground truthing experiments. This method gave rise to a complicated subsurface mixing interface that could be temperature and/or salinity

dependent. There needs to be further refinement of this method to address the issues of the high resistivity anomalies produced.

While electrical resistivity has been proven to be a viable technique in a identifying a salt-freshwater interface, the limitations of the instrument may have been reached when identifying pore water boundaries in the shallow subsurface of a salt marsh. The technique needs further development to accurately image a salinity and/or temperature boundary by the creation and implementing a water layer file that is within the ground truthed parameters observed. Once these developments have been implemented in the processing technique, analysis of the hyporheic zone can continue in the detailed analysis that has been described in this paper.

Understanding the limitations of electrical resistivity is needed to determine what the instrument can and cannot measure, but with further refinement, electrical resistivity could be a viable tool and technique to gather spatial and temporal analysis of the hyporheic zone and shallow subsurface salt marsh salinity/temperature boundaries. The application of the technique from a fresh water saline tracer experiment (Ward et al. 2010) at this time does not readily transfer into the coastal salt marsh tidal creek channel environment due to the complexity of marsh hydrology and the processing limitations.

6. Literature Cited

Acworth RI, Dasey GR (2003) Mapping of the hyporheic zone around a tidal creek using a combination of borehole logging, borehole electrical tomography and cross-creek electrical imaging, New South Wales, Australia. Hydrogeology Journal 11:368 – 377

Anderson JK, Wondzell SM, Gooseff MN, Haggerty R (2005) Patterns in stream longitudinal profiles and implications for hyporheic exchange flow at the H.J. Andrews Experimental Forest, Oregon, USA. Hydrol. Process. 19:2931 – 2949

Bartlett KB, Bartlett DS, Harriss RC, Sebacher DI (1987) Methane emissions along a salt marsh salinity gradient. Biogeochemistry. 4:3: 183 – 202

Battin TJ (2000) Hydrodynamics is a major determinant of streambed biofilm activity: From the sediment to the reach scale. Limnol. Oceanogr. 45:6: 1308 – 1319

Battin TJ (1999) Hydrologic flow paths control dissolved organic carbon fluxes and metabolism in an alpine stream hyporheic zone. Water Resources Research. 35:10: 3159 – 3169

Bollinger MS, Moore WS (1993) Evaluation of salt marsh hydrology using radium as a tracer. Geochimica et Cosmochimica Acta. 57:10: 2203 – 2212

Boesch DF, Turner RG (1984) Dependence of Fishery Species on Salt Marshes: The Role of Food and Refuge. Estuaries 7:4A:460 – 468

Boulton AJ, Datry T, Kasahara T, Mutz M, Stanford JA (2010) Ecology and management of the hyporheic zone: stream-groundwater interactions of the running waters and their floodplains. Journal of the North American Benthological Society 29:1:26 – 40

Burnett WC, Aggarwal PK, Aureli A, Bokuniewicz H, Cable JE, Charette MA, Kontar E, Krupa S, Kulkarni KM, Loveless A, Moore WS, Oberdorfer JA, Oliviera J, Ozyurt N, Povinec P, Privitera AMG, Rajar R, Ramessur RT, Scholten J, Stieglitz T, Taniguchi M, Turner JV (2006) Quantifying submarine groundwater discharge in the coastal zone via multiple methods. Science of the Total Environment 367:498 – 543

Cai WJ (2011) Estuarine and Coastal Ocean Carbon Paradox: CO2 Sinks or Sites of Terrestrial Carbon Incineration? Annual Review of Marine Science 3:123 – 145

Cai WJ, Wang Y (1998) The chemistry, fluxes, and sources of carbon dioxide in the estuarine waters of the Satilla and Altamaha Rivers, Georgia. Limnol. Oceanogra. 43:4:657 – 668

Capone DG, Bautista F (1985) A groundwater source of nitrate in nearshore marine sediment. Nature. 313, 214 – 216

Carter ES, White SM, Wilson AM (2008) Variation in groundwater salinity in a tidal salt marsh basin, North Inlet Estuary, South Carolina. Estuarine Coastal and Shelf Science. 76: 543 – 552

Carter ML (2014) Characterization of submarine groundwater discharge in a back barrier tidal creek. Coastal Carolina University. (Master's Theses) pp. 104

Colella A, Lapenna V, Rizzo E (2004) High-resolution imaging of the High Agri Valley Basin (Southern Italy) with electrical resistivity tomography. Tectonophysics. 386, 29 – 40

Cullinan M, LaBella N, Schott M (2004) Salt Marshes – A Valuable Ecosystem. The Traprock. 3:20 - 23

Dimova NT, Swarzenski PW, Dulaiova H, Glenn CR (2012) Utilizing multichannel electrical resistivity methods to examine the dynamics of the fresh water-seawater interface in two Hawaiian groundwater systems. Journal of Geophysical Research. 117, C02012

Gardner LR (2005) Role of geomorphic and hydraulic parameters in governing pore water seepage from salt marsh sediments, Water Resour. Res., 41, W07010, doi:10.1029/2004WR003671

Gedman KB, Silliman BR, Bertness MD (2009) Centuries of Human-Driven Change in Salt Marsh Ecosystems. Annual Review of Marine Science. 1:117 – 141

Gleeson J, Santos IR, Maher DT, Golsby-Smith L (2013) Groundwater-surface water exchange in a mangrove tidal creek: Evidence from natural geochemical tracers and implications for nutrient budgets. Marine Chemistry. 156: 27 – 37

Gooseff MN (2010) Defining Hyporheic Zones – Advancing Our Conceptual and Operational Definitions of Where Stream Water and Groundwater Meet. Geography Compass. 4:8: 945 – 955

Gooseff MN, Anderson JK, Wondzell SM, LaNier J, Haggerty R (2006) A modeling study of hyporheic exchange pattern and the sequence, size, and spacing of stream bedforms in mountain stream networks, Oregon, USA. Hydrological Processes 20:2443 – 2457

Griffiths DH, Barker RD (1993) Two-dimensional resistivity imaging and modeling in areas of complex geology. Journal of Applied Geophysics. 29, 211 – 226

Haggerty R, Wondzell SM, Jonson MA (2002) Power-law residence time distribution in the hyporheic zone of a 2nd-order mountain stream. Geophysical Research Letters. 29:13:1640

Harvey JW, Germann PF, Odum WE (1987) Geomorphological controls of subsurface hydrology in the creekbank zone of tidal marshes. Estuarine, Coastal and Shelf Science. 25. pp 677 – 691

Henderson RD, Day-Lewis FD, Abarca E, Harvey CF, Karam HN, Liu L, Lane, JW (2010) Marine electrical resistivity imaging of submarine goroundwater discharge:

sensitivity analaysis and application in Waquoit Bay, Massachusetts, USA. Hydrogeology Journal. 18: 173 – 185

King GM, Klug MJ, Wiegert RG, Chalmers AG (1982) Relation of soil water movement and sulfide concentration to Spartina alterniflora production in a Georgia salt marsh. Science. 218:4567: 61 – 63

Krause S, Hannah DM, Fleckenstein JH, Heppell CM, Kaeser D, Pickup R, Pinay G, Robertson AL, Wood PJ (2011) Inter-disciplinary perspectives on processes in the hyporheic zone. Ecohydrology. 4:481-499

Loke MH, and Lane JW (2004) Inversion of data from electrical resistivity imaging surveys in water-covered areas. Exploration Geophysics. 35, 266 – 271

Loke MH (2000) Electrical imaging surveys for environmental and engineering studies. Web access. http://www.geo.mtu.edu/~ctyoung/LOKENOTE.PDF

Loke MH, Acworth I, Dahlin T (2003) A comparison of smooth and blocky inversion methods in 2D electrical imaging surveys. Exploration Geophysics. 34, 182 – 187

Moffett KB, Gorelick SM, McLaren RG, Sudicky EA (2012), Salt marsh ecohydrological zonation due to heterogeneous vegetation–groundwater–surface water interactions, Water Resour. Res., 48, W02516, doi:10.1029/2011WR010874.

Moore WS (1999) The subterranean estuary: A reaction zone of ground water and sea water, Mar. Chem. 65, 111-125

Moore WS (1996) Large groundwater inputs to coastal waters revealed by 226 RA enrichments, Nature. 380, 612 – 614

Moore WS, Krest J, Taylor G, Roggenstein E, Joye S, and Lee R (2002) Thermal evidence of water exchange through a coastal aquifer: Implications for nutrient fluxes, Geophys. Res. Lett., 29(14), 1704

Morris D. and Johnson AI (1967) Summary of hydrologic and physical properties of rock and soil materials as analyzed by the Hydrologic Laboratory of the U.S. Geological Survey, U.S. Geological Survey Water-Supply Paper 1839-D, 42p.

Osgood D T (2000) Subsurface hydrology and nutrient export from barrier island marshes at different tidal ranges. Wetlands Ecology and Management 8:133 – 146

Peterson RN, Santos, IR, Burnett WC (2010) Evaluating groundwater discharge to tidal rivers based on a Rn-222 time series approach. Estuarine, Coastal and Shelf Science 86(2): 165 – 178

Santos IR, Dimova N, Peterson RN, Mwashote B, Chanton J, Burnett WC (2009) Extended time series measurments of submarine groundwater discharge tracers (222Rn and CH4) at a coastal site in Florida. Marine Chemistry. 113:137-147

Schultz G, Ruppel C (2002) Constraints on hydraulic parameters and implications for groundwater flux across the upland – estuary interface. Journal of Hydrology 260:255 – 269

Schwartz MC (2001) Significant groundwater input to a coastal plain estuary: assessment from excess radon. Estuarine Coastal and Shelf Science. 56:31-42

Shaw TJ, Moore WS, Kloepfer J, Sochaski MA (1998) The flux of barium to the coastal waters of the southeastern USA: The importance of submarine groundwater discharge. Geochem. Cosmochim. Actua. 62, 3047 – 3054

Simmons GM (1992) Importance of submarine groundwater discharge (SMGD) and seawater cycling to material flux across sediment/water interfaces in marine environments. Mar. Ecol. Prog. Ser. 84, 173 – 184

Swarzenski PW, Izbicki JA (2009) Coastal groundwater dynamics off Santa Barbara, California: Combining geochemical tracers, electromagnetic seepmeters, and electrical resistivity. Estuarine, Coastal and Shelf Science 83:77 – 89

Swarzenski PW, Burnett WC, Greenwood WJ, Herut B, Peterson R, Dimova N, Shalem Y, Yechieli Y, Weinstein Y (2006) Combined time-series resistivity and geochemical tracer techniques to examine submarine groundwater discharge at Dor Beach, Israel. Geophysical Research Letters, 33: L24405

Taniguchi M (2002) Tidal effects on submarine groundwater discharge into the ocean. Geophysics Res. Lett. 29(12), 1561

Wang ZA, Cai WJ (2004) Carbon dioxide degassing and inorganic carbon export from a marsh-dominated estuary (the Duplin River): A marsh CO2 pump. Limonl. Oceanogr. 49:4:341 – 354

Ward AS, Fitzgerald M, Gooseff MN, Voltz TJ, Binley AM, Singha K (2012) Hydrologic and geomorphic controls on hyporheic exchange during base flow recession in a headwater mountain stream. Water Resources Research. 48:W04513

Ward AS, Gooseff MN, Singha K (2010) Imaging hyporheic zone solute transport using electrical resistivity. Hydrological Processes. 24:948 – 953

Ward AS, Gooseff MN, Fitzgerald M, Voltz TJ, Singha K (2014) Spatially distributed characterization of hyporheic solute transport during baseflow recession in a headwater

mountain stream using electrical geophysical imaging. Journal of Hydrology. 517: 362 – 377

White DS (1993) Perspectives and defining and delineating hyporheic zones. J.N. Am. Benthol. Soc. 12:1: 61 – 69

Whiting GJ, Childers DL (1989) Subtidal advective water flux as a potentially important nutrient input to southeastern U.S.A. saltmarsh estuaries. Estuary Coastal Shelf Science 80(l): 193-199

Wilson, AM (2005) Fresh and saline groundwater discharge to the ocean: A regional perspective, Water Resour. Res., 41, W02016, doi:10.1029/2014WR003399

Wilson AM, Evans T, Moore W, Schutte CA, Joye SB, Hughes AH, Anderson JL (2015) Groundwater controls ecological zonation of salt marsh macrophytes. Ecology. 96:840 – 849

Wilson AM, Gardner LR (2006) Tidally driven groundwater flow and solute exchange in a marsh: Numerical simulations. Water Resource Res 42:W01405.

Wilson AM, Morris JT (2012) The influence of tidal forcing on groundwater flow and nutrient exchange in a salt marsh-dominated estuary. Biogeochemistry. 108:27-38

Wondzell SM, Swanson FJ (1996)a Seasonal and Storm dynamics of the hyporheic zone of a 4th-order mountain stream. I: Hydrologic processes. The North American Benthological Society. 15:3-19

Wondzell SM, Swanson FJ (1996)b Seasonal and Storm dynamics of the hyporheic zone of a 4th-order mountain stream. II: Nitrogen cycling. The North American Benthological Society. 15:20-34

Xin P, Li L, Barry DA (2013) Tidal influence on soil conditions in an intertidal creek-marsh system, Water Resour. Res., 49, doi:10.1029/2012WR012290.

7. Tables

Table 1: Specific dates when ERT surveys were conducted for the spring and neap tides from September 2015 – January 2016.

Spring Tides	Neap Tides
September 29, 2015	September 18, 2015
October 30, 3015	October 20, 2015
December 12, 2015	December 4, 2015
January 25, 2016	January 31, 2016

Table 2: Results from field dates suggest that the most statistically accurate and realistic resistivity measurements come from the terrain file (.trn) while there is significant issues that occur when using the water layer file (.uwt). This is the basis for the assumption to use the terrain file only during the processing and interpretation of data revealing a simplified mixing boundary in the subsurface.

	. trn file			**. uwt file**		
Data File	**Largest Ω-m**	**RMS**	**L2**	**Largest Ω-m**	**RMS**	**L2**
150918D_neap	2.20	6.46	0.79	211.00	9.85	0.85
150918J_neap	2.10	6.49	0.69	47.20	9.66	0.81
150929E_spring	3.00	7.07	0.85	83.00	13.47	0.97
151020H_neap	4.50	9.11	0.94	241.00	8.89	0.97
151020I_neap	4.70	9.20	0.69	227.00	8.22	0.85
151020J_neap	4.00	9.30	0.88	184.00	8.91	0.94
151030E_spring	3.60	8.43	0.68	96.00	11.23	0.81
151030F_spring	2.90	8.31	0.73	62.00	8.75	0.75
151030G_spring	4.20	8.31	0.76	56.30	8.65	0.72
151030H_spring	4.30	8.44	0.74	44.30	8.86	0.85
151030I_spring	4.80	8.73	0.63	1208.00	12.20	0.97
151030J_spring	4.90	8.74	0.97	2849.00	15.13	1.05
151204H_neap	3.70	12.88	0.82	28.70	13.56	0.83
151204K_neap	3.60	25.27	0.74	510.00	27.60	0.82
151215F_spring	3.70	5.66	0.66	22.90	10.94	0.79
151215J_spring	4.20	6.65	0.75	17.10	8.98	0.69
160125F_spring	3.00	5.52	0.71	17.80	6.10	0.74
160125H_spring	3.50	5.80	0.67	41.40	10.08	0.96
160125I_spring	3.00	5.73	0.61	25.40	6.84	0.96
160125J_spring	3.50	5.66	0.62	76.00	6.76	0.92
160125L_spring	2.80	5.66	0.67	49.80	11.08	1.02
160131C_neap	2.60	4.69	0.75	3290.00	22.17	2.65
160131D_neap	1.70	6.88	0.97	2968.00	20.82	3.20
160131E_neap	1.90	5.21	0.55	385.00	16.44	1.64
160131F_neap	2.10	5.36	0.55	2232.00	16.88	2.22
160131G_neap	2.40	6.14	0.76	587.00	14.52	1.56
160131H_neap	2.70	5.77	0.78	39.40	13.08	0.92
160131I_neap	3.10	6.29	0.99	200.00	11.37	0.88
Averages	3.31	7.78	0.75	564.26	12.18	1.12

Table 3: Average resistivity values of all hand auger samples collected.

Sample	Average Resistivity (Ω-m)	Standard Deviation (Ω-m)	Applied Current (mA)
1A	3.843	0.022	+5.744
1B	1.048	0.001	+22.03
1C	0.875	0.003	+26.88
1D	1.209	0.002	+18.20
1E	0.463	0.001	+44.09
1F	0.504	0.001	+40.58
1G	0.561	0.000	+35.70
1H	0.598	0.005	+39.15
1I	0.538	0.002	+37.93
1J	0.463	0.003	+45.31
1K	0.550	0.001	+42.60
1L	0.584	0.001	+41.01
1M	0.638	0.001	+38.98
2A	0.601	0.002	+38.68
2B	0.529	0.000	+42.62
2C	0.488	0.001	+43.01
2D	0.483	0.009	+44.83
2E	0.566	0.002	+40.30
2F	0.601	0.001	+39.53
3A	0.774	0.003	+33.37
3B	0.661	0.008	+36.75
3C	0.659	0.003	+37.81
3D	0.688	0.003	+37.78
3E	0.960	0.013	+27.59
3F	0.696	0.002	+37.48
4A	0.557	0.001	+39.09
4B	0.582	0.001	+38.52
4C	0.650	0.001	+36.31
4D	0.670	0.000	+34.42
4E	0.611	0.001	+38.43
5A	0.544	0.001	+38.87
5B	0.555	0.000	+39.33
5C	0.584	0.000	+37.51
5D	0.570	0.002	+40.27
5E	0.628	0.001	+37.26
5F	0.542	0.001	+41.92
5G	0.553	0.001	+42.11

5H	0.525	0.001	+43.24

Table 4: Results of the hand auger sediment analysis averages for the five wells, and the total average of all sediment samples.

Sediment Analysis	HA Well 1	HA Well 2	HA Well 3	HA Well 4	HA Well 5	Total Averages
Porosity	0.44 – 0.45	0.44 – 0.45	0.41 – 0.42	0.45 – 0.46	0.46 – 0.47	0.44 – 0.45
Bulk Density (g/ml)	2.56	2.02	2.53	3.14	2.28	2.49
Water Content (%)	24.52	29.19	22.43	23.77	28.18	25.60
Grain Size (φ)	3.12	3.45	2.79	2.69	2.99	3.03
Sorting	1.99	1.85	1.13	1.00	1.46	1.59
Skewness	0.48	0.55	0.47	0.44	0.49	0.49
Kurtosis	1.69	1.28	2.29	2.42	2.04	1.89

Table 5: The largest hyporheic zone area, with the corresponding highest tide, reveals that the largest tides and areas occurred during the late summer and fell gradually through the fall and winter months.

Dates	High Tide (m)	Hyporheic Zone Area (m^2)
150918_neap	1.59	13.87
150929_spring	2.04	23.24
151020_neap	1.68	14.53
152030_spring	2.01	23.19
151204_neap	1.39	12.83
151215_spring	1.63	16.29
160125_spring	1.67	15.11
160131_neap	1.19	8.24

8. Figures

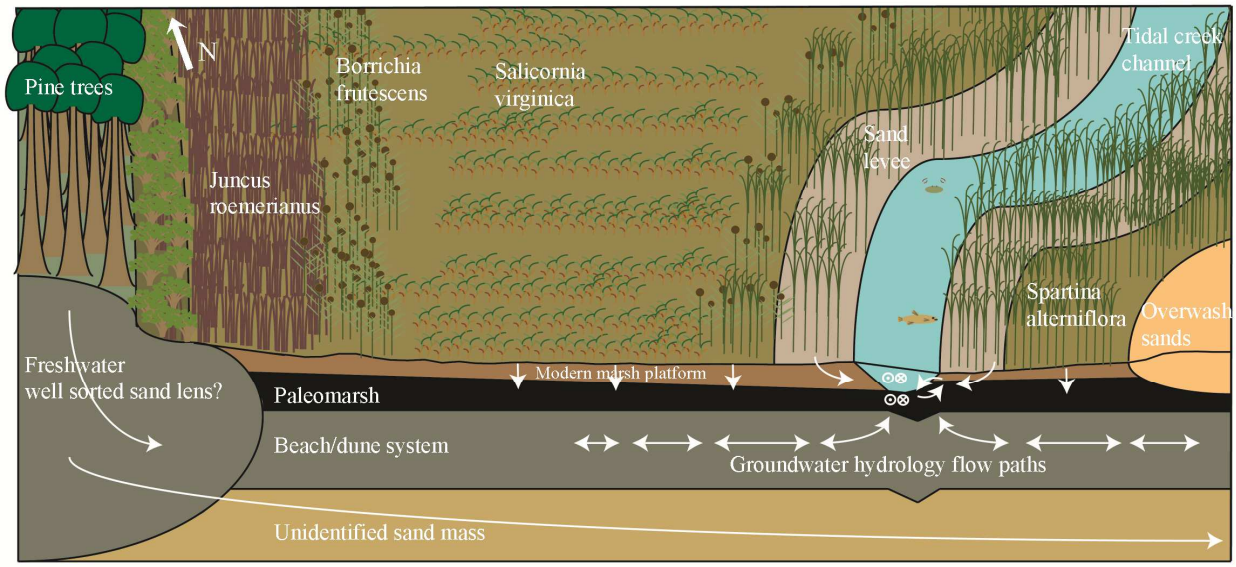

Figure 1: Cartoon illustration of the complex saltmarsh groundwater hydrology processes. There is large-scale movement of fresh groundwater flowing from the uplands through the marsh platform and/or deeper under the coastal system discharging into the open ocean. Small local processes such as the hyporheic zone that function within 2 meters of the creek bank recirculating localized channel and groundwater. There is also overtopping, infiltration of the marsh platform and percolation of water through the marsh platform.

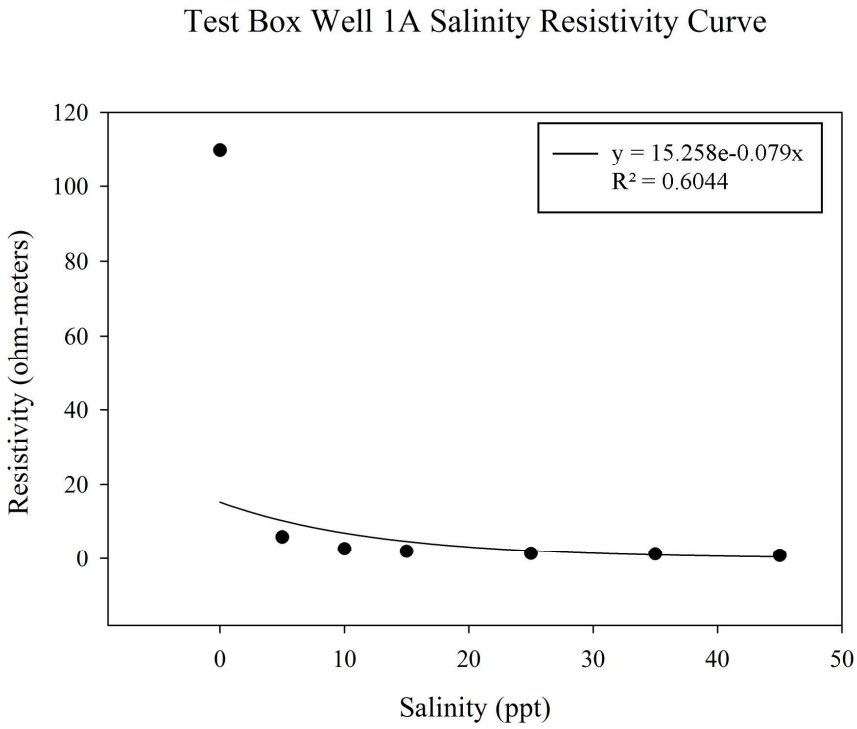

Figure 2: Resistivity test box experiment to show the effect of pore water salinity on resistivity. The sediment sample was flushed and filled with 100 ml of 0ppt, 5ppt, 10ppt, 15ppt, 25ppt, 35ppt, and 45ppt waters.

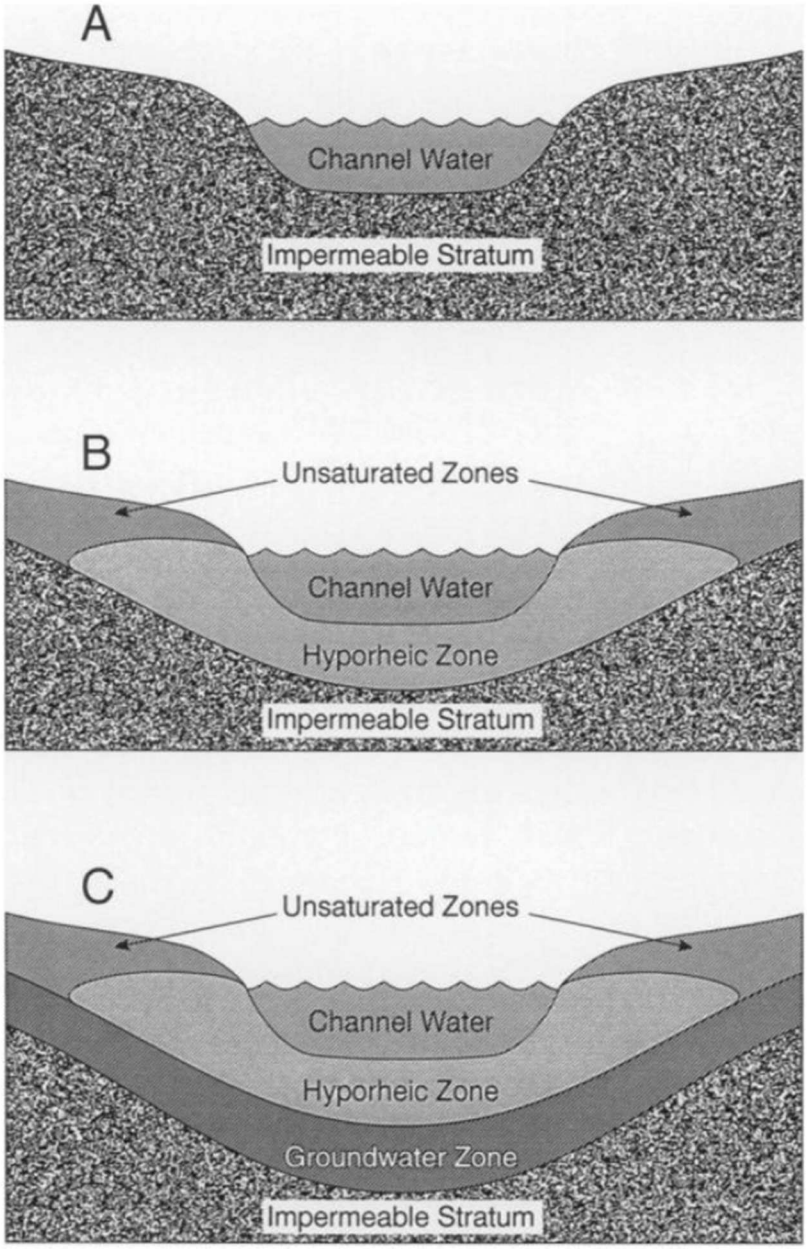

Figure 3: Cross-sectional images of channel relationship between channel, hyporheic zone, and groundwater as characterized by White, 1993

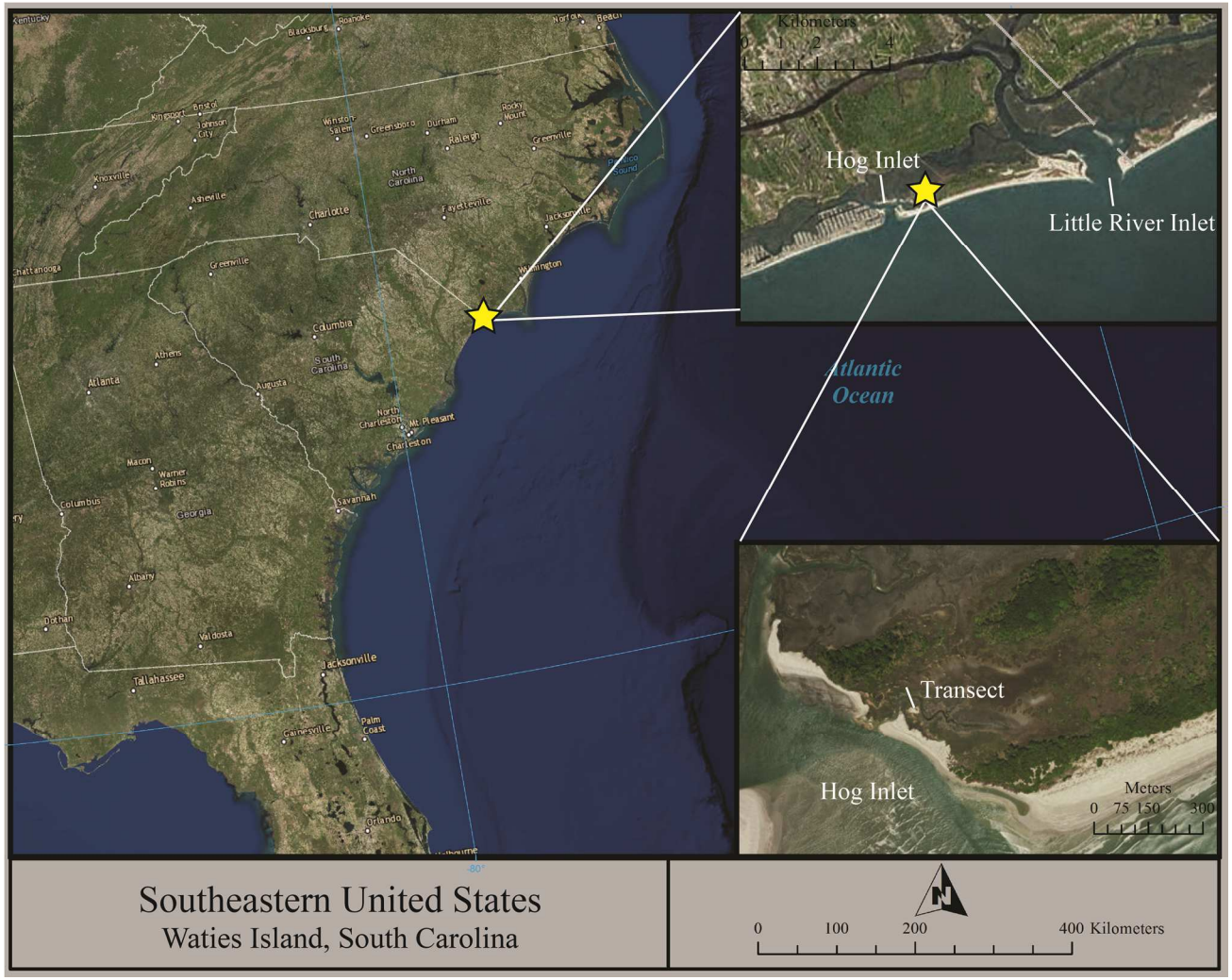

Figure 4: Regional study site overview of Waties Island, South Carolina, location of the tidal creek channel of interest with the highlighted resistivity transect.

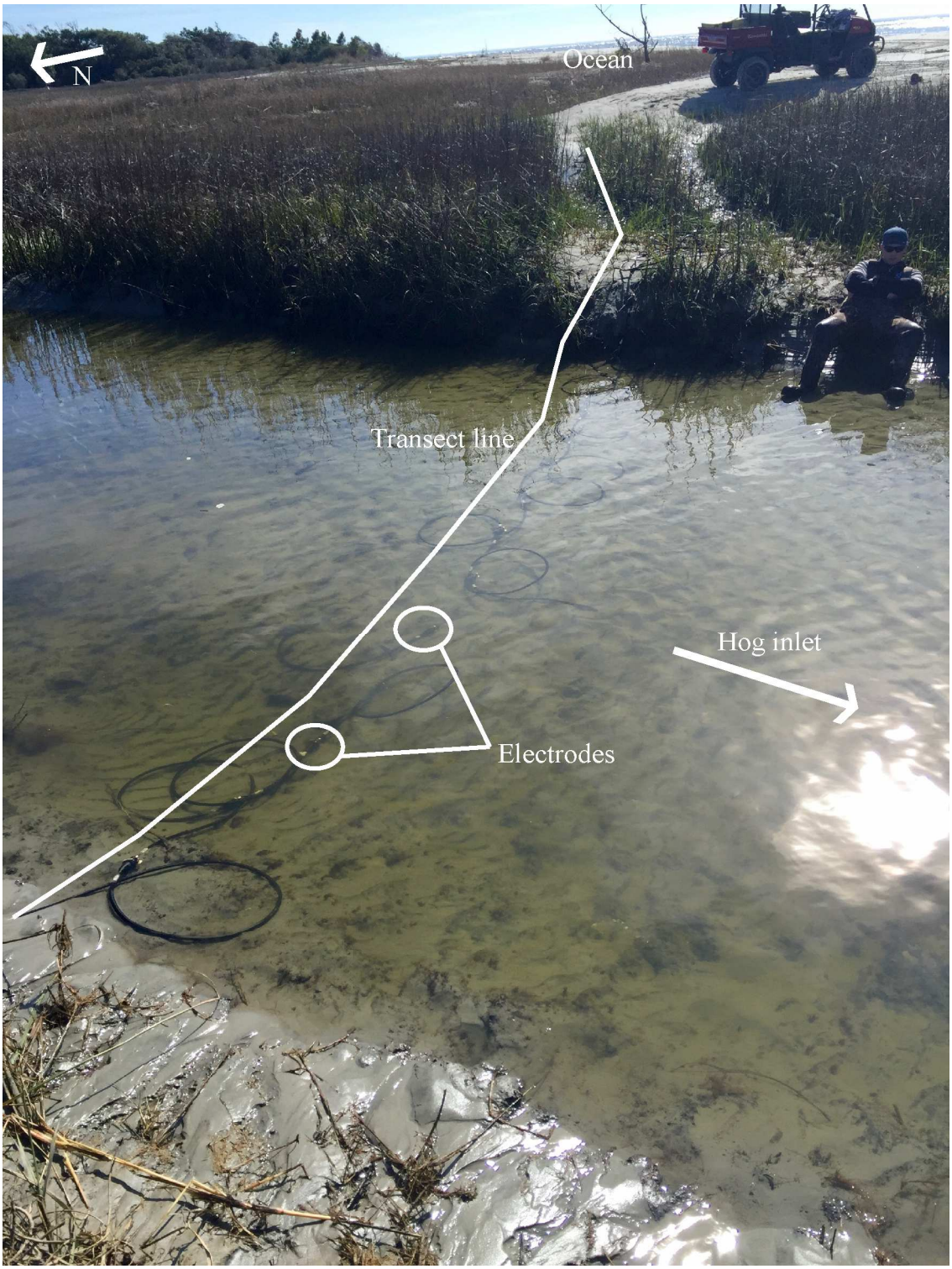

Figure 5: Image of the study site looking toward the ocean and Hog Inlet. Note the tall Spartina alterniflora, muddy sediment, sand levee next to the creek channel, and the sand lens that is the natural break between Hog Inlet and the marsh. The 56 electrode cable is also visible in 0.5 m increments.

Figure 6: Image of the study site looking landward, with the Hammock in the background. Note that this is the cut bank side of the channel, with a large sand levee, and shorter Spartina plants, the lack of vegetation is due to the continual setup of equipment on the same area. Also note the two white pipes, these are the deep and shallow wells that are located at electrode 38 in all of the resistivity surveys. Vibracore 3 is being extracted from the center of the creek channel. The small point bar is clearly visible, with the deepest part of the channel only containing water.

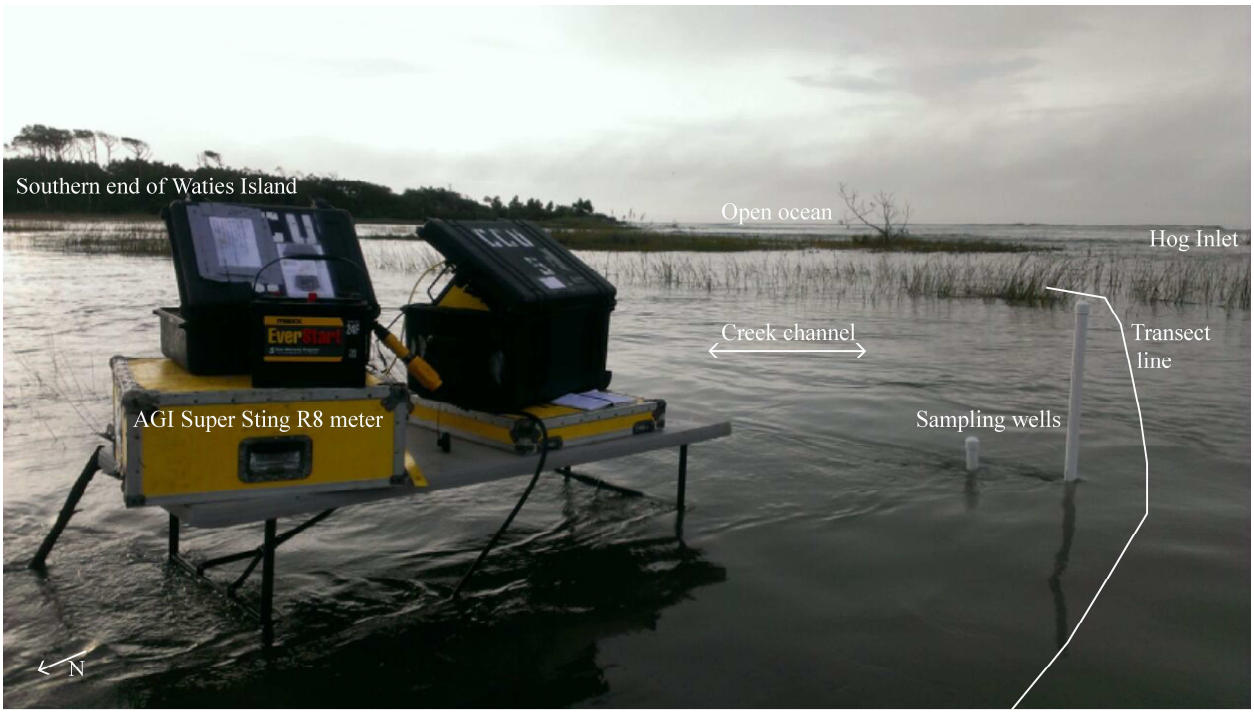

Figure 7: Image of the AGI SuperSting and operating equipment set up on the table, at the highest point in the marsh. The shallow and deep wells are barely above the highest spring tide.

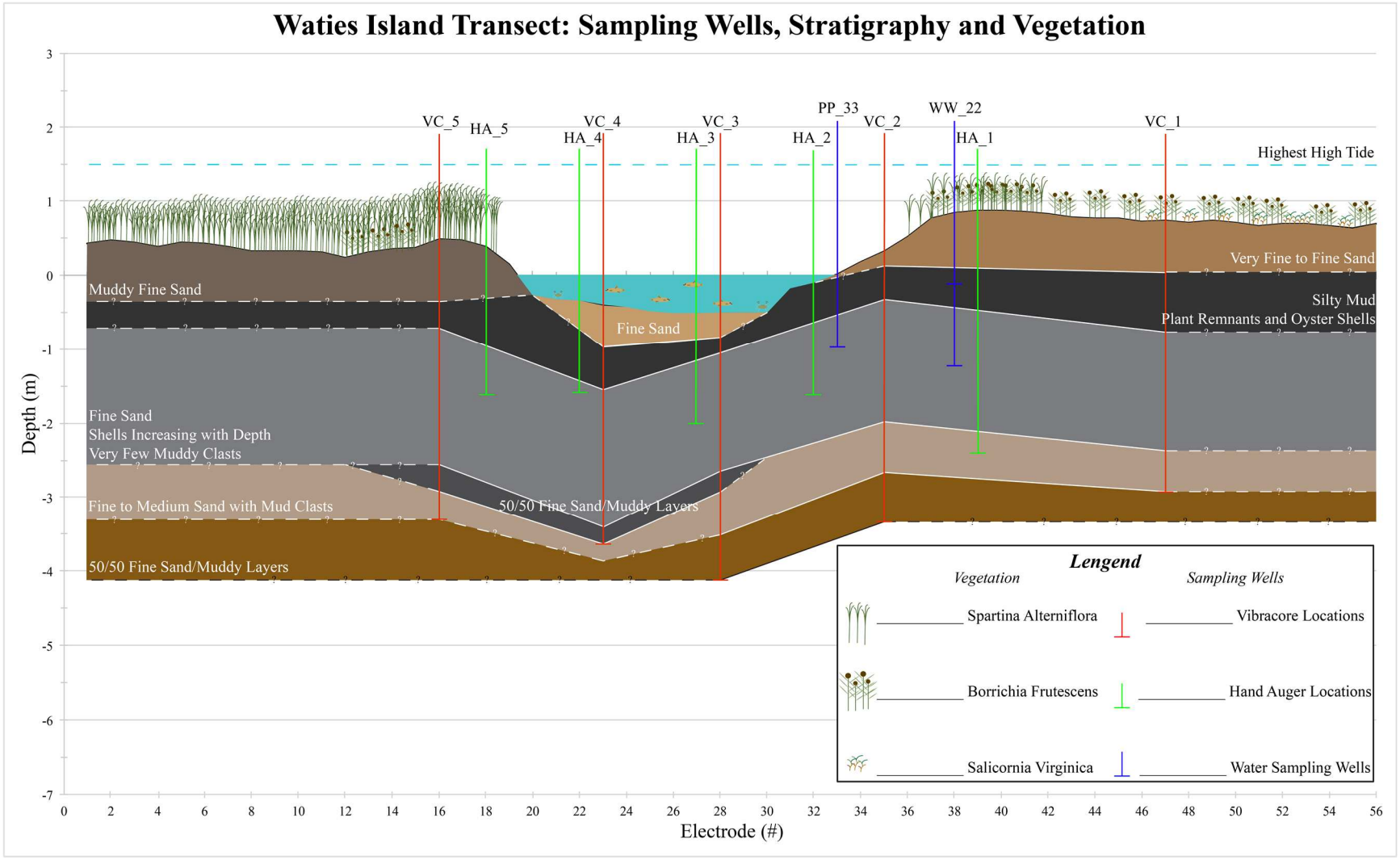

Figure 8: Stratigraphic cross section developed from the five vibracores, as well as the hand auger sampling locations and water wells.

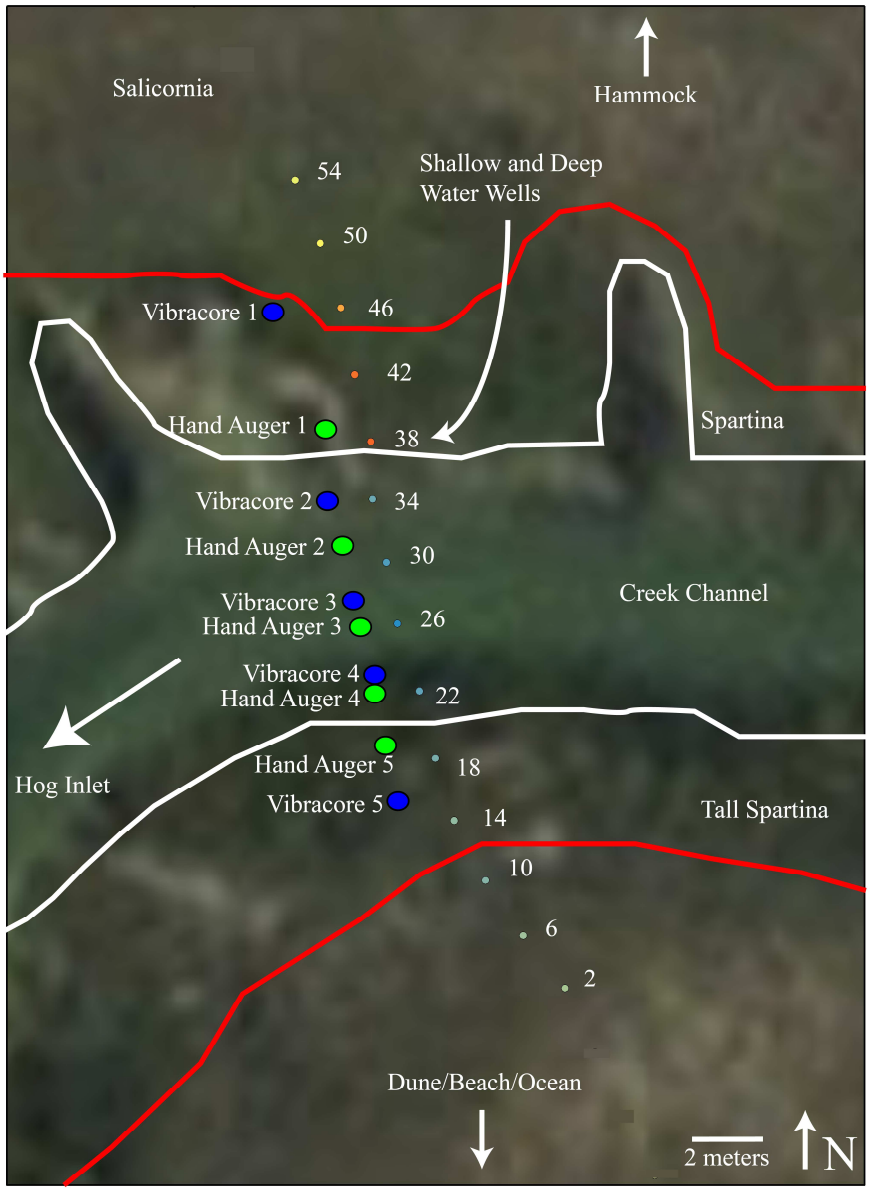

Figure 9: ArcGIS satellite view of the creek channel and marsh. The RTK GPS points are shown in 2-meter increments to show what electrode number is correspondent with that measuring point. The hand auger and vibracore locations are also located adjacent to the resistivity transect. Also note the white line indicates the channel boundaries while the red lines indicate the extent of the Spartina alterniflora vegetation.

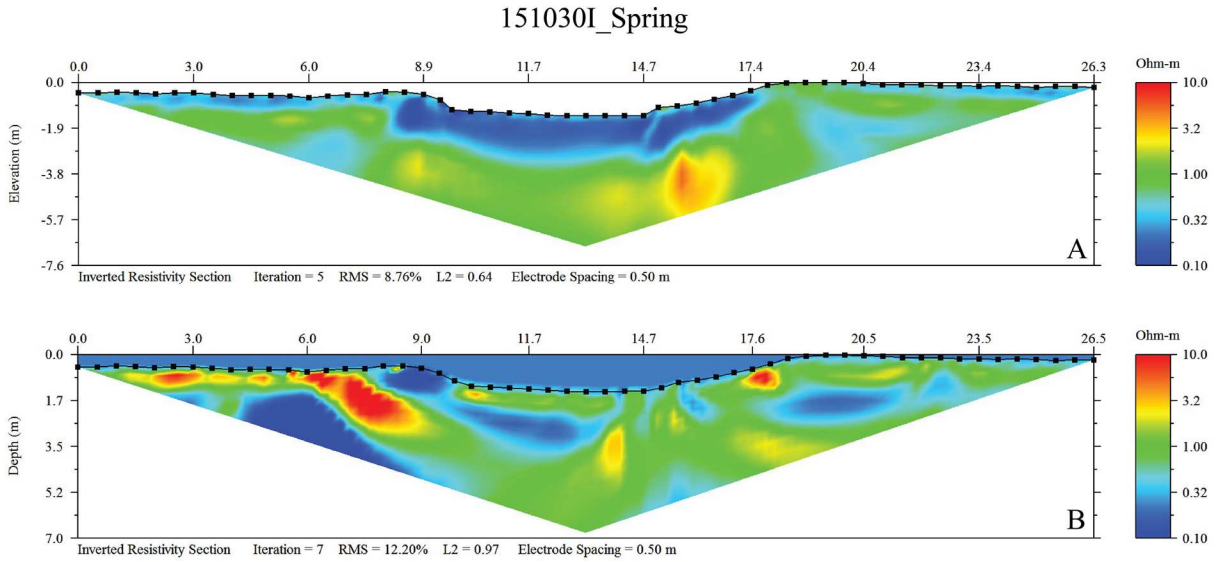

Figure 10: Image A is the processed data for 151030I_spring utilizing the .trn file. The maximum resistivity value is 4.8 Ω-m, which is well similar to the laboratory observed resistivities. Image B is the processed data for151030I_spring utilizing the .uwt file. Its maximum resistivity value is 1208.0 Ω-m, which falls well outside the range that has been physically observed in laboratory experiments. Also note the statistical difference in the processed figures, resulting in the use of only the terrain and not the water layer to give the most statistically accurate representation of field conditions.

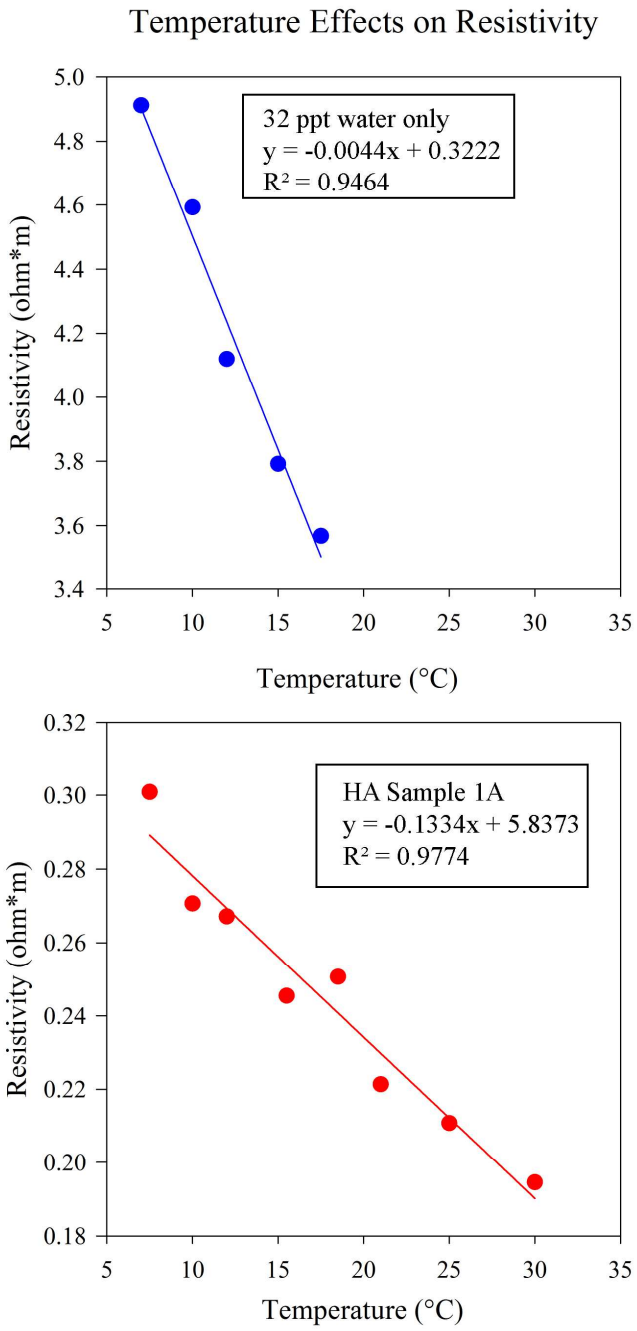

Figure 11: Temperatures inverse effect on resistivity. As temperature increases the resistivity of a material decreases.

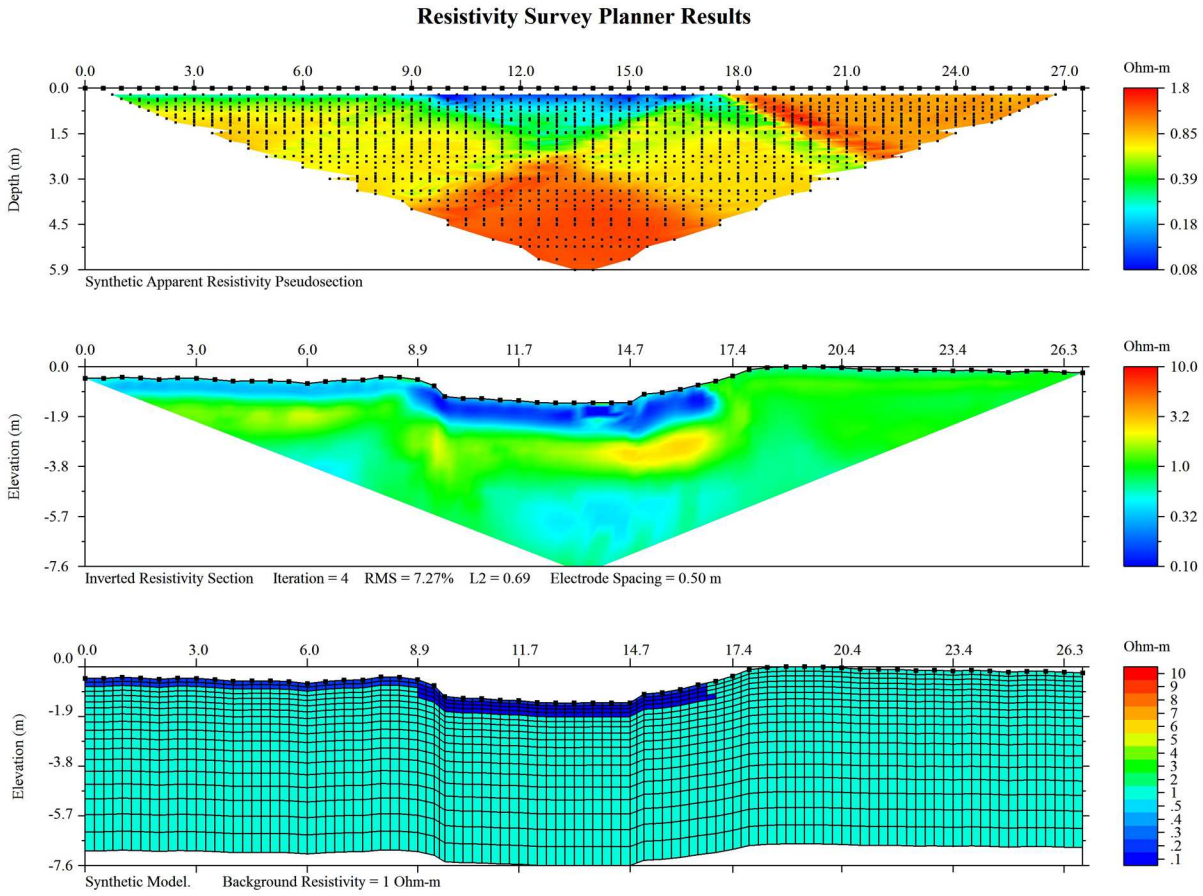

Figure 12: Synthetic Models that where developed using AGI EarthImager software to determine what type of artifacts would be developed having a 1 Ω-m background resistivity and 0.3 Ω-m hyporheic zone. The processed data reveals similarities in artifacts located in the subsurface near the creek banks, high and low resistivity bodies.

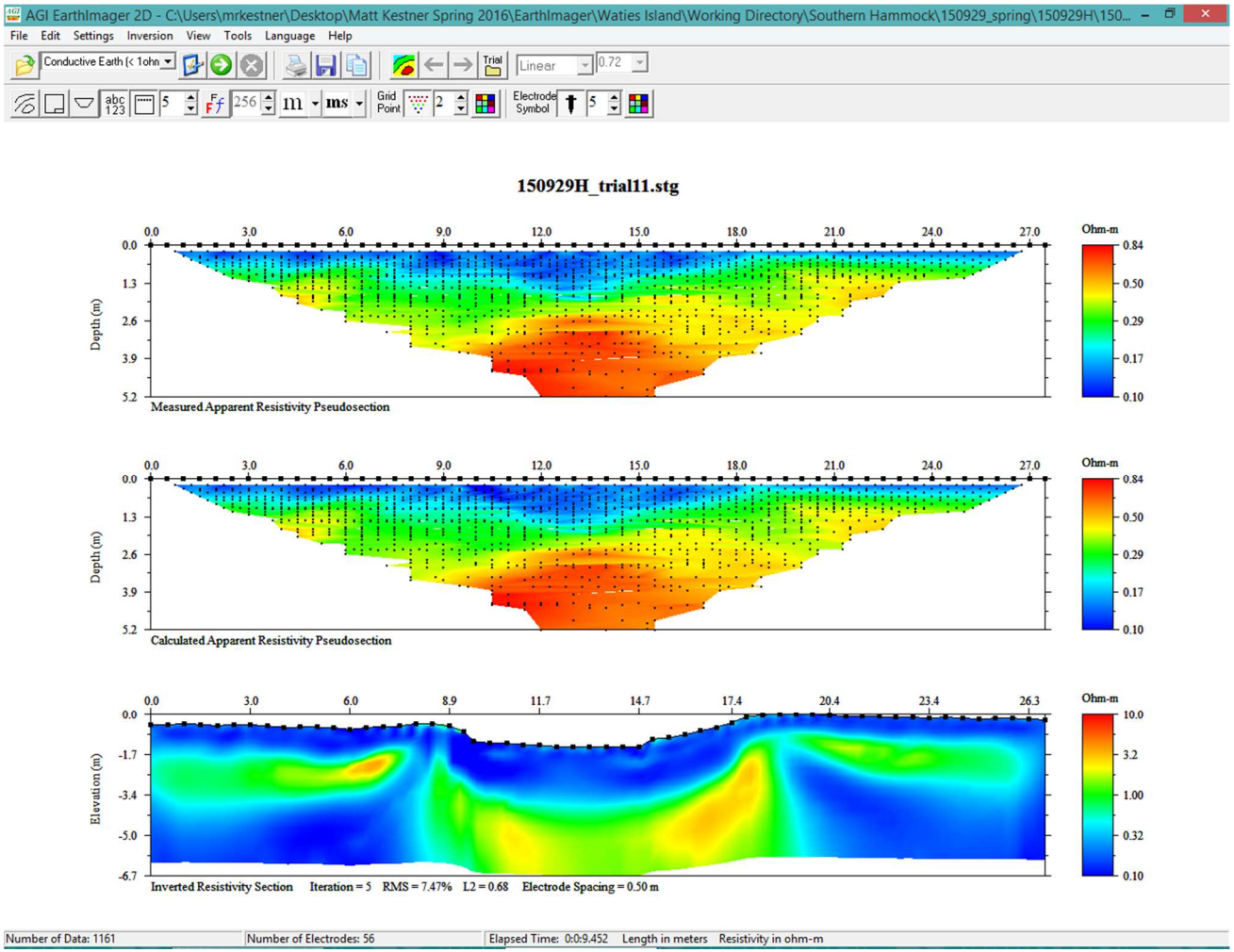

Figure 13: Typical processed Electrical Resistivity data including the Measured Apparent Resistivity Psuedosection at the top followed by the Calculated Apparent Resistivity Psuedosection in the middle, with the interpreted geological cross section, Inverted Resistivity Section at the bottom.

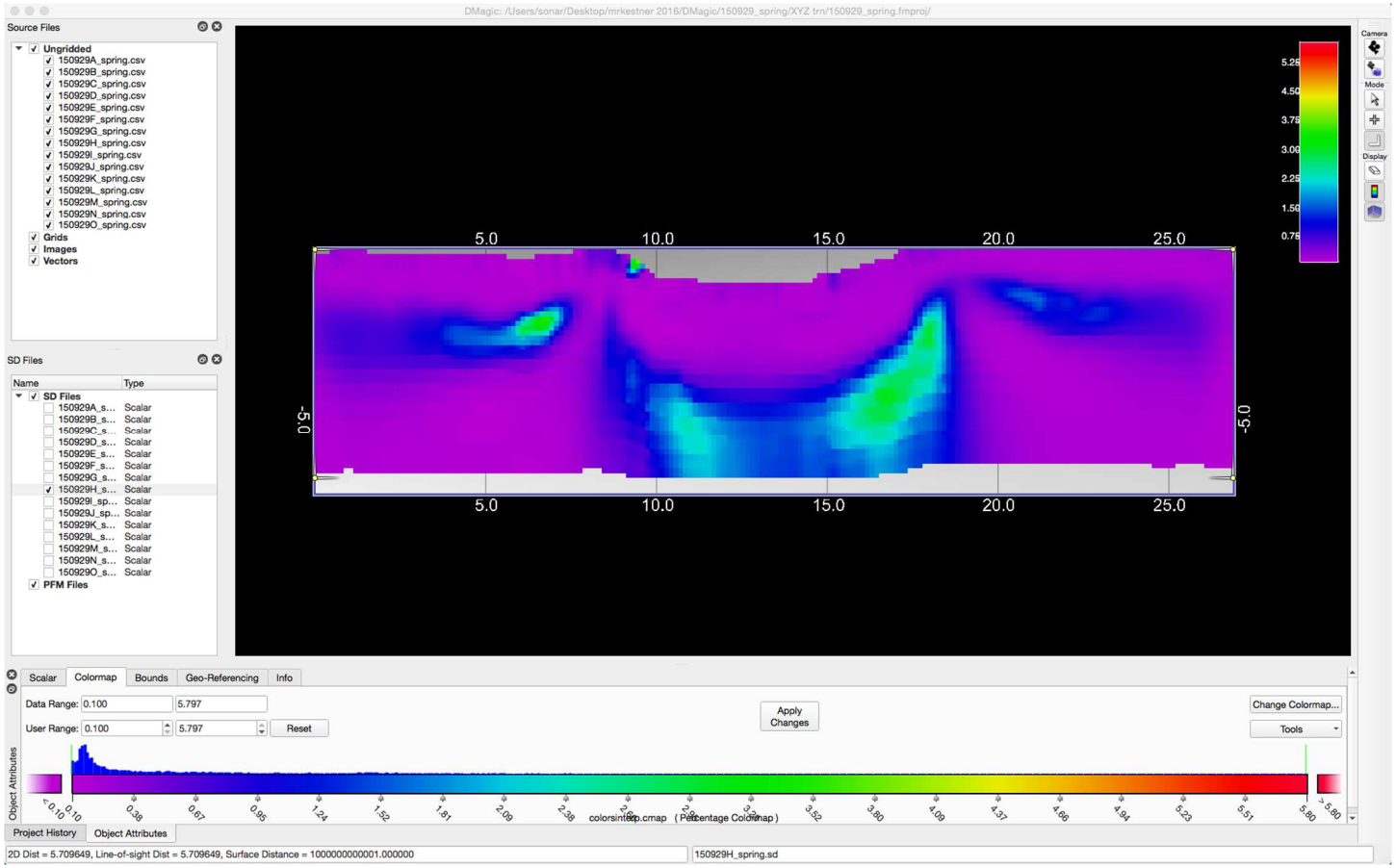

Figure 14: The numerical mesh generation by QPS Fledermaus DMagic.

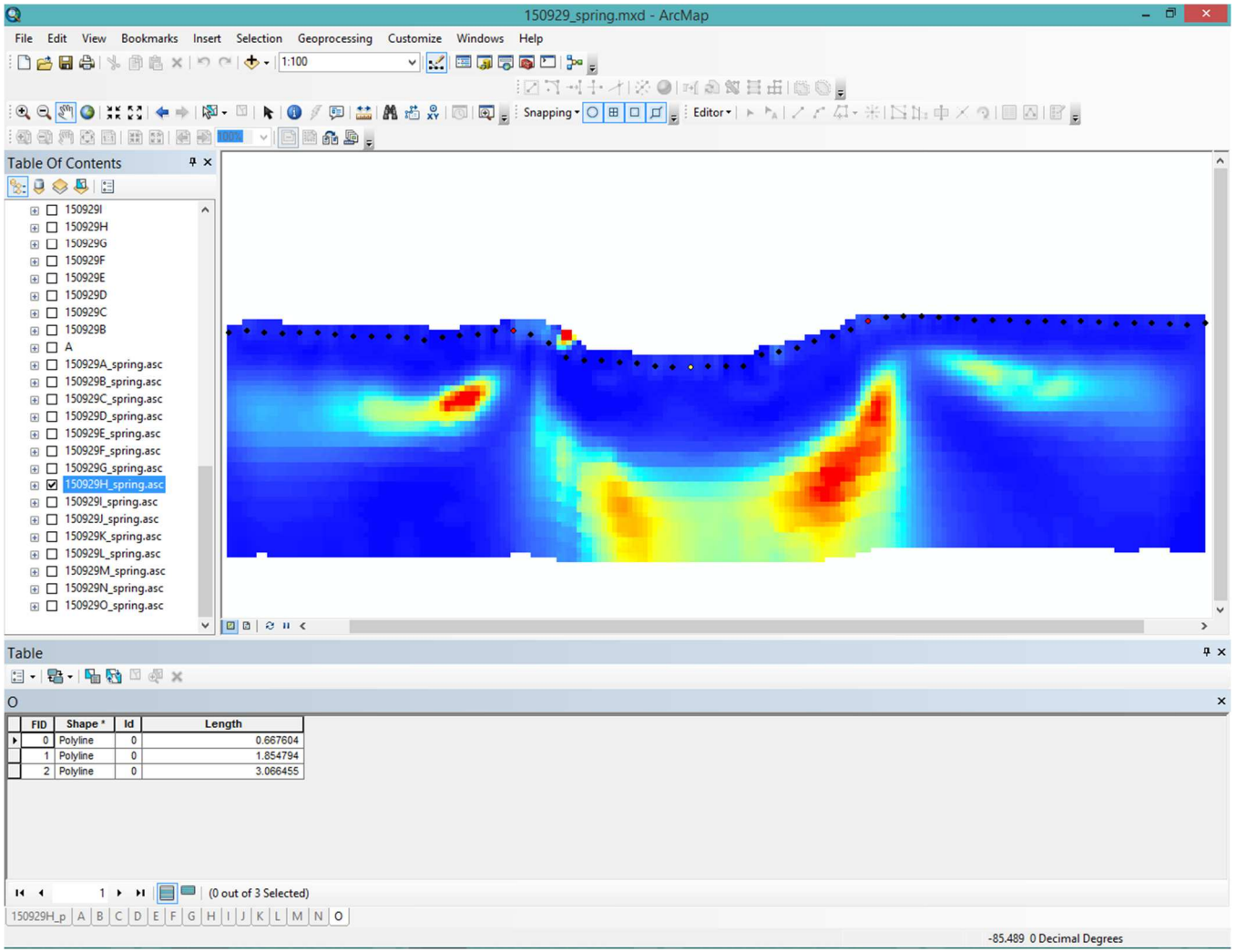

Figure 15: Screenshot of the numerically generated mesh imported from Fledermaus, with the accompanying electrode surface position from the RTK-GPS data.

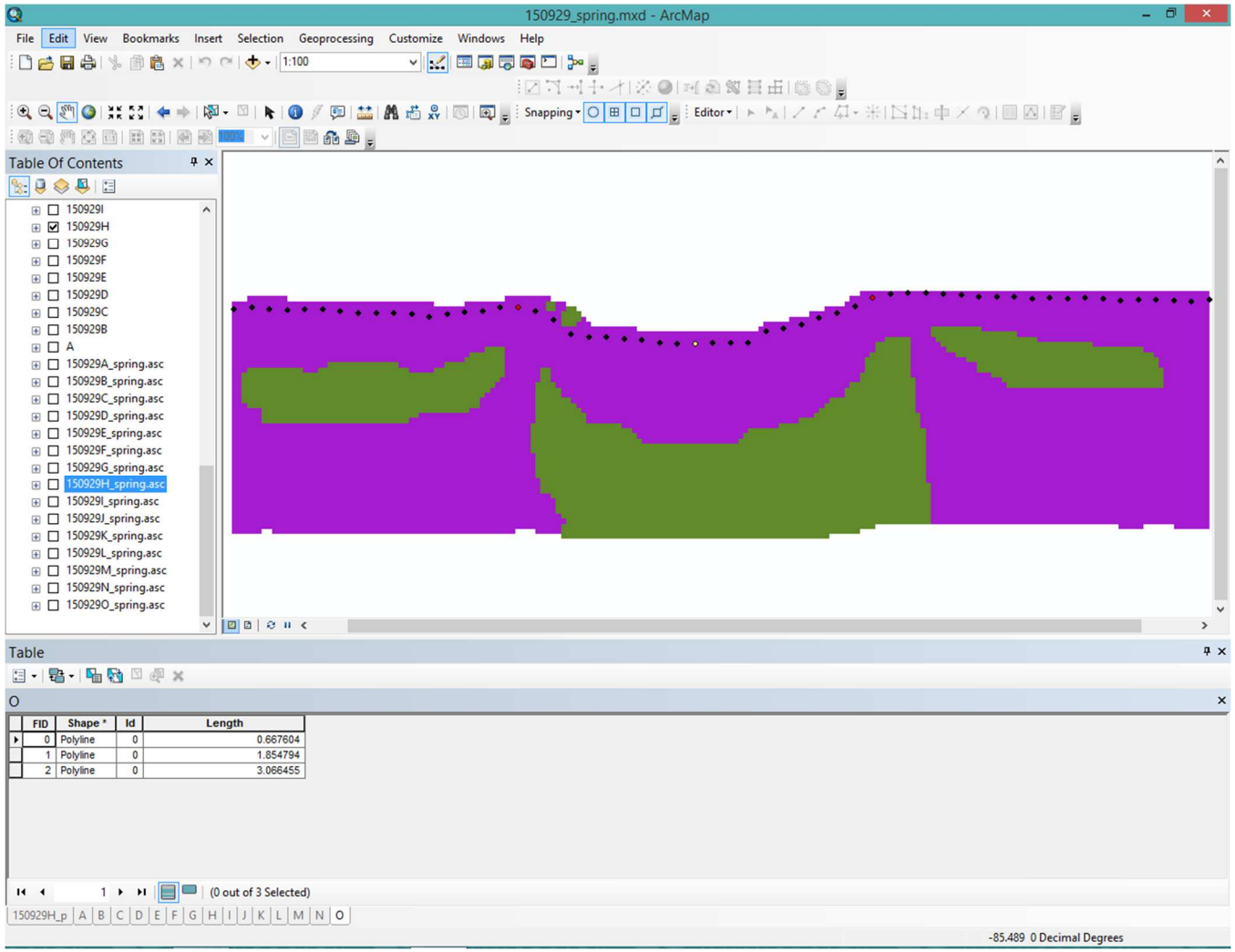

Figure 16: ArcGIS 2-color contour surround the 0.604 Ω-m line that separates the maximum extent of the hyporheic zone and ambient background noise.

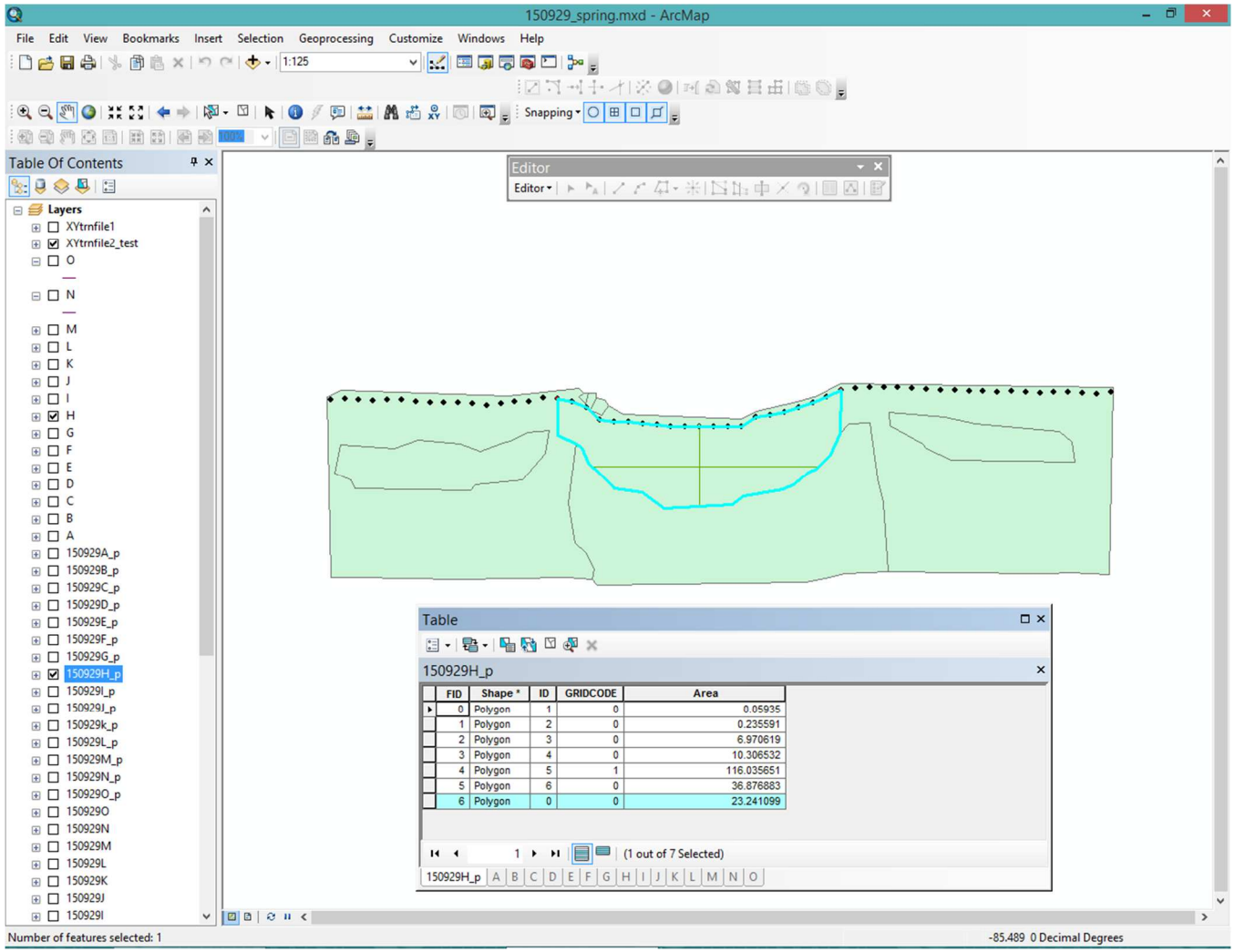

Figure 17: ArcGIS polygon with the drawn area, width and thickness lines, which have been quantitatively recorded.

Figure 18: Sediment core of the modern marsh from Vibracore 5. Note the brownish tint to the sand, plenty of root fragments and vegetation.

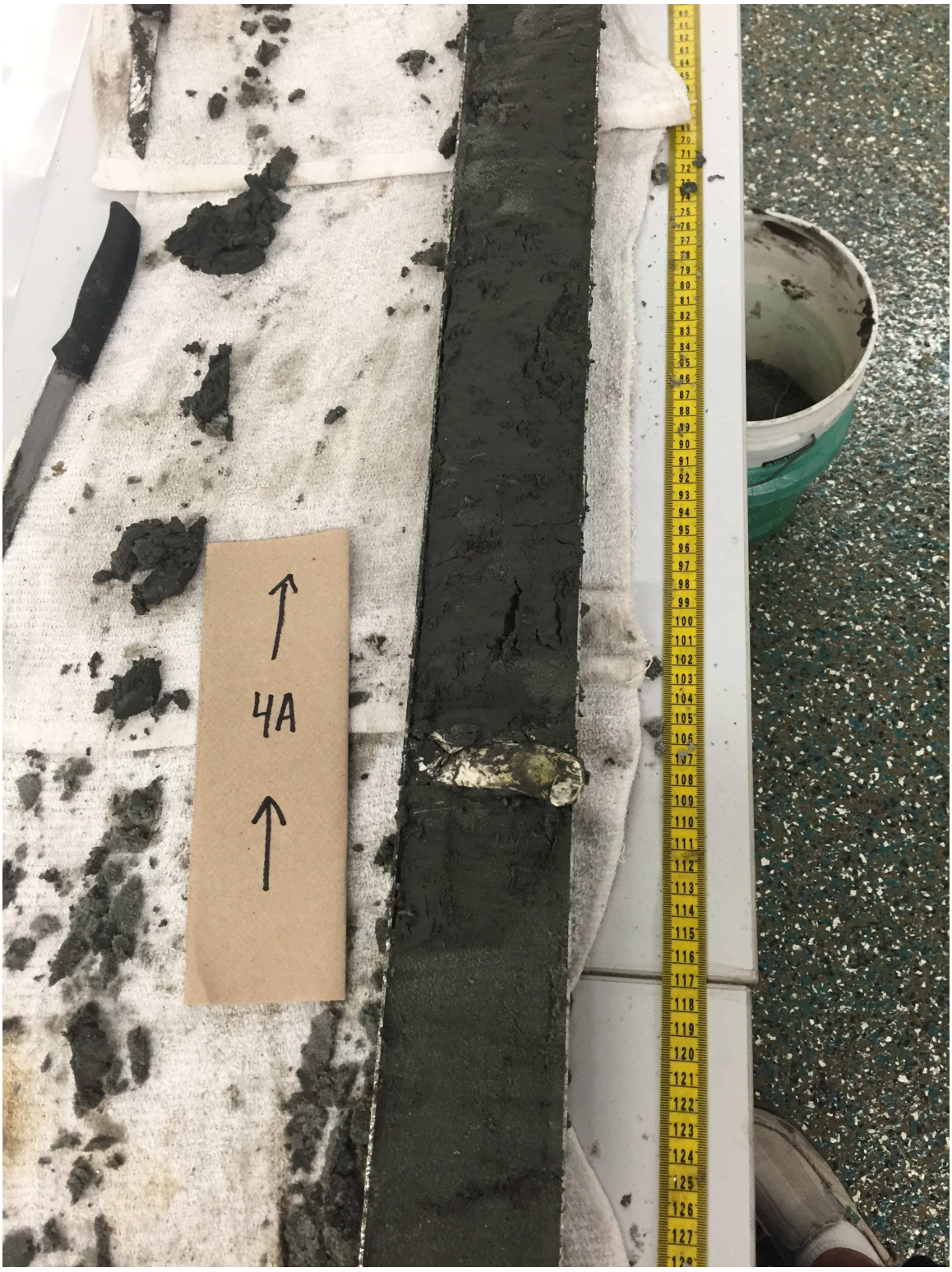

Figure 19: Sediment core of the paleomarsh from Vibracore 4. Note the black color, oyster shell, and root fragments.

Figure 20: Sediment core of the large sand unit from Vibracore 2. There is a presence of large shell fragments, and a massive sandstone unit.

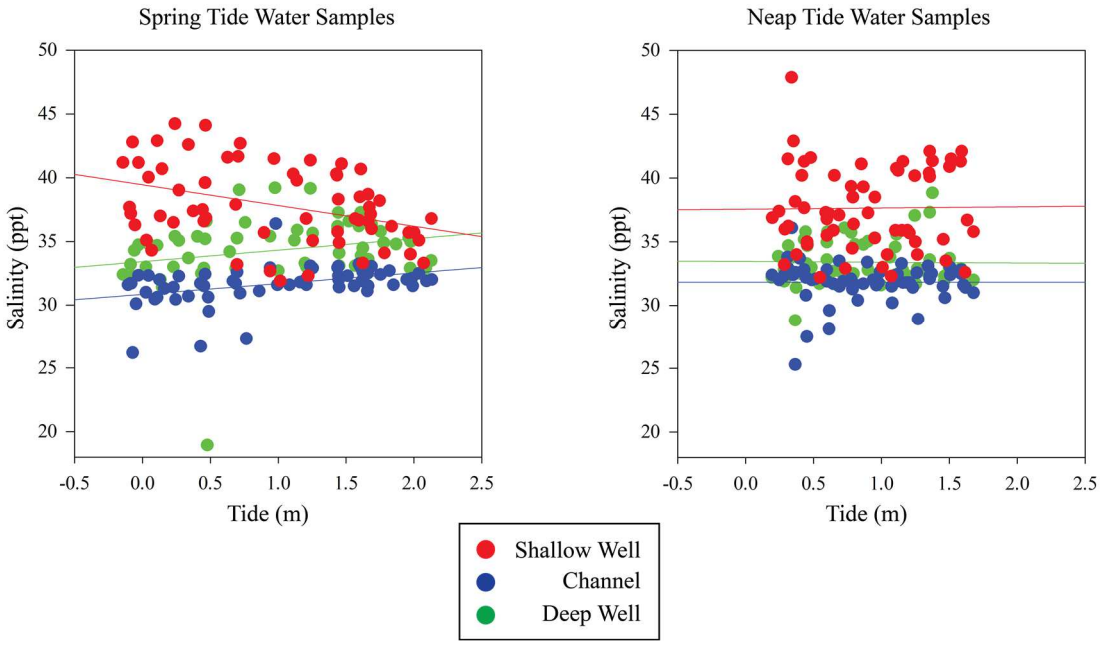

Figure 21: Fortnightly differences in salinity at the study site during ERT measurement days.

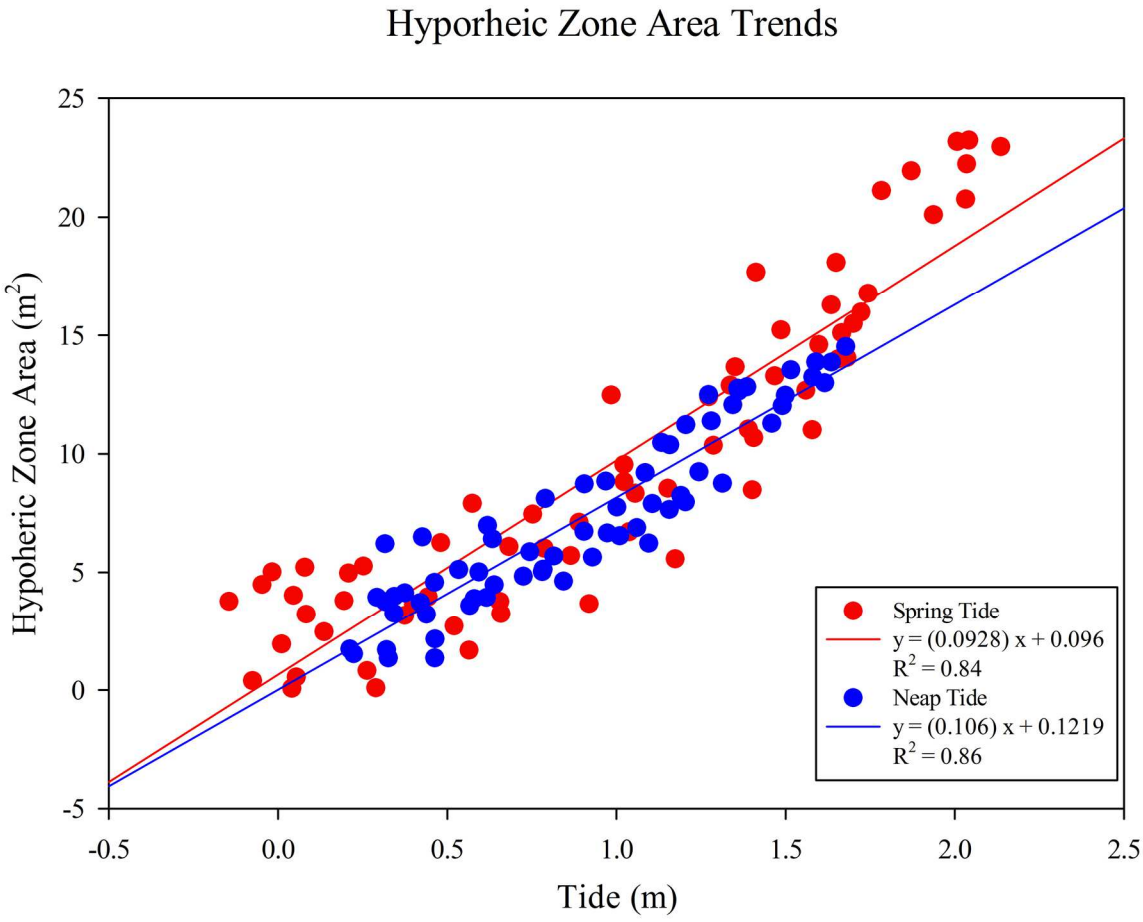

Figure 22: The linear relationship between hyporheic zone area and tidal height.

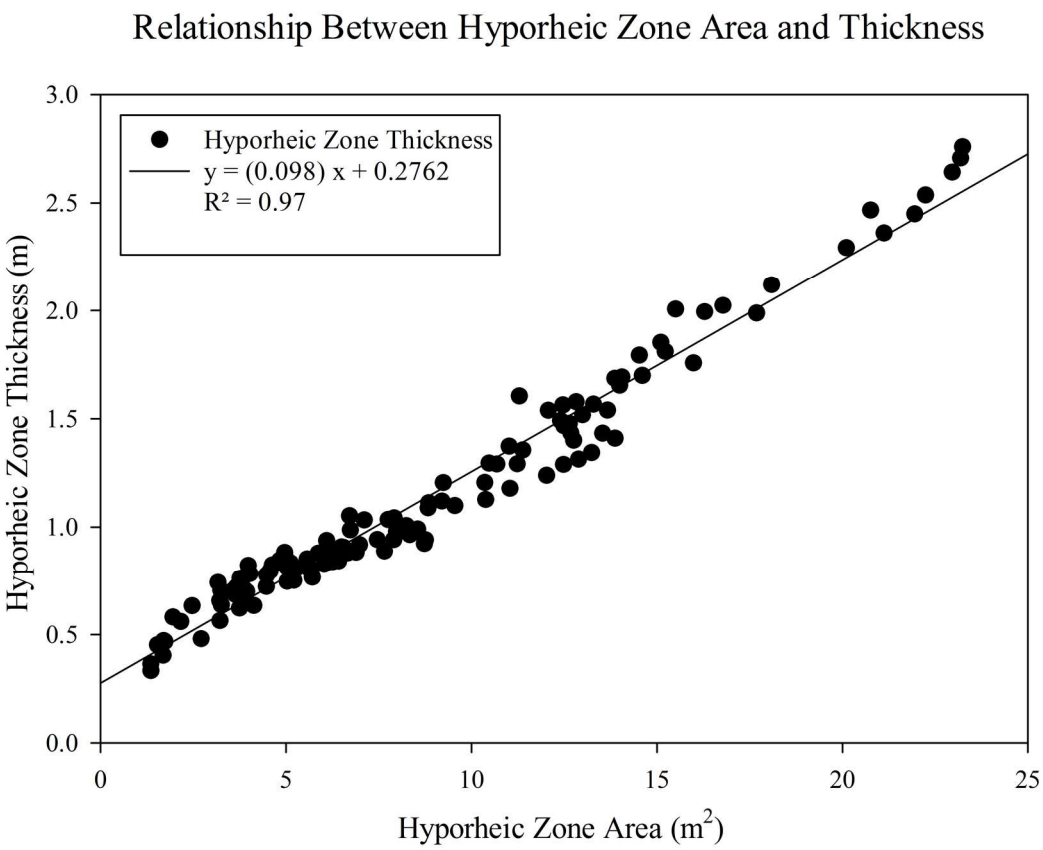

Figure 23: The linear relationship between hyporheic zone thickness and area.

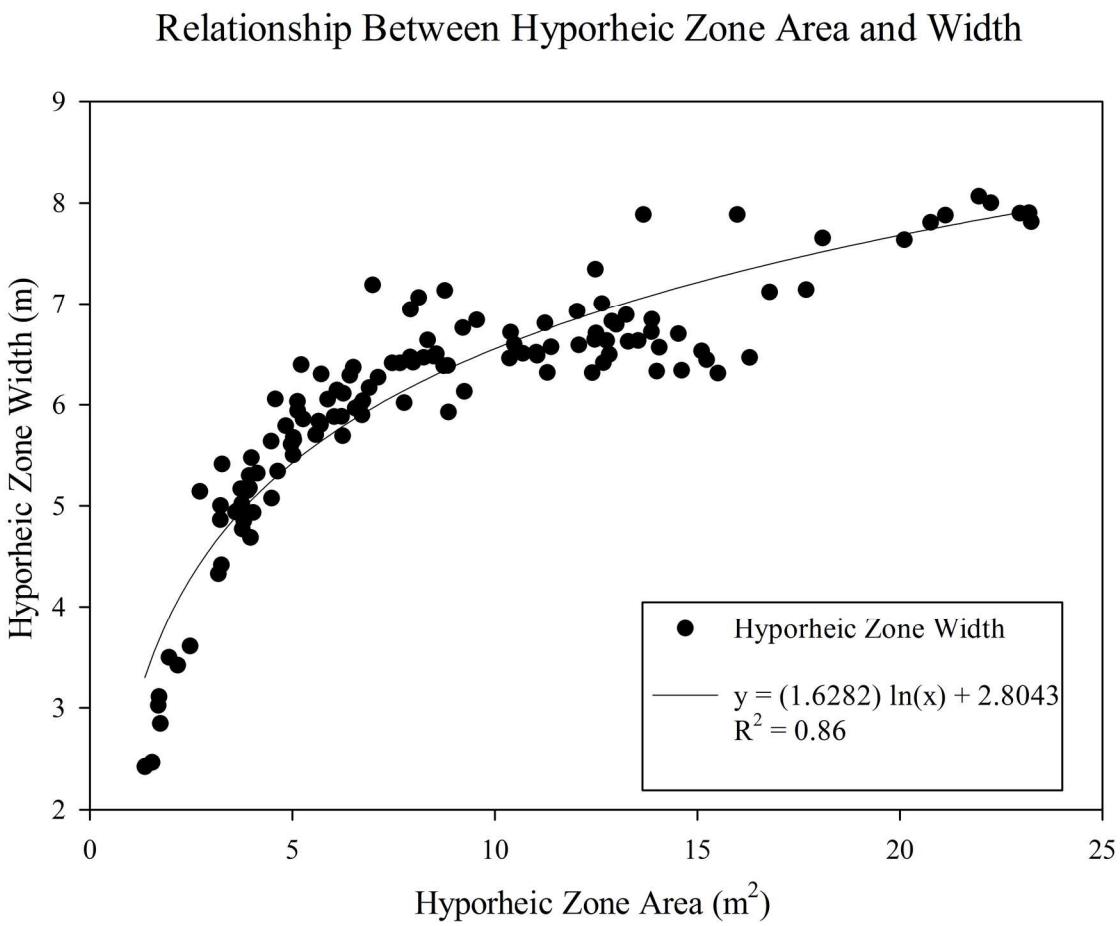

Figure 24: The logarithmic relationship between hyporheic zone width and area

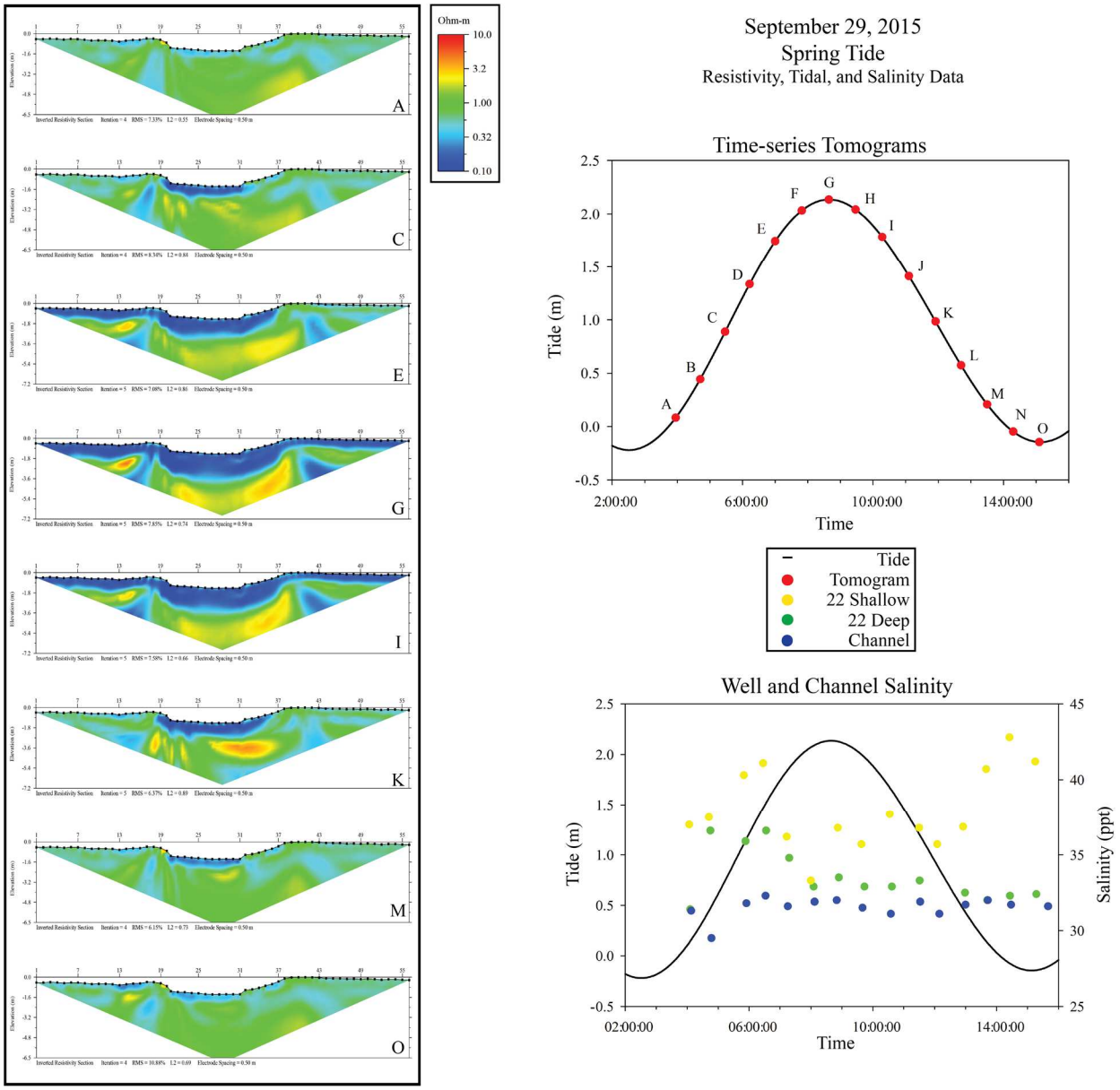

Figure 25: 150929_Spring. The effect of hyporheic zone processes on the shallow water well. As the tide rises and expands the hyporheic zone, the salinity in the shallow well goes from hypersaline to channel water salinity.

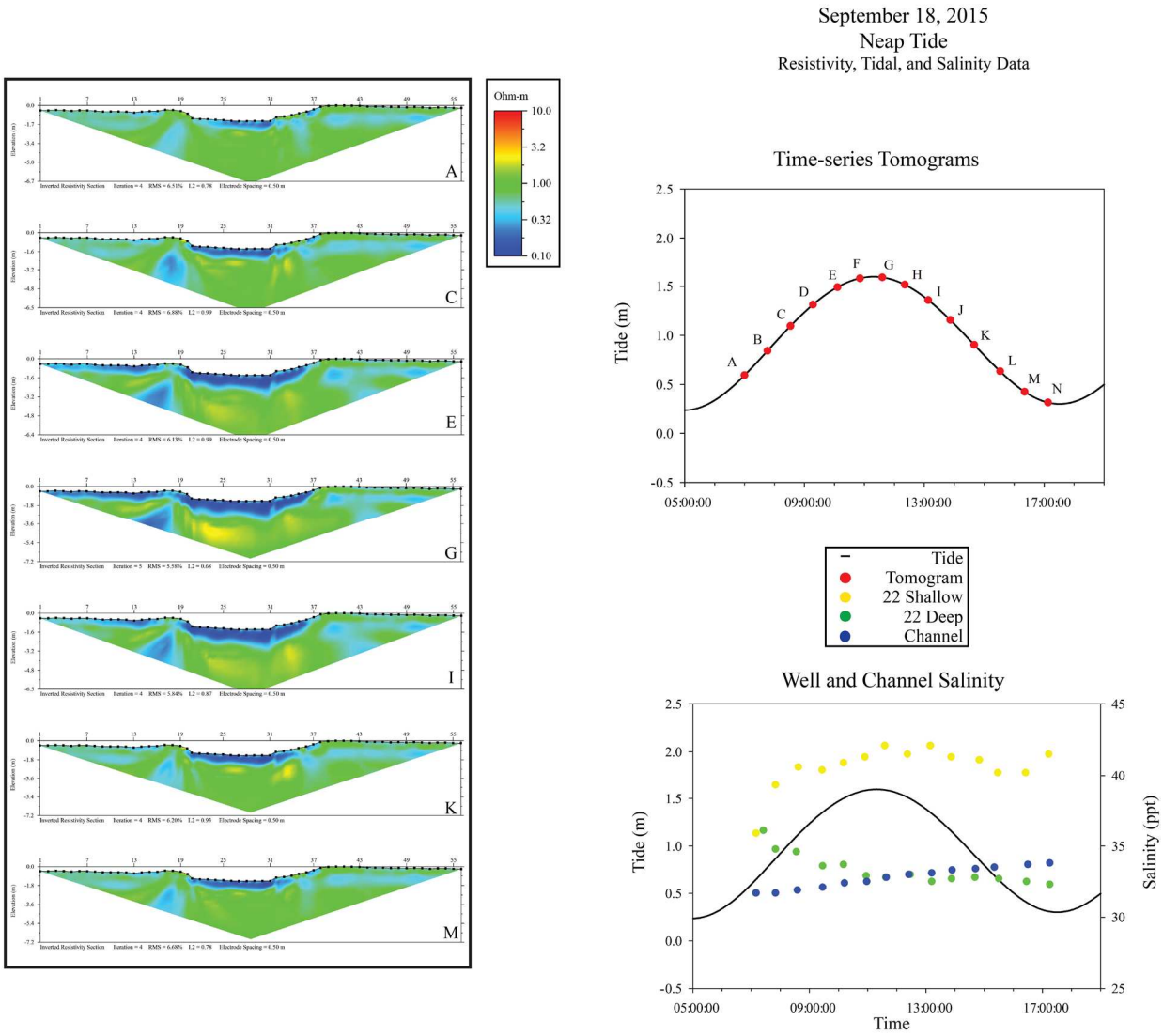

Figure 26: 150918_Neap. The small extent of the hyporheic zone expanding into and out of the creek bank, does not affect the salinity of the wells.

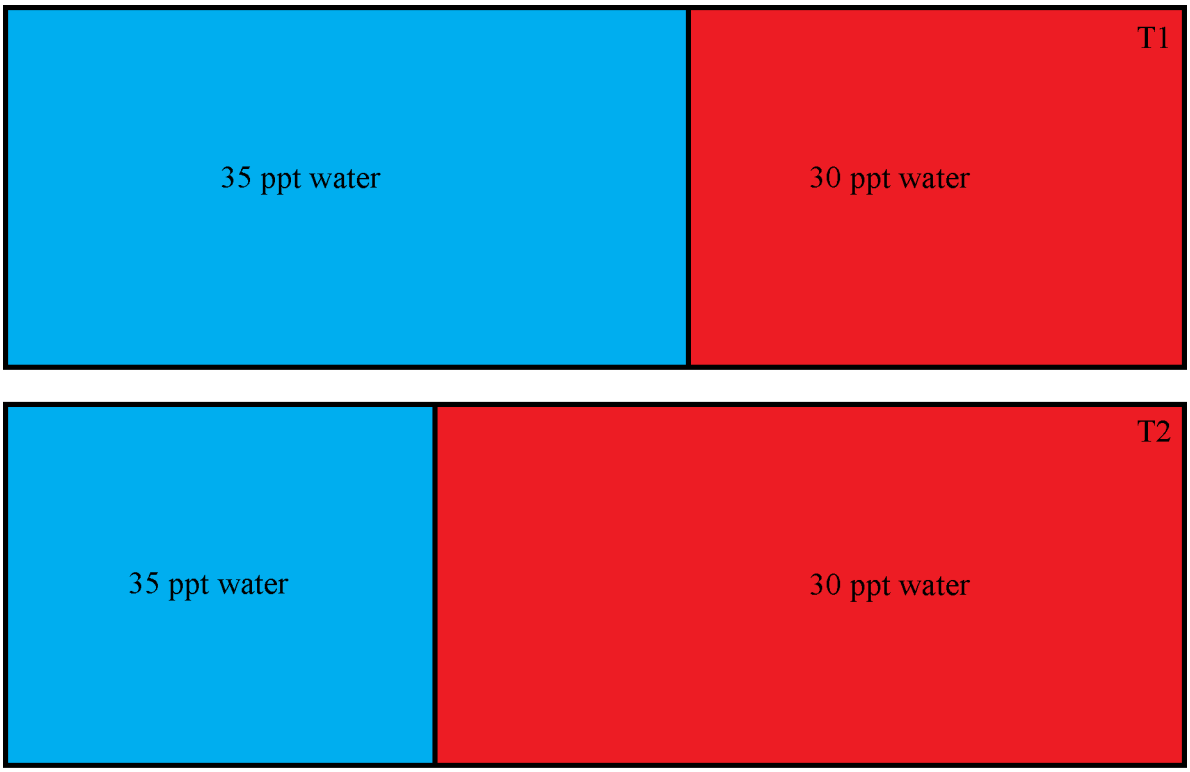

Figure 27: The only assumption that can be made about a boundary imaged in the resistivity tomograms from one image to another is that the boundary has moved. There can be no assumption to the flow direction or velocity of water moving through the area.

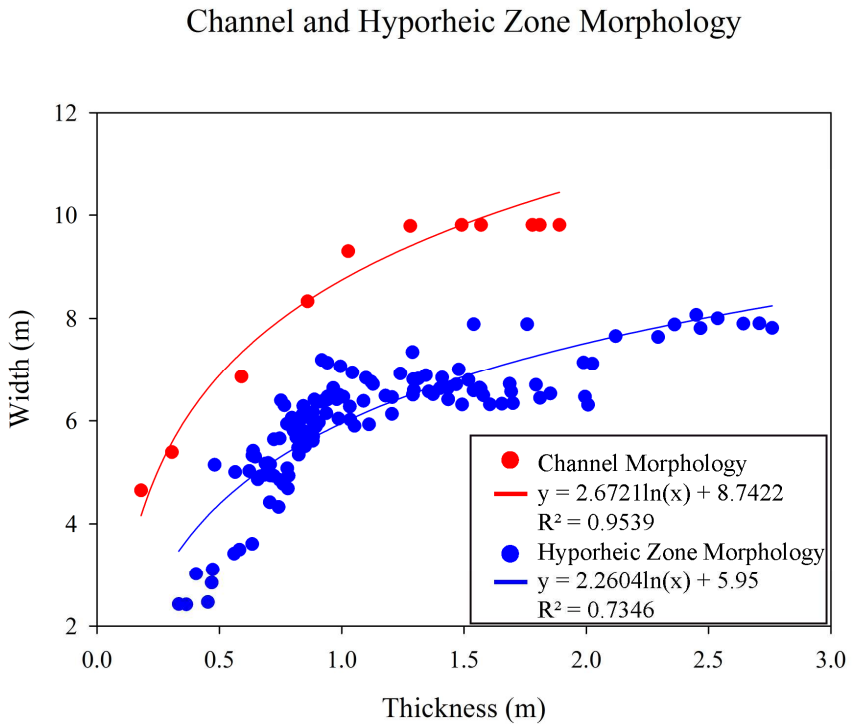

Figure 28: Comparison of the channel morphology and the subsurface hyporheic zone morphology.

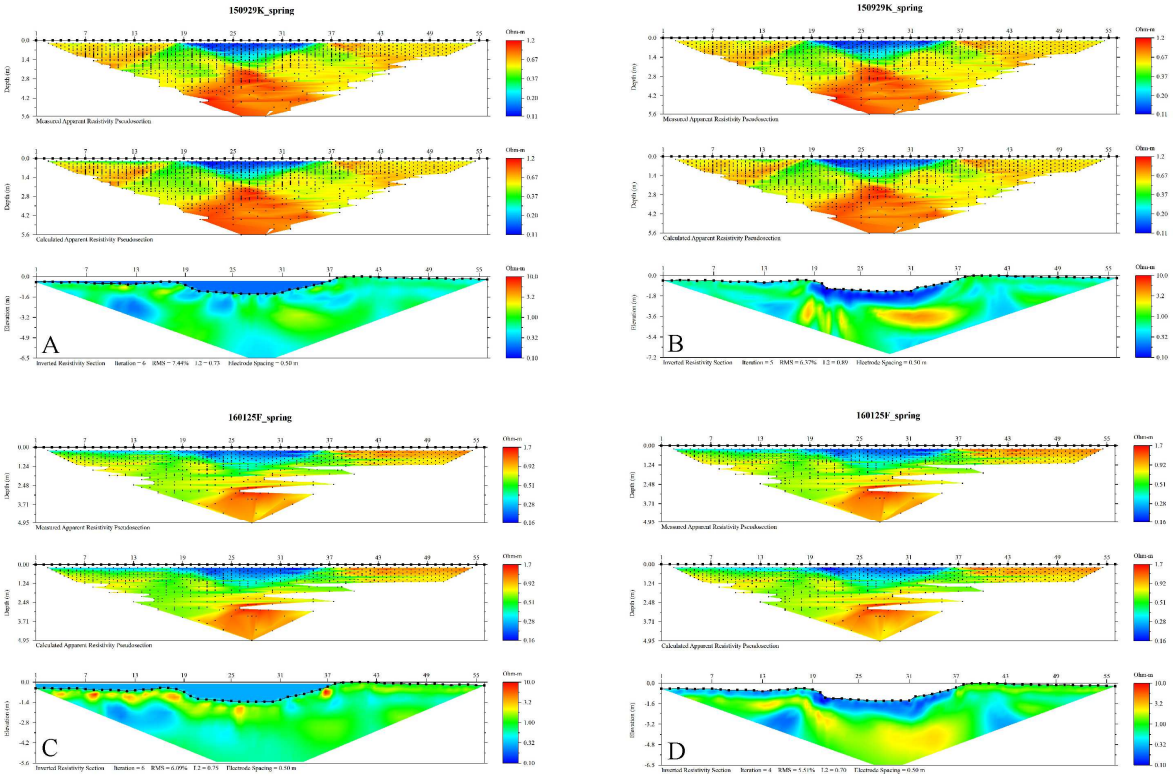

Figure 29: September and January tomogram images with and without water layers to analyze a simplified uniform mixing zone (B and D) and a more complex mixing zone with the possibility of temperature effects as the changing unit.

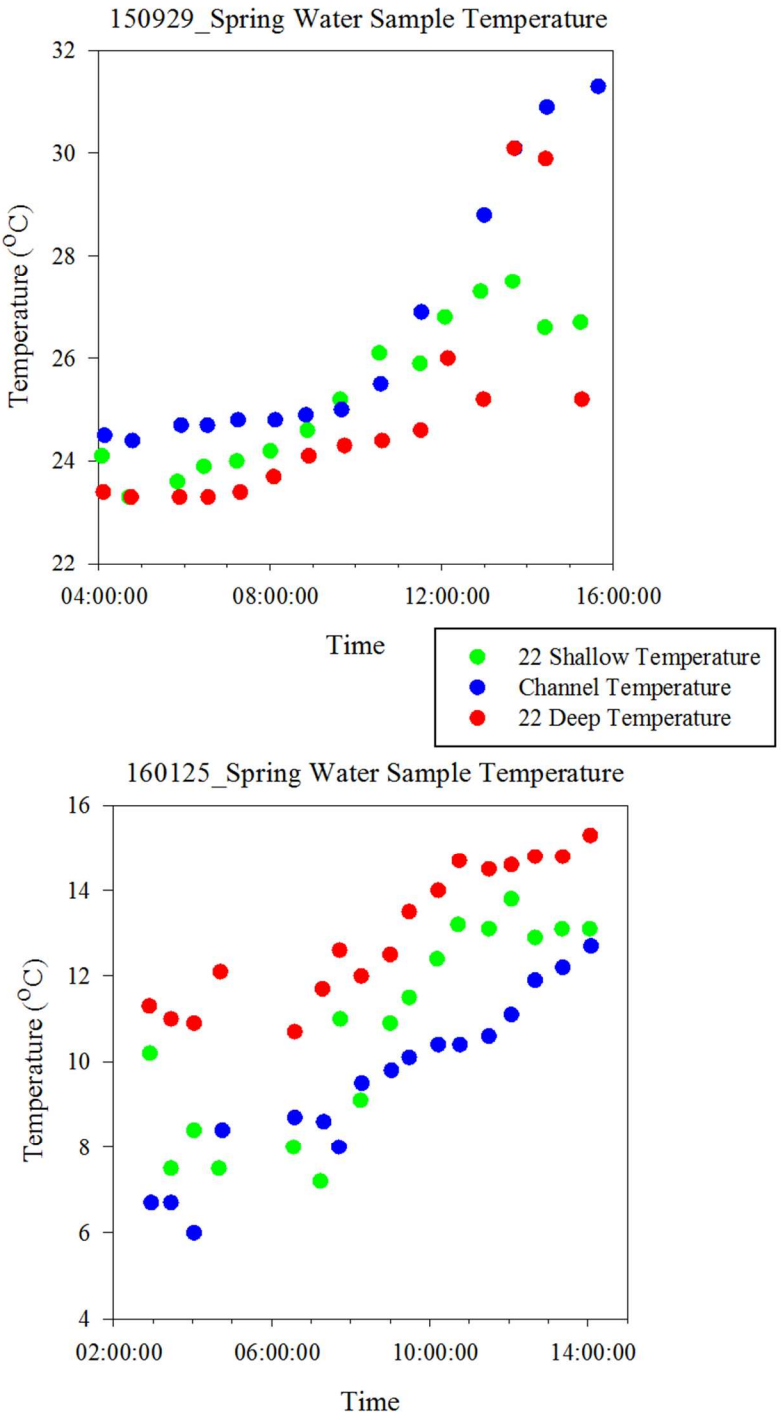

Figure 30: Late summer pore water and channel water temperatures to suggest warm channel waters entering a cooler mass causing a lowering in resistivity values. The opposite occurs during the winter with cooler channel waters mixing with warmer subsurface waters causing higher resistivity readings.

9. Appendices

Appendix A

Electrical Resistivity Time-series Tomograms:

The following data set contains the eight data collection days. They appear in chronological order, starting with September 18, 2015 and finishing with January 31, 2016. There is a total of eight field days containing four spring tides and four neap tides. Each image contains a data set that took between 35 – 45 minutes to collect. Measurements for each field day started around low tide and finished around low tide. Each image has been processed using AGI EarthImager 2D and has had the scale set between 0.1 – 10 Ω-m, with 256 colors between the resistivity range. This made for visually appealing images, and the hyporheic zone can easily be identified as the maximum extent of blue, with the ambient background color of green. Accompanying the time series tomogram images is a scale bar, as well as a graph showing the tidal range for the data set with coinciding data points representing the midpoint of each tomogram image.

150918_Neap Tomograms A - E

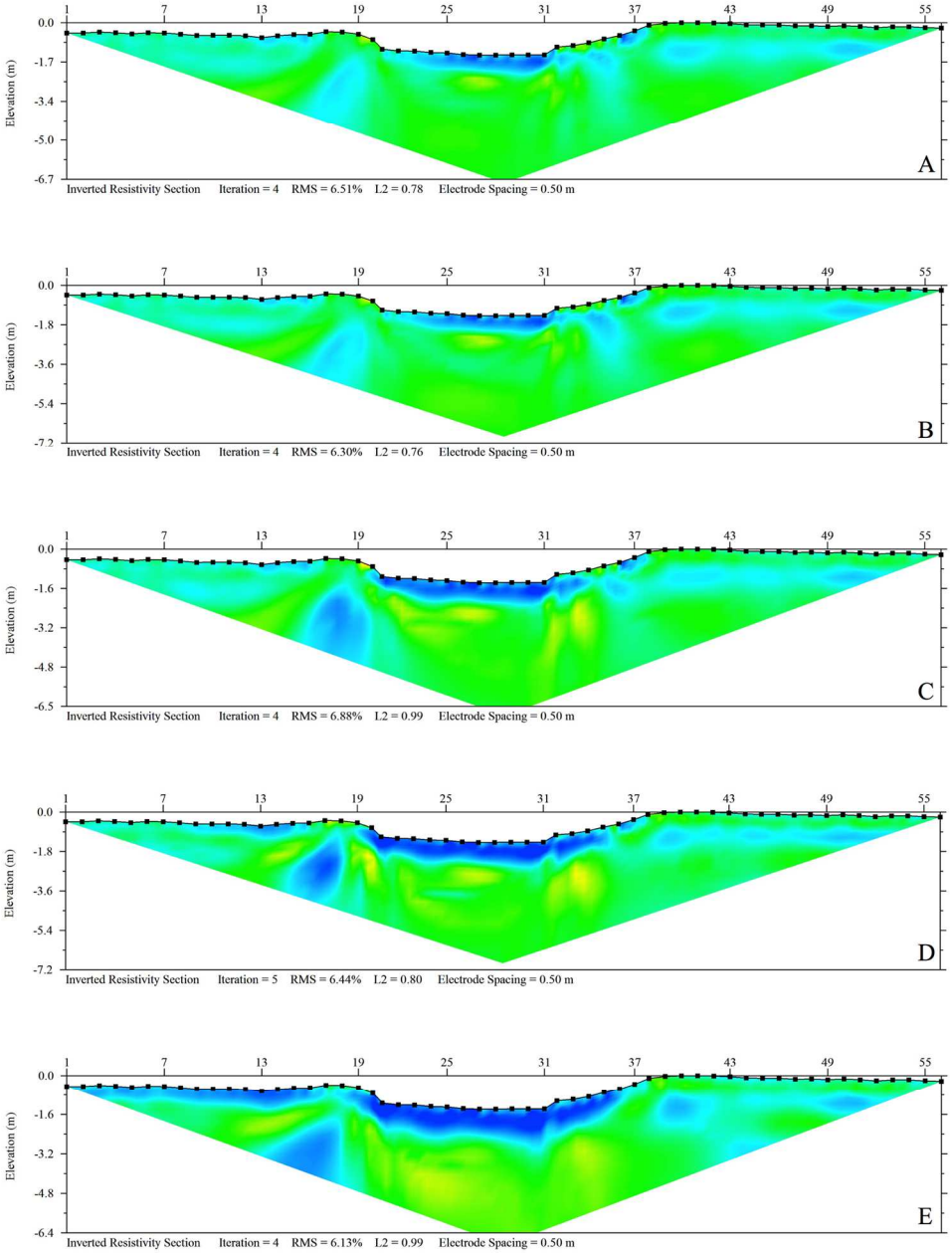

150918_Neap Tomograms F - J

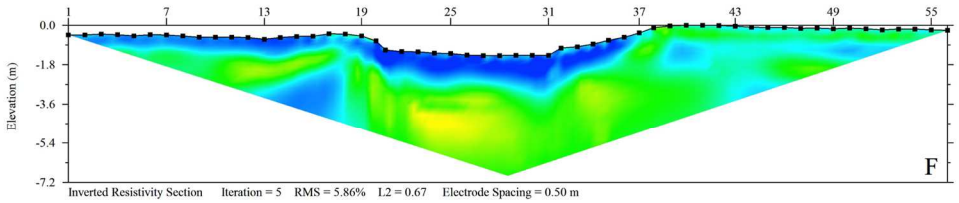

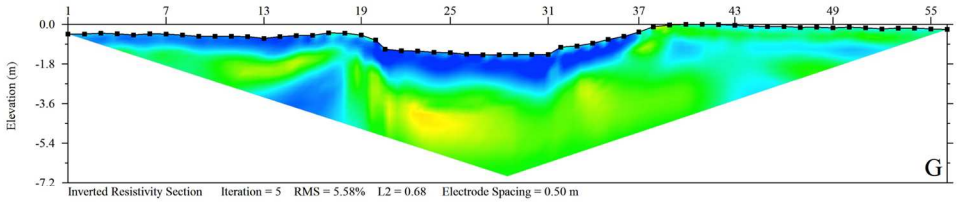

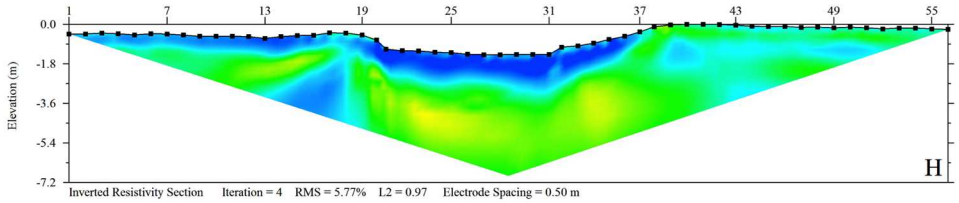

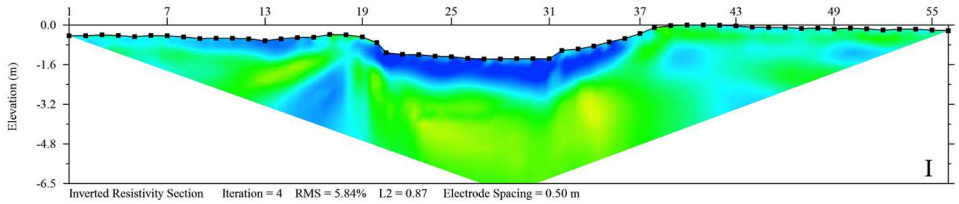

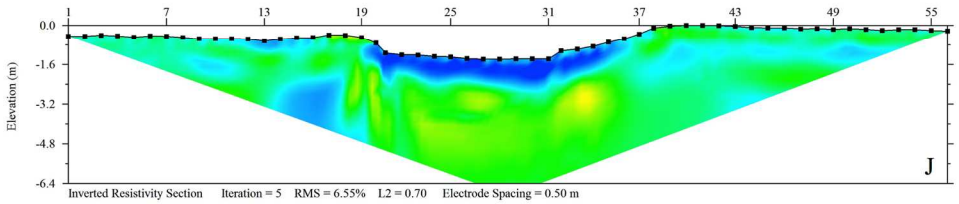

150918_Neap Tomograms K - N

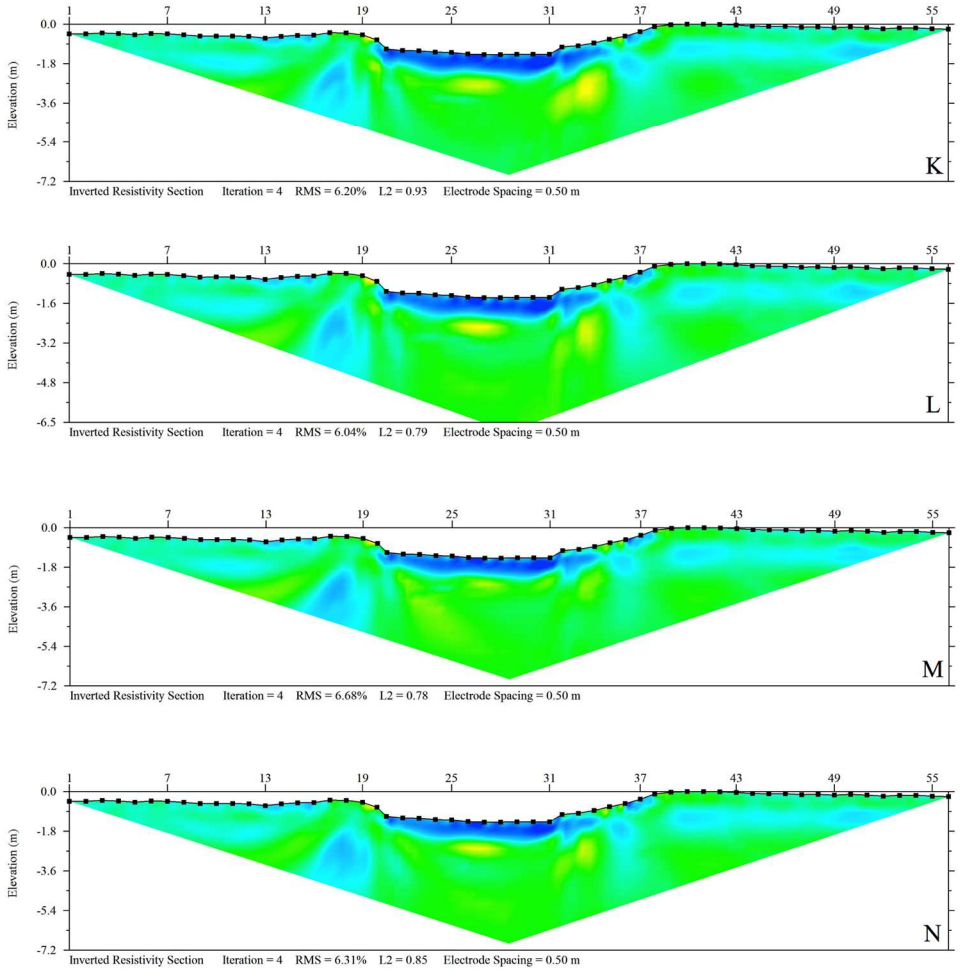

150918_Neap Tomogram Tidal and Scale Information

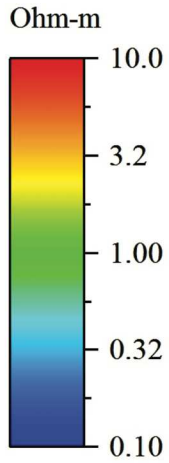

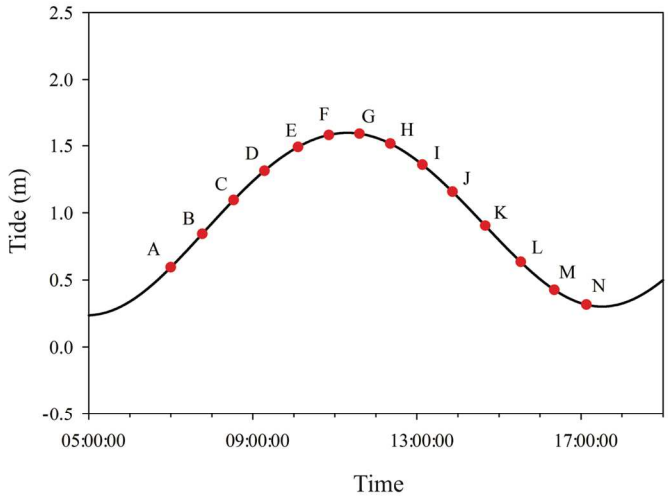

150929_Spring Tomograms A - E

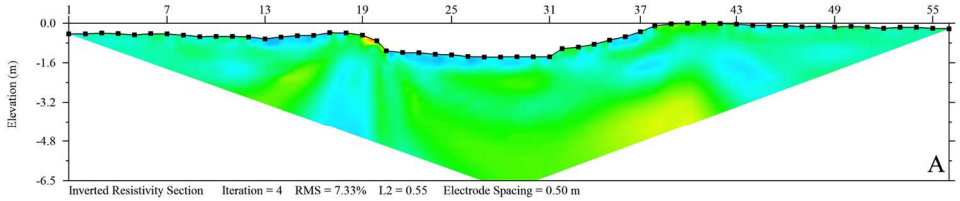

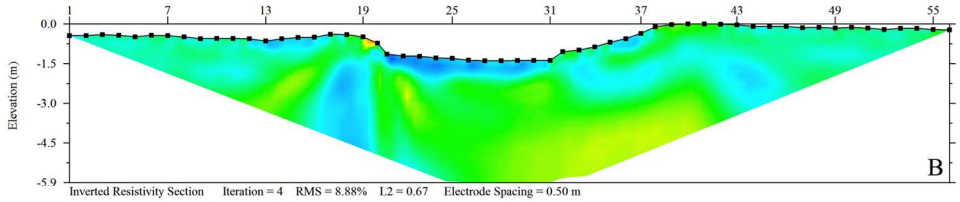

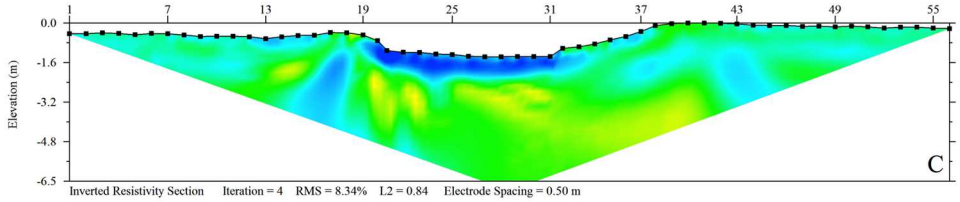

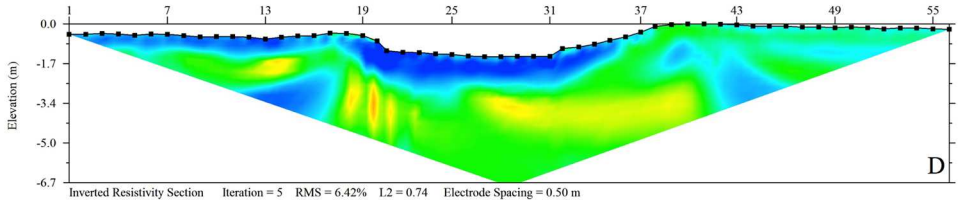

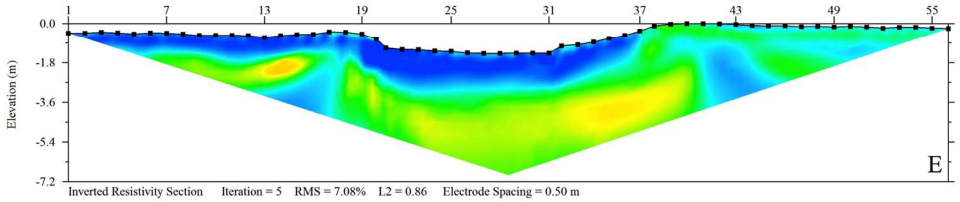

150929_Spring Tomograms F - J

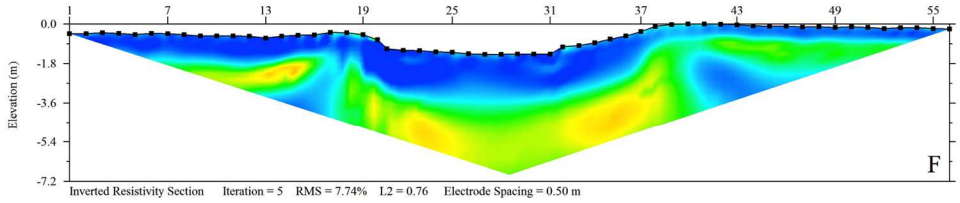

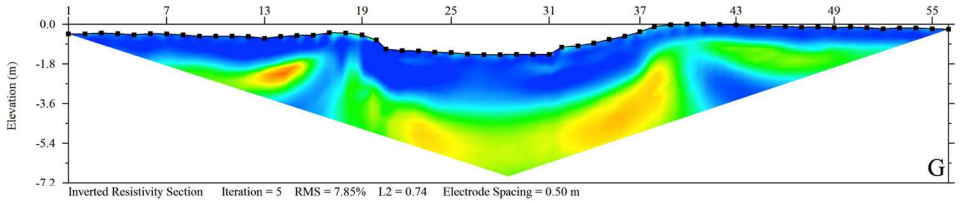

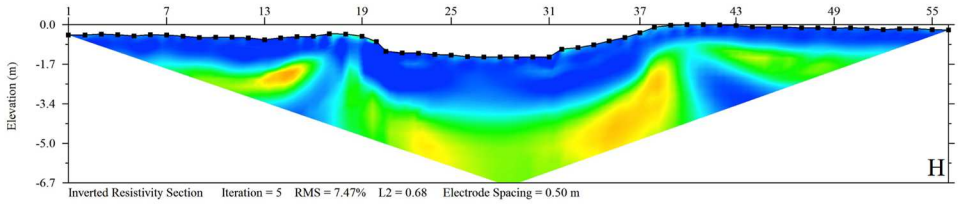

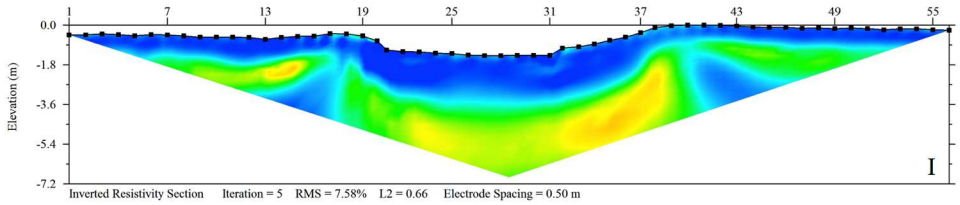

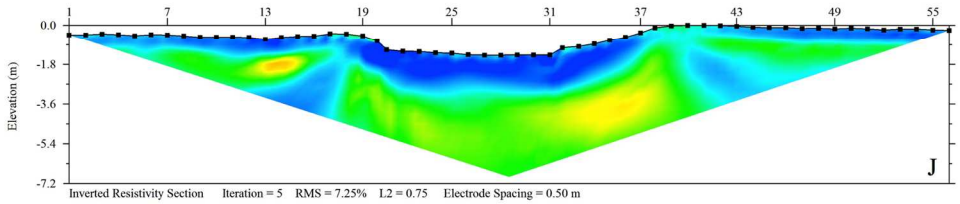

150929_Spring Tomograms K - O

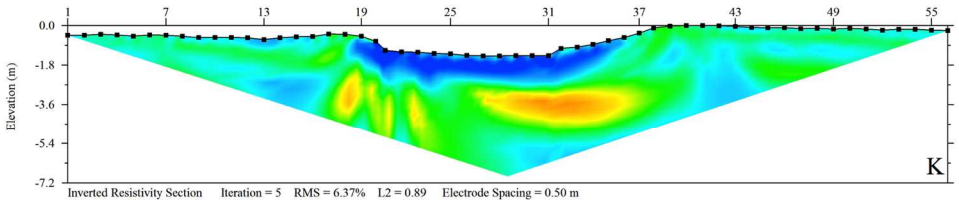

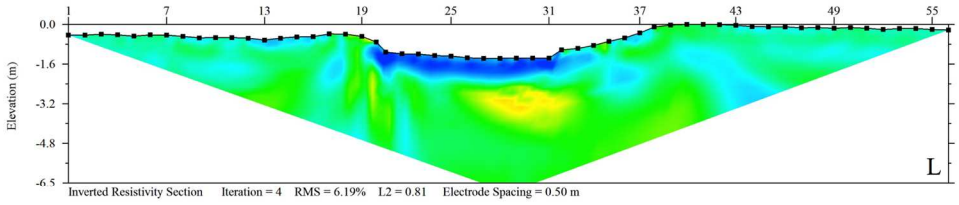

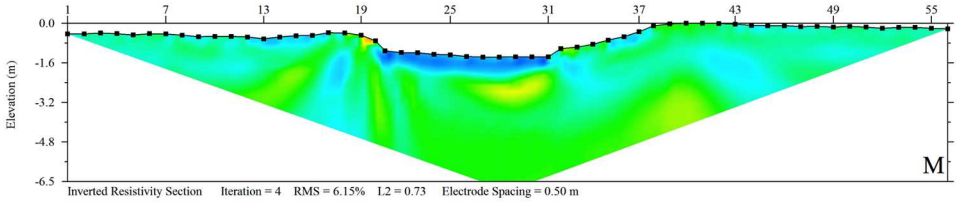

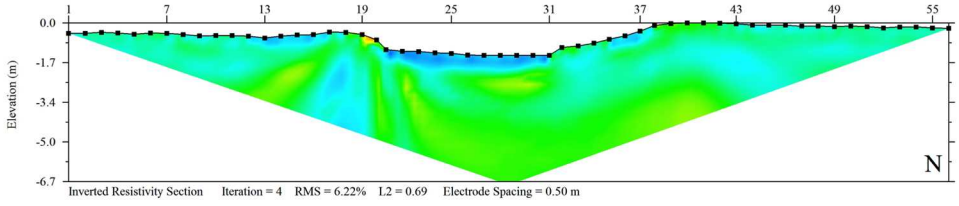

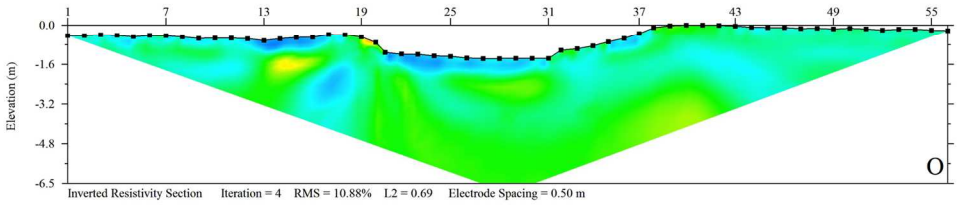

150929_Spring Tomogram Tidal and Scale Information

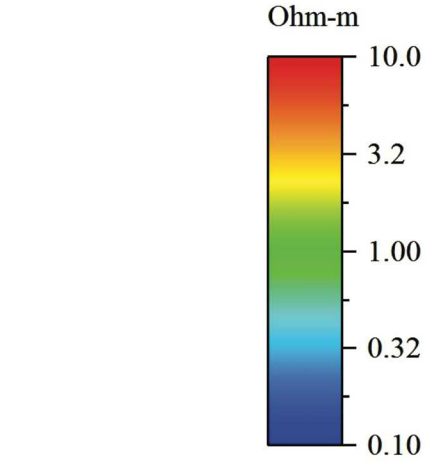

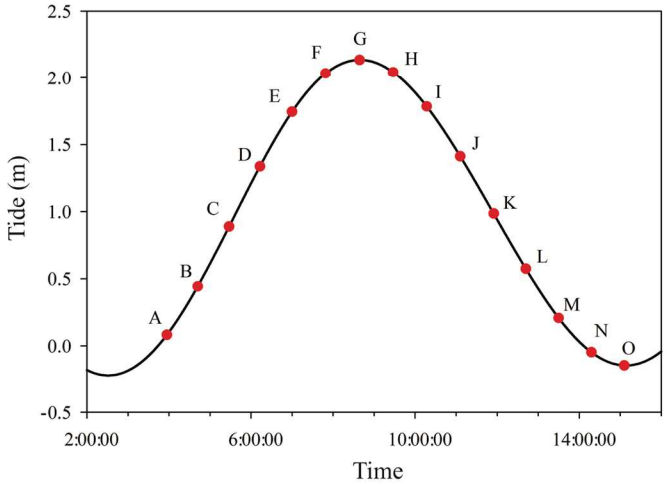

151020_Neap Tomograms A - E

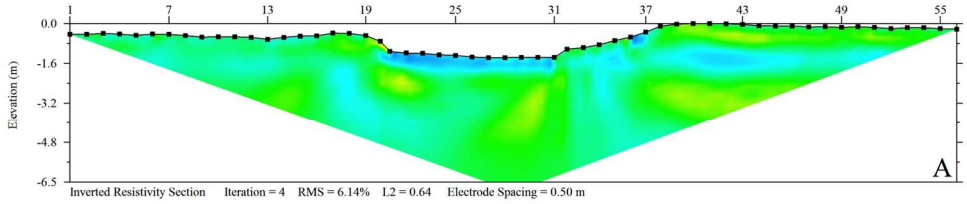

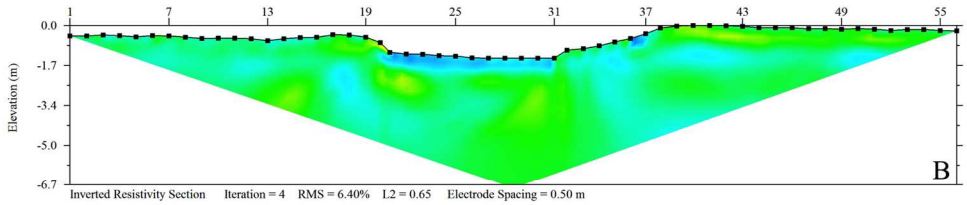

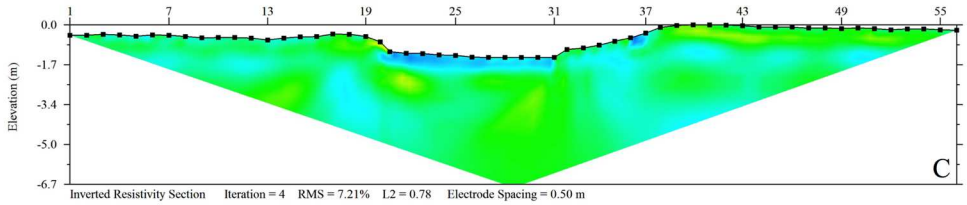

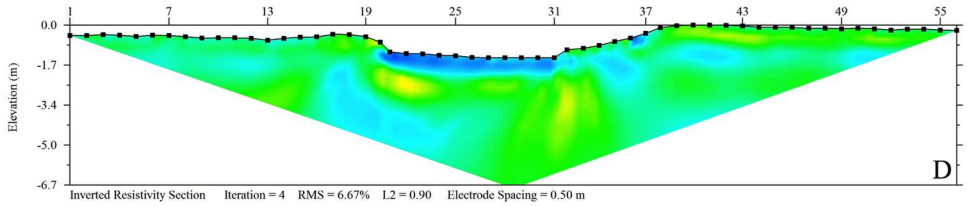

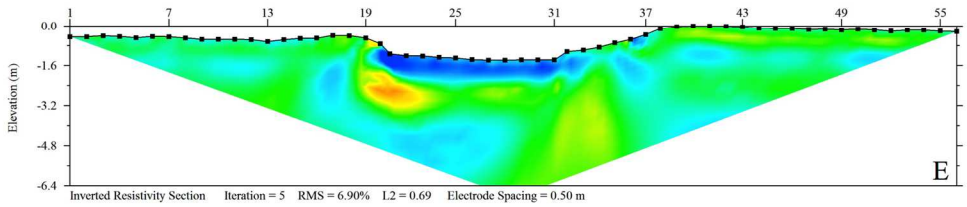

151020_Neap Tomograms F - J

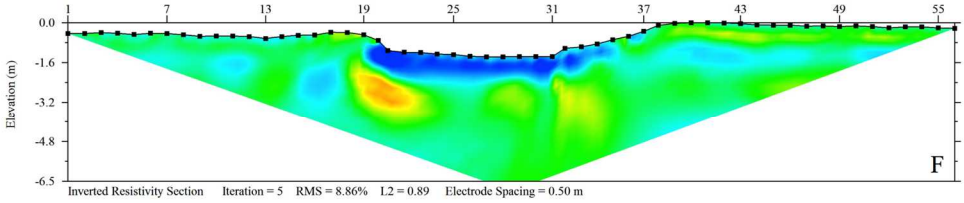

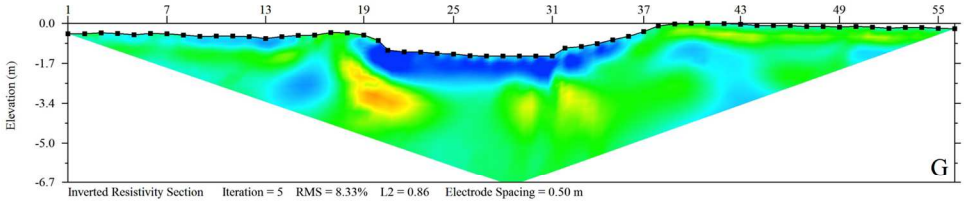

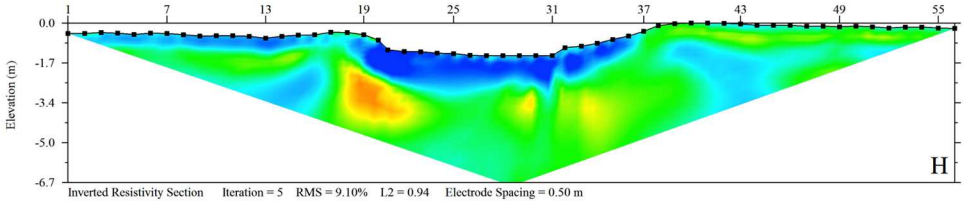

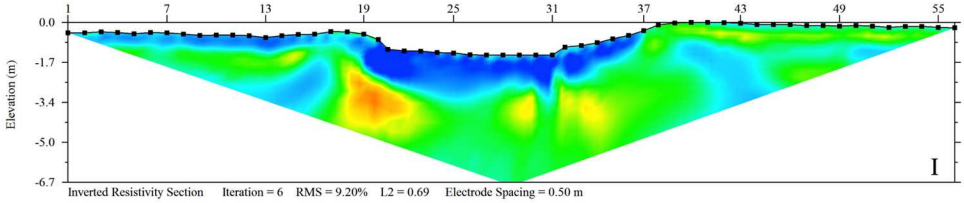

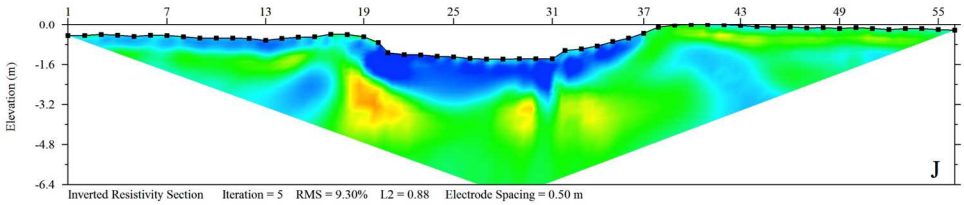

151020_Neap Tomograms K - O

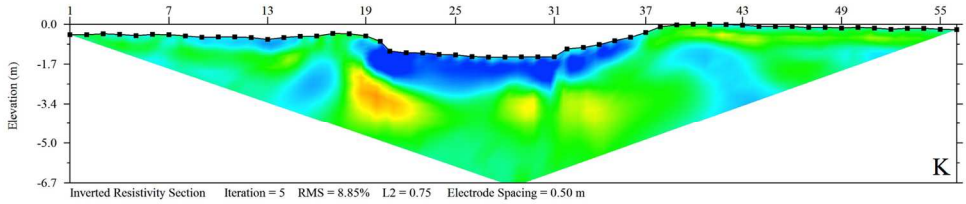

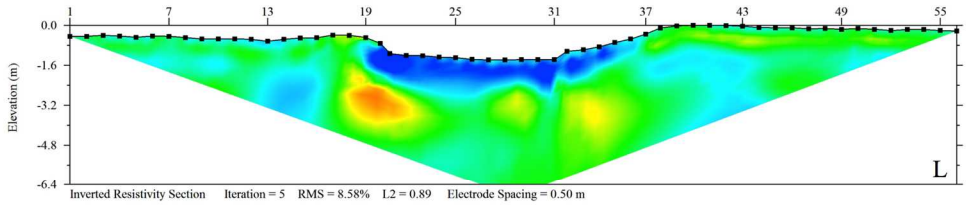

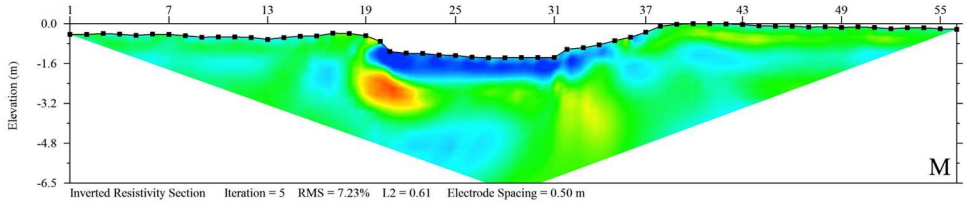

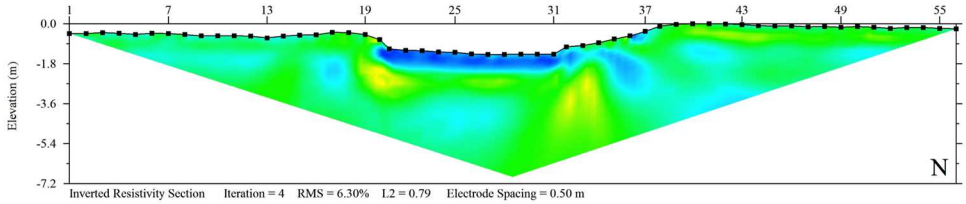

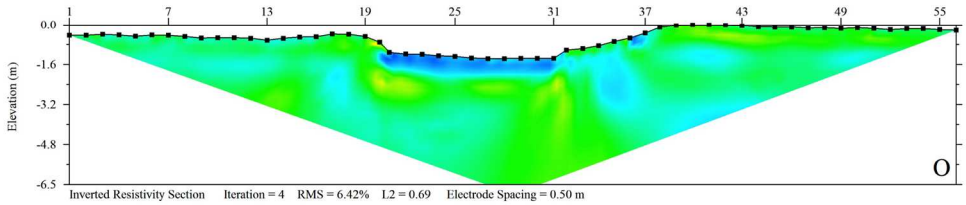

151020_Neap Tomograms P - Q

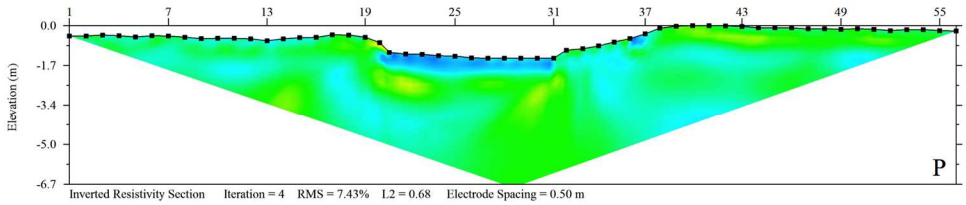

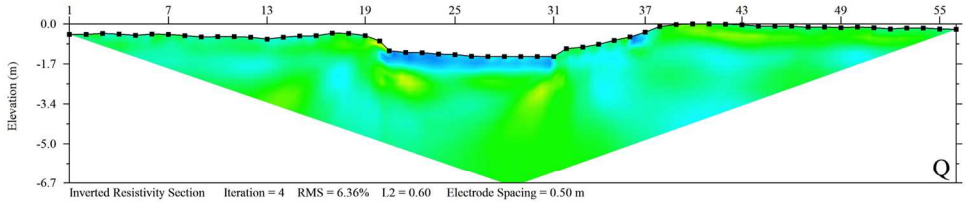

151020_Neap Tomogram Tidal and Scale Information

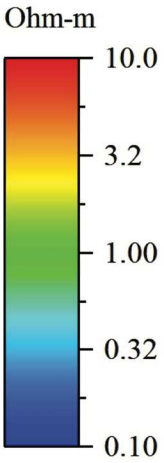

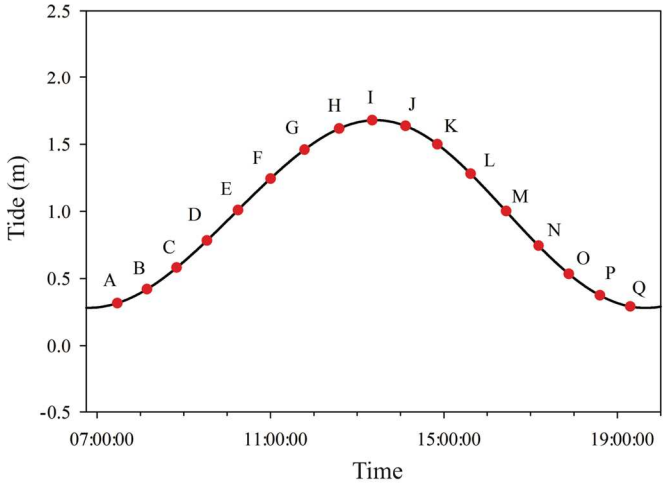

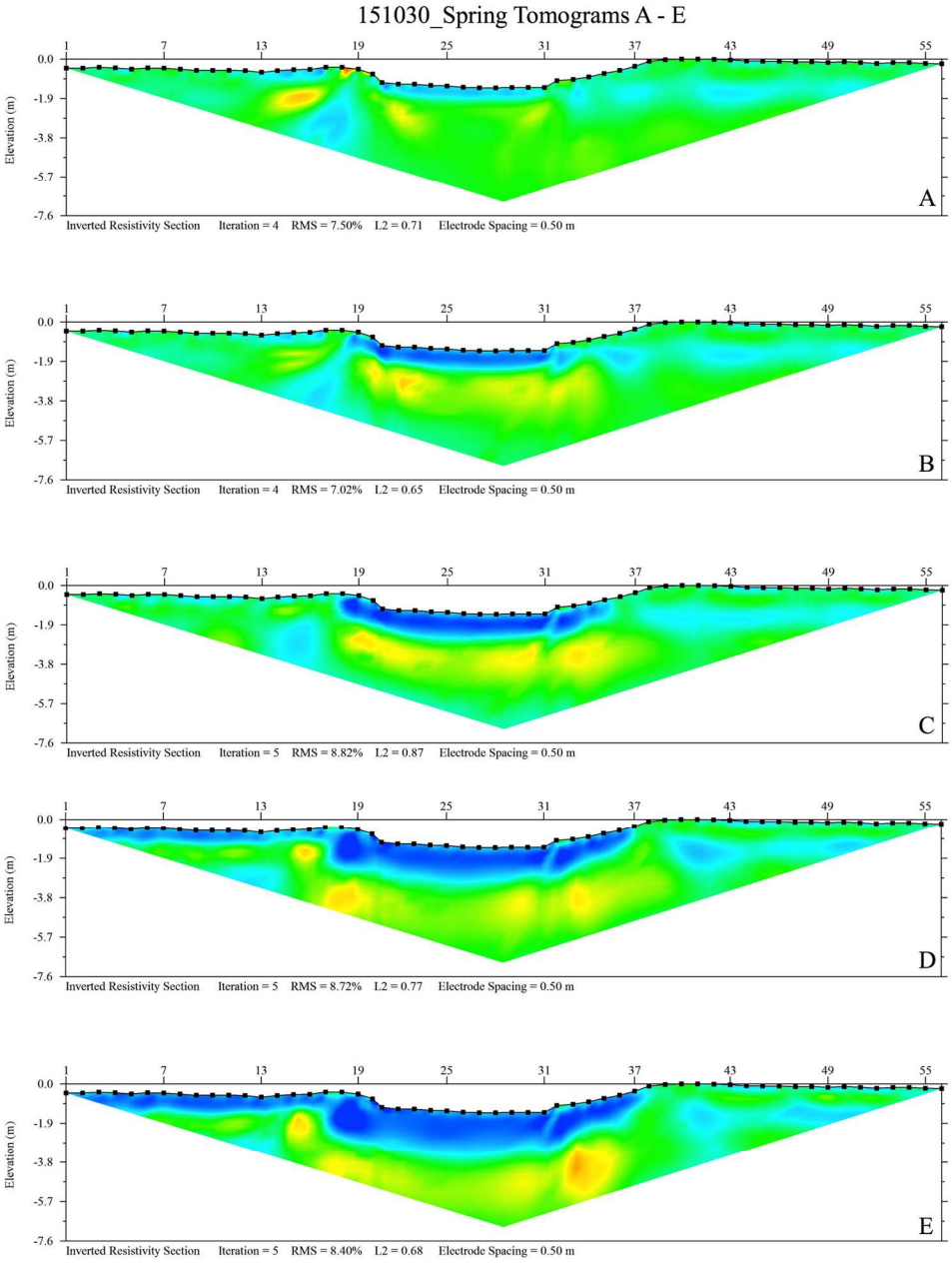
151030_Spring Tomograms A - E
1 7 13 19 25 31 37 43 49 55
0.0 -1.9 -3.8 -5.7 -7.6
Elevation (m)
A
Inverted Resistivity Section Iteration = 4 RMS = 7.50% L2 = 0.71 Electrode Spacing = 0.50 m
B
Inverted Resistivity Section Iteration = 4 RMS = 7.02% L2 = 0.65 Electrode Spacing = 0.50 m
C
Inverted Resistivity Section Iteration = 5 RMS = 8.82% L2 = 0.87 Electrode Spacing = 0.50 m
D
Inverted Resistivity Section Iteration = 5 RMS = 8.72% L2 = 0.77 Electrode Spacing = 0.50 m
E
Inverted Resistivity Section Iteration = 5 RMS = 8.40% L2 = 0.68 Electrode Spacing = 0.50 m

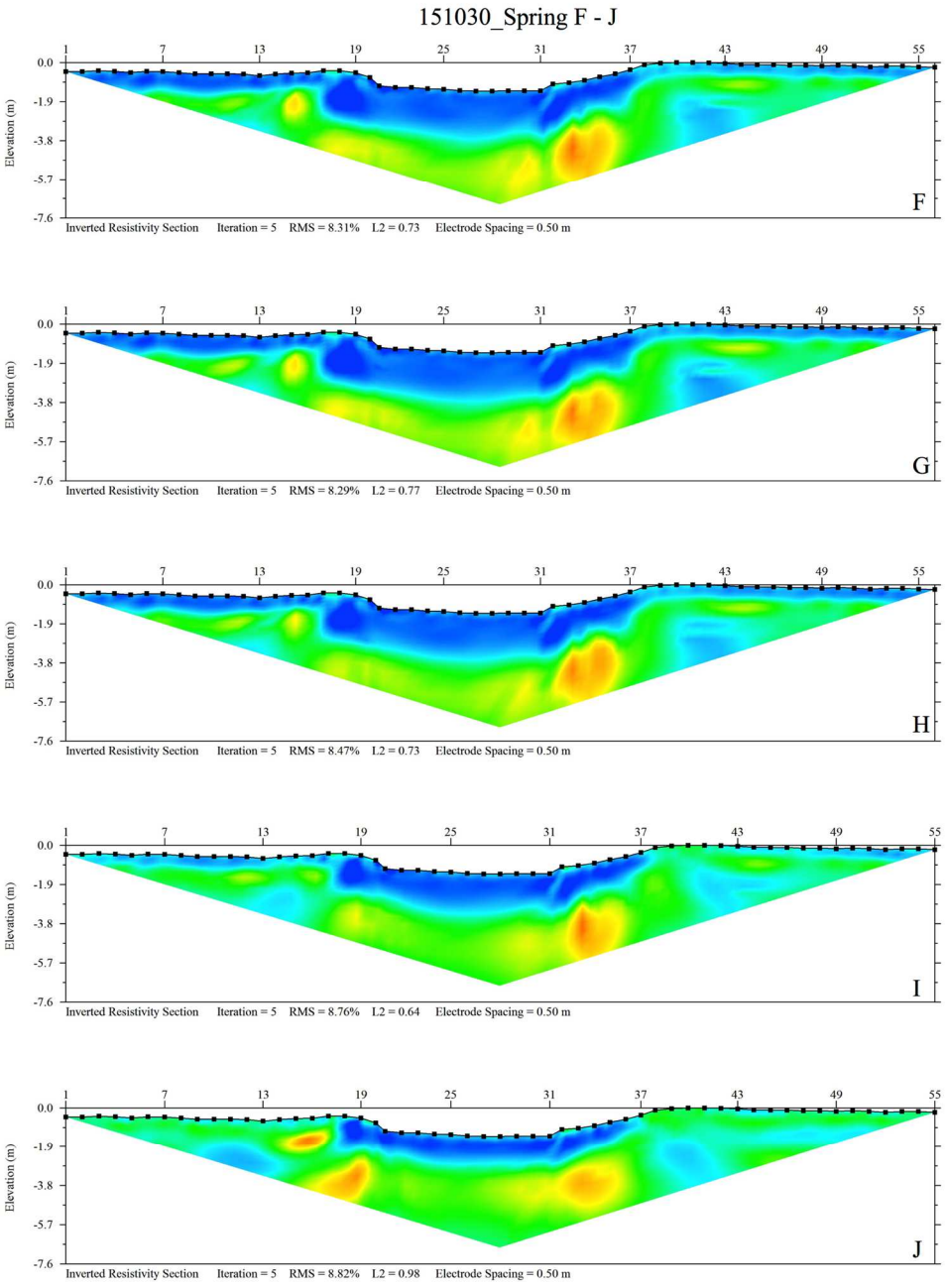
151030_Spring F - J
1 7 13 19 25 31 37 43 49 55
0.0 -1.9 -3.8 -5.7 -7.6
Elevation (m)
F
Inverted Resistivity Section Iteration = 5 RMS = 8.31% L2 = 0.73 Electrode Spacing = 0.50 m
G
Inverted Resistivity Section Iteration = 5 RMS = 8.29% L2 = 0.77 Electrode Spacing = 0.50 m
H
Inverted Resistivity Section Iteration = 5 RMS = 8.47% L2 = 0.73 Electrode Spacing = 0.50 m
I
Inverted Resistivity Section Iteration = 5 RMS = 8.76% L2 = 0.64 Electrode Spacing = 0.50 m
J
Inverted Resistivity Section Iteration = 5 RMS = 8.82% L2 = 0.98 Electrode Spacing = 0.50 m

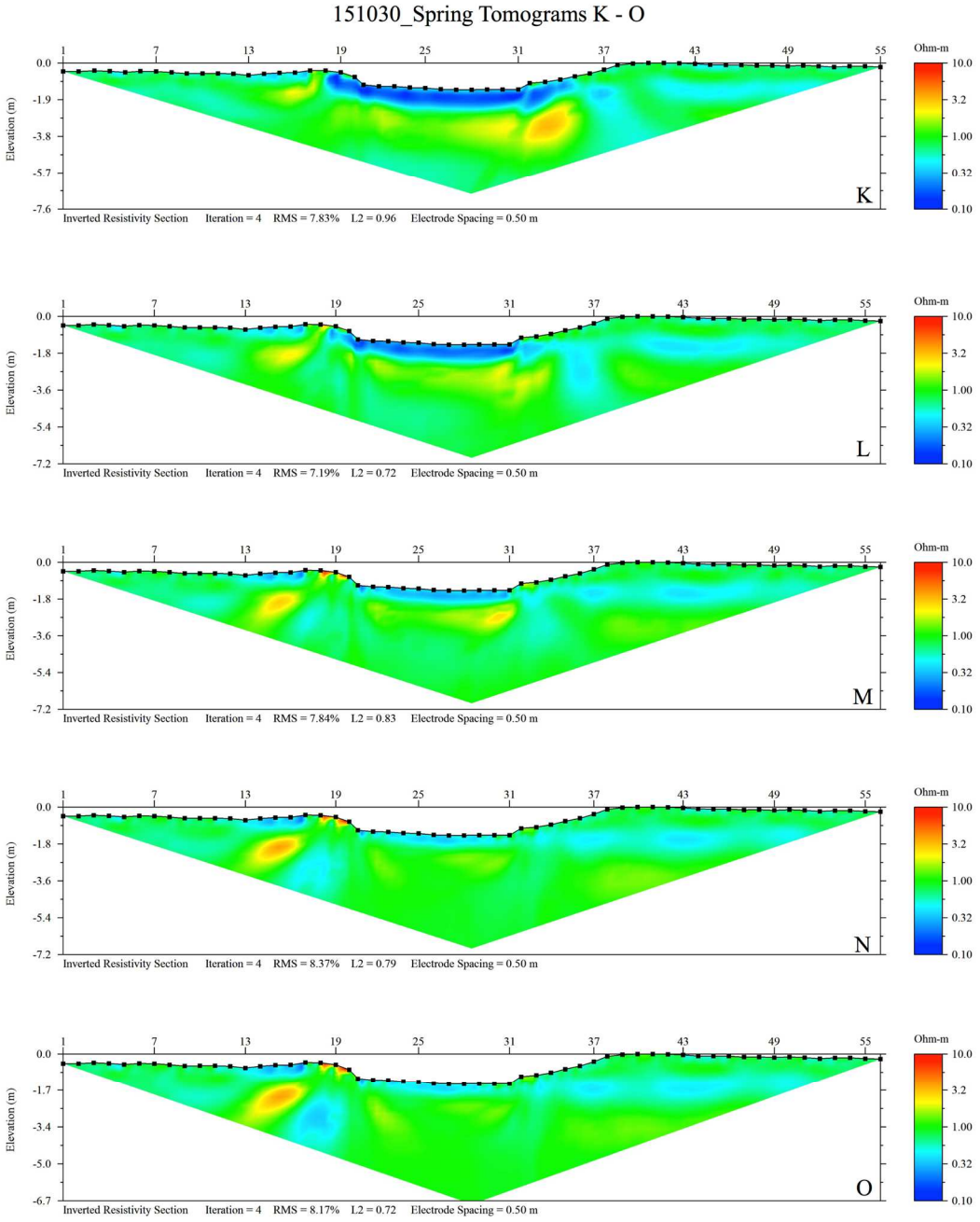
151030_Spring Tomograms K - O
Elevation (m)
Ohm-m
K
Inverted Resistivity Section Iteration = 4 RMS = 7.83% L2 = 0.96 Electrode Spacing = 0.50 m
L
Inverted Resistivity Section Iteration = 4 RMS = 7.19% L2 = 0.72 Electrode Spacing = 0.50 m
M
Inverted Resistivity Section Iteration = 4 RMS = 7.84% L2 = 0.83 Electrode Spacing = 0.50 m
N
Inverted Resistivity Section Iteration = 4 RMS = 8.37% L2 = 0.79 Electrode Spacing = 0.50 m
O
Inverted Resistivity Section Iteration = 4 RMS = 8.17% L2 = 0.72 Electrode Spacing = 0.50 m

151030_Spring Tomogram Tidal and Scale Information

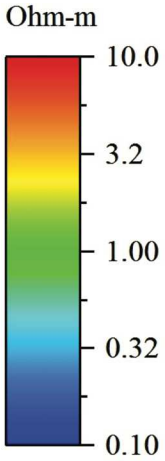

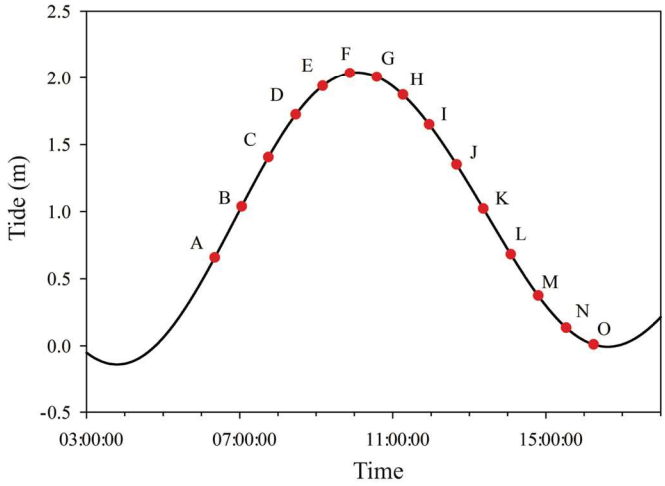

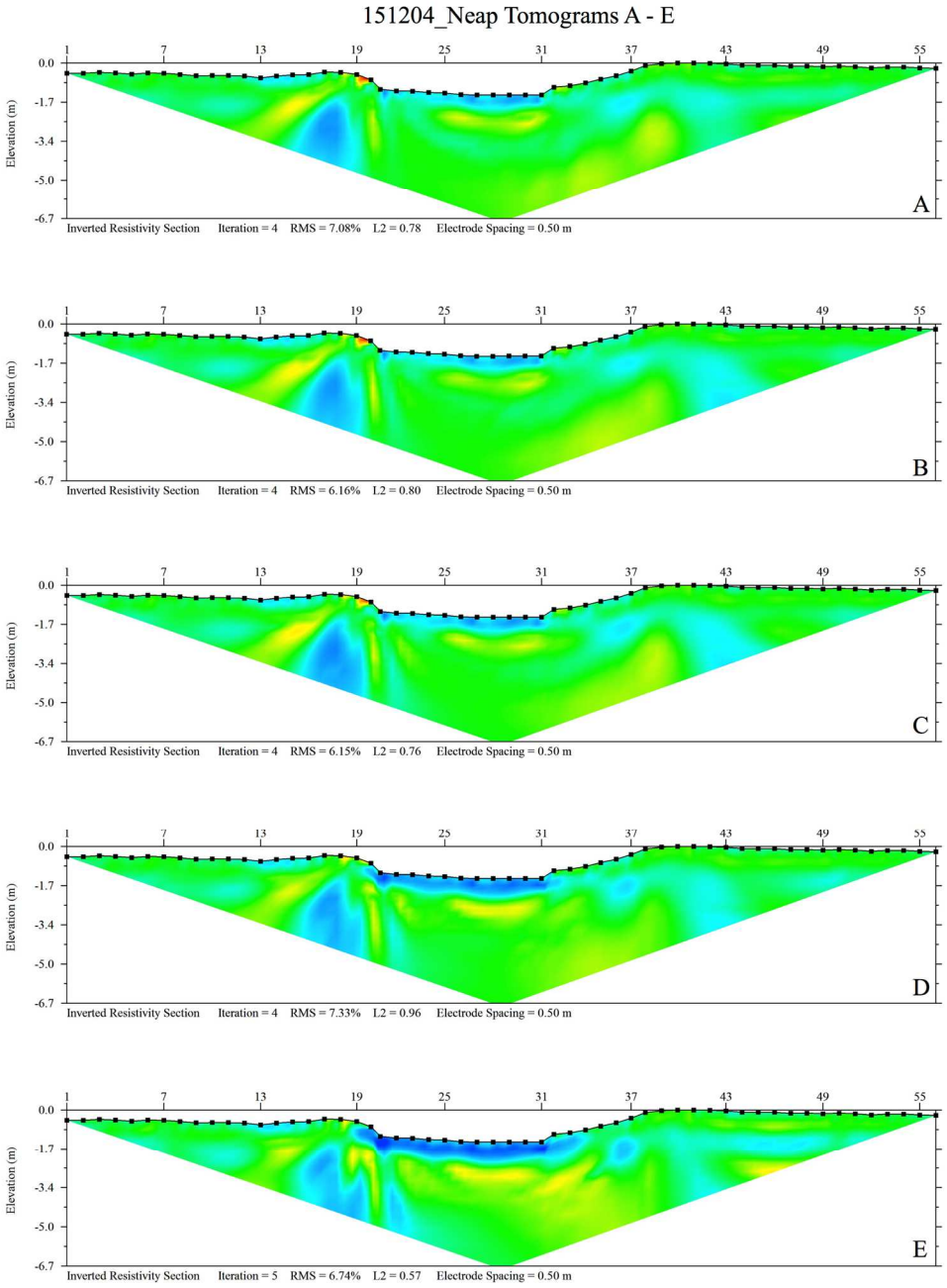
151204_Neap Tomograms A - E
1 7 13 19 25 31 37 43 49 55
0.0 -1.7 -3.4 -5.0 -6.7
Elevation (m)
A
Inverted Resistivity Section Iteration = 4 RMS = 7.08% L2 = 0.78 Electrode Spacing = 0.50 m
B
Inverted Resistivity Section Iteration = 4 RMS = 6.16% L2 = 0.80 Electrode Spacing = 0.50 m
C
Inverted Resistivity Section Iteration = 4 RMS = 6.15% L2 = 0.76 Electrode Spacing = 0.50 m
D
Inverted Resistivity Section Iteration = 4 RMS = 7.33% L2 = 0.96 Electrode Spacing = 0.50 m
E
Inverted Resistivity Section Iteration = 5 RMS = 6.74% L2 = 0.57 Electrode Spacing = 0.50 m

151204_Neap Tomograms F - J

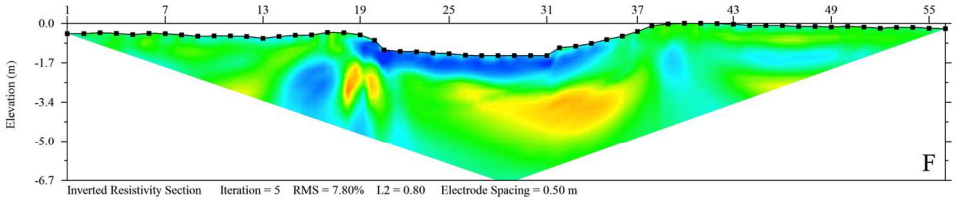

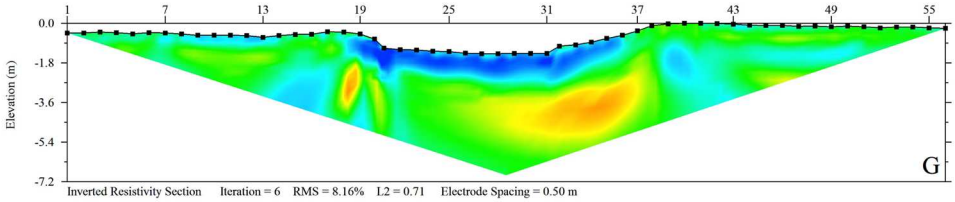

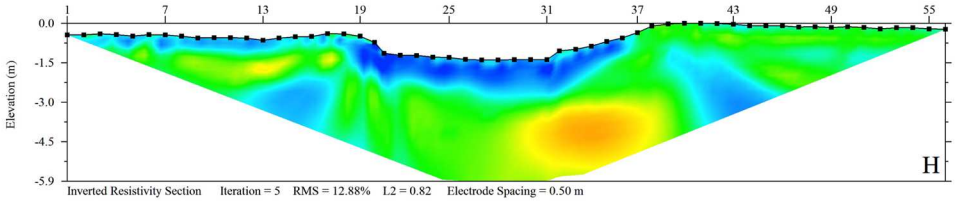

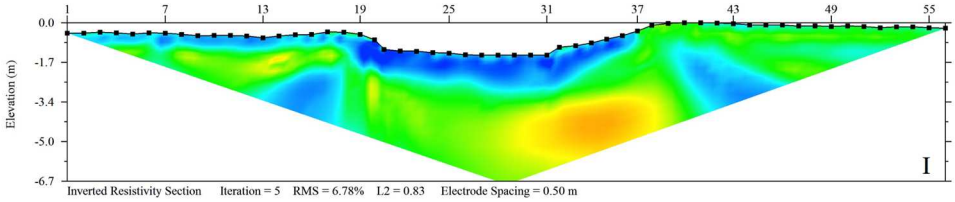

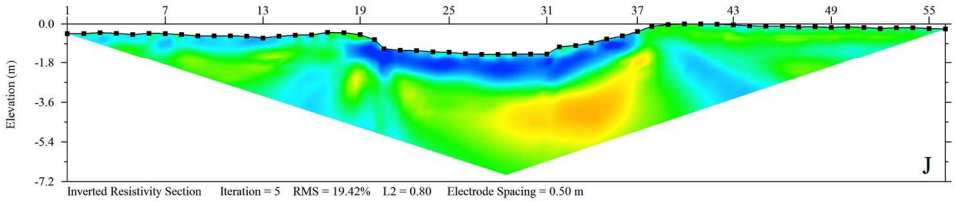

151204_Neap Tomograms K - O

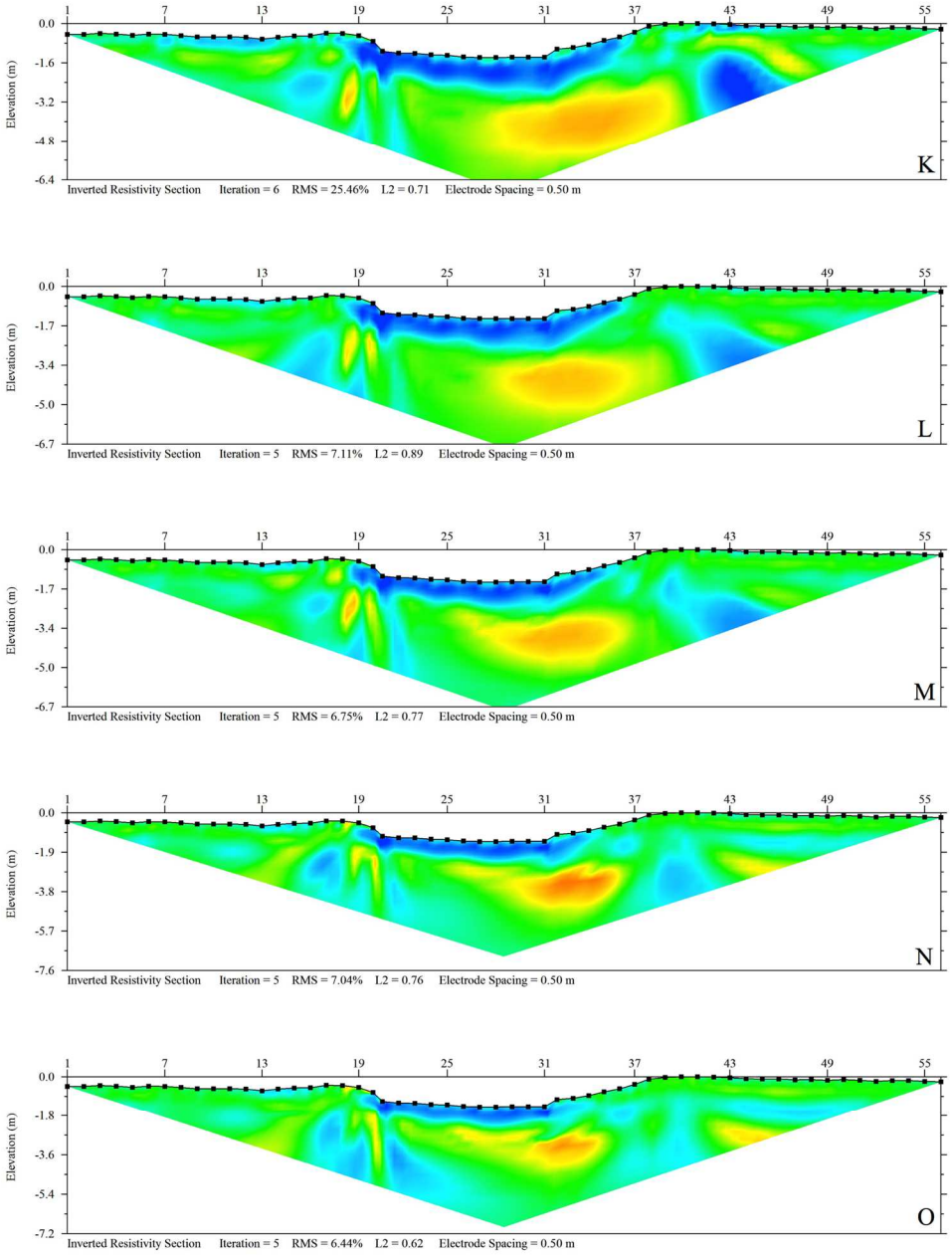

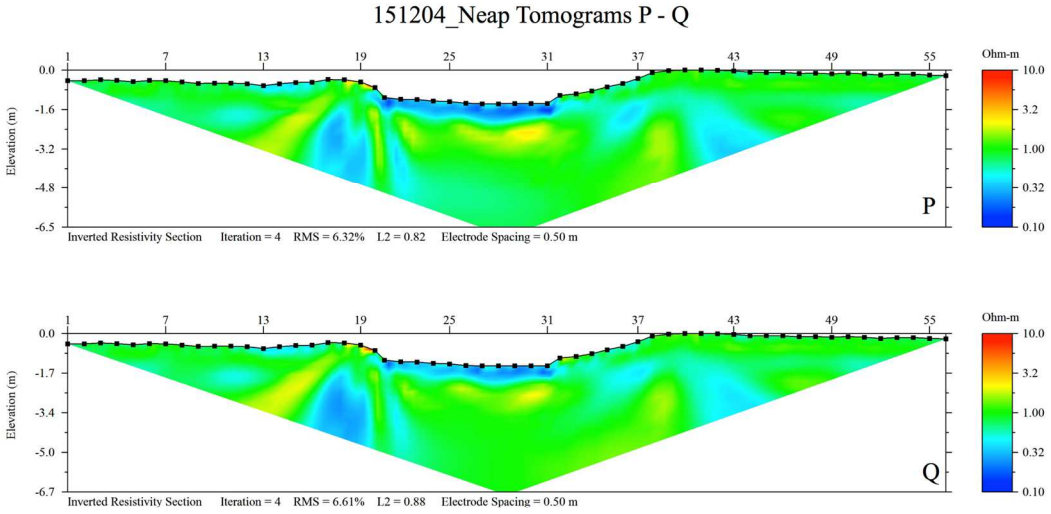
151204_Neap Tomograms P - Q
1
7
13
19
25
31
37
43
49
55
0.0
-1.6
-3.2
-4.8
-6.5
Elevation (m)
Ohm-m
10.0
3.2
1.00
0.32
0.10
P
Inverted Resistivity Section Iteration = 4 RMS = 6.32% L2 = 0.82 Electrode Spacing = 0.50 m
0.0
-1.7
-3.4
-5.0
-6.7
Q
Inverted Resistivity Section Iteration = 4 RMS = 6.61% L2 = 0.88 Electrode Spacing = 0.50 m

151204_Neap Tomogram Tidal and Scale Information

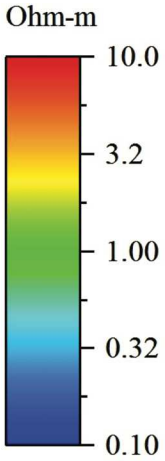

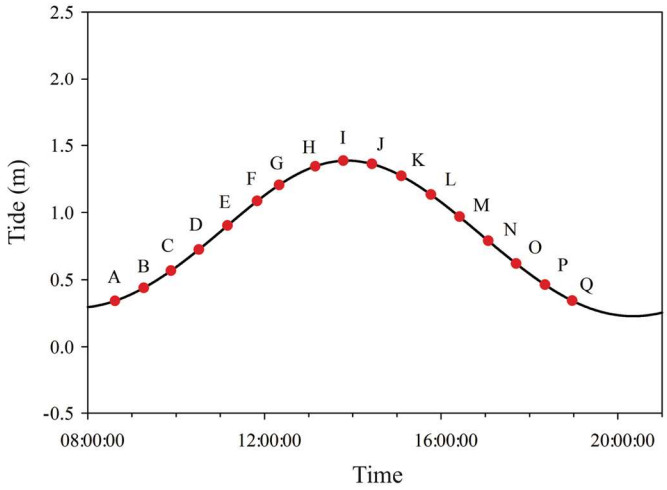

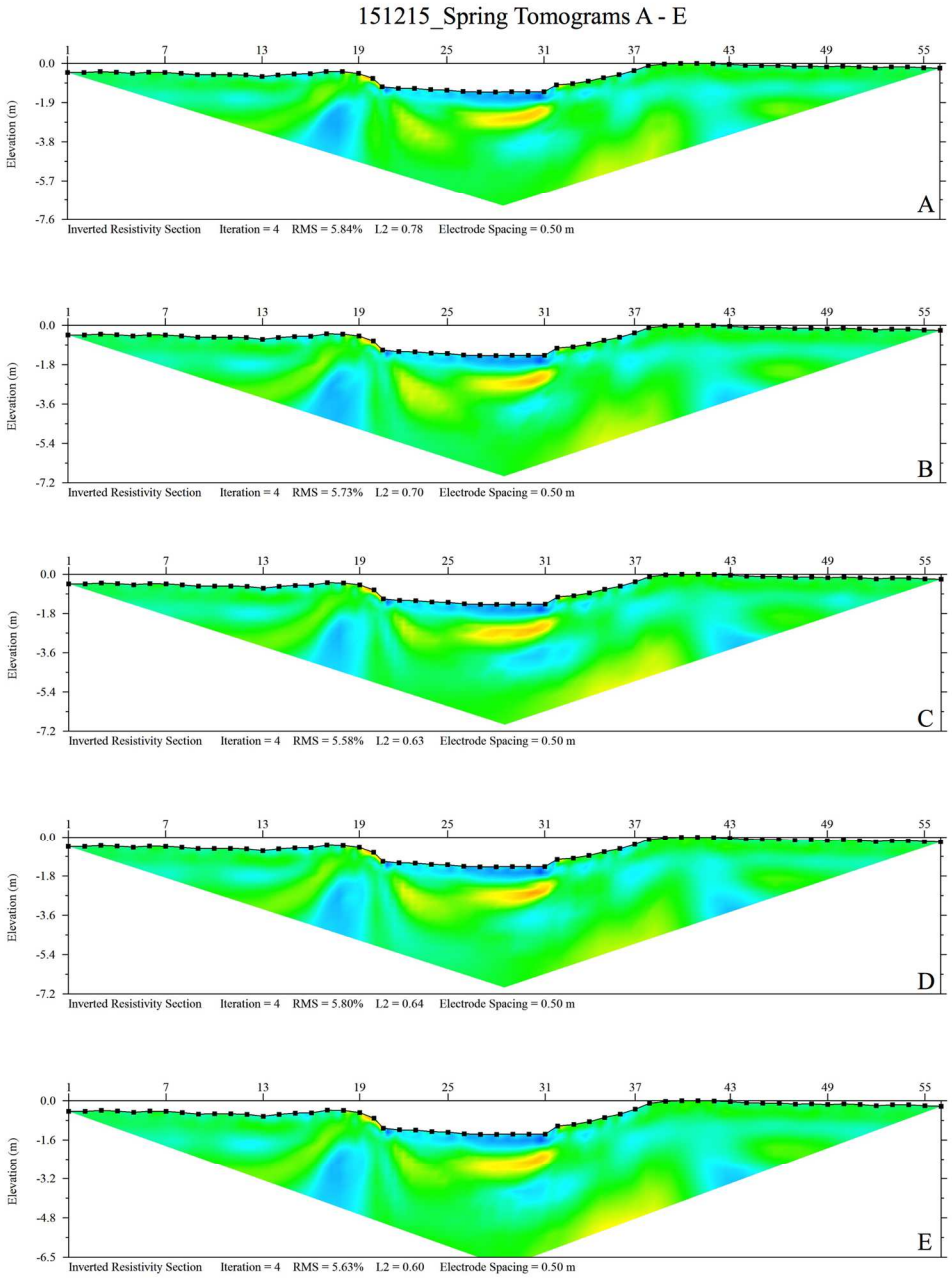
151215_Spring Tomograms A - E
1 7 13 19 25 31 37 43 49 55
0.0 -1.9 -3.8 -5.7 -7.6
Elevation (m)
A
Inverted Resistivity Section Iteration = 4 RMS = 5.84% L2 = 0.78 Electrode Spacing = 0.50 m
1 7 13 19 25 31 37 43 49 55
0.0 -1.8 -3.6 -5.4 -7.2
Elevation (m)
B
Inverted Resistivity Section Iteration = 4 RMS = 5.73% L2 = 0.70 Electrode Spacing = 0.50 m
1 7 13 19 25 31 37 43 49 55
0.0 -1.8 -3.6 -5.4 -7.2
Elevation (m)
C
Inverted Resistivity Section Iteration = 4 RMS = 5.58% L2 = 0.63 Electrode Spacing = 0.50 m
1 7 13 19 25 31 37 43 49 55
0.0 -1.8 -3.6 -5.4 -7.2
Elevation (m)
D
Inverted Resistivity Section Iteration = 4 RMS = 5.80% L2 = 0.64 Electrode Spacing = 0.50 m
1 7 13 19 25 31 37 43 49 55
0.0 -1.6 -3.2 -4.8 -6.5
Elevation (m)
E
Inverted Resistivity Section Iteration = 4 RMS = 5.63% L2 = 0.60 Electrode Spacing = 0.50 m

151215_Spring Tomograms F - J

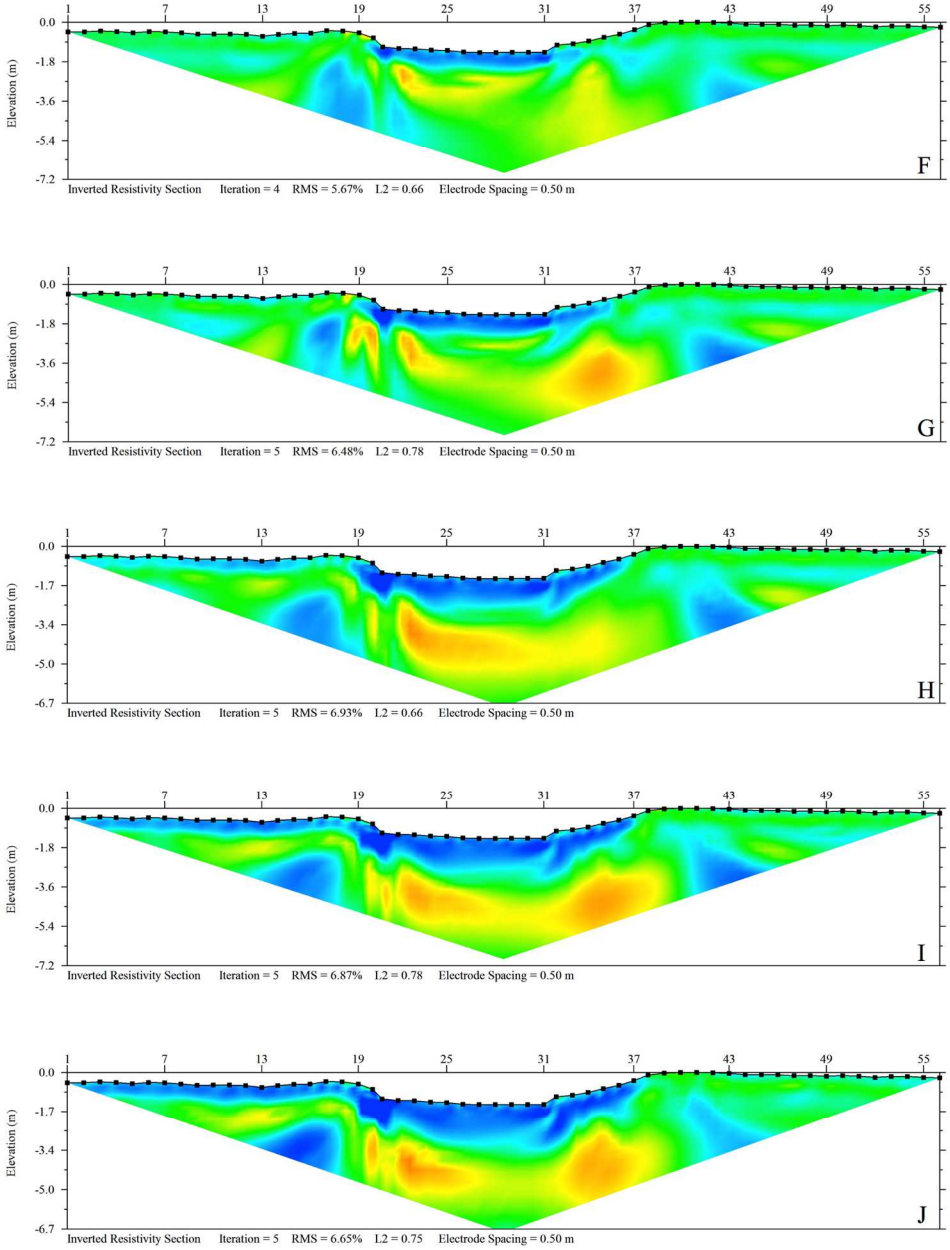

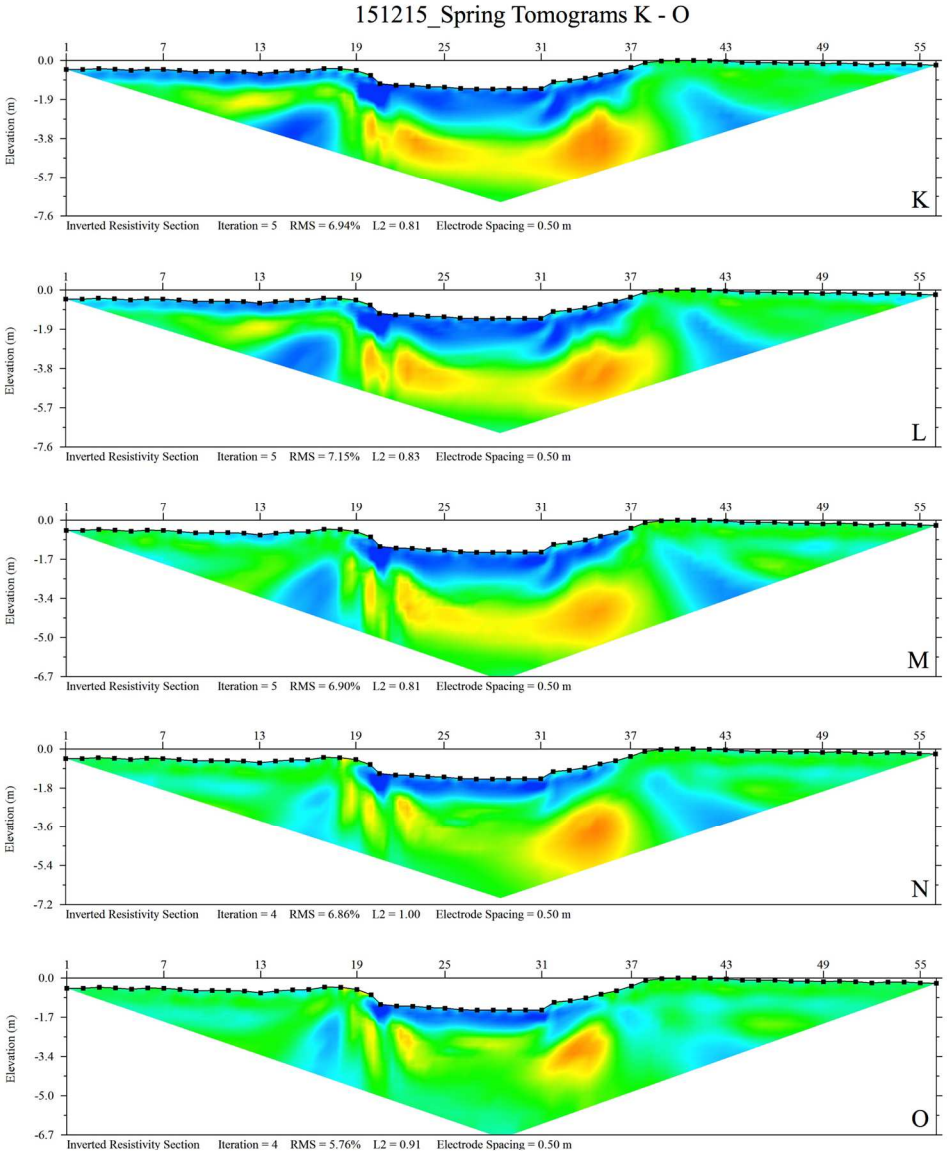
151215_Spring Tomograms K - O
1 7 13 19 25 31 37 43 49 55
0.0 -1.9 -3.8 -5.7 -7.6
Elevation (m)
K
Inverted Resistivity Section Iteration = 5 RMS = 6.94% L2 = 0.81 Electrode Spacing = 0.50 m
L
Inverted Resistivity Section Iteration = 5 RMS = 7.15% L2 = 0.83 Electrode Spacing = 0.50 m
0.0 -1.7 -3.4 -5.0 -6.7
M
Inverted Resistivity Section Iteration = 5 RMS = 6.90% L2 = 0.81 Electrode Spacing = 0.50 m
0.0 -1.8 -3.6 -5.4 -7.2
N
Inverted Resistivity Section Iteration = 4 RMS = 6.86% L2 = 1.00 Electrode Spacing = 0.50 m
0.0 -1.7 -3.4 -5.0 -6.7
O
Inverted Resistivity Section Iteration = 4 RMS = 5.76% L2 = 0.91 Electrode Spacing = 0.50 m

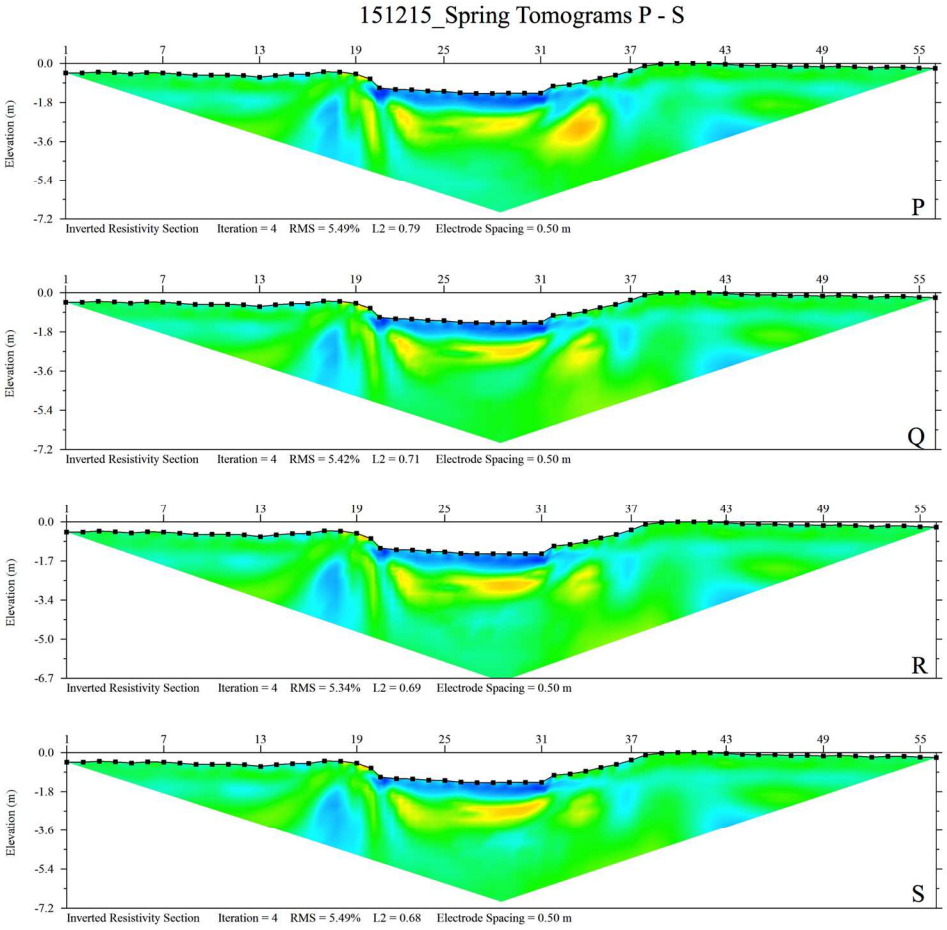
151215_Spring Tomograms P - S
1 7 13 19 25 31 37 43 49 55
0.0 -1.8 -3.6 -5.4 -7.2
Elevation (m)
Inverted Resistivity Section Iteration = 4 RMS = 5.49% L2 = 0.79 Electrode Spacing = 0.50 m
P
Inverted Resistivity Section Iteration = 4 RMS = 5.42% L2 = 0.71 Electrode Spacing = 0.50 m
Q
0.0 -1.7 -3.4 -5.0 -6.7
Inverted Resistivity Section Iteration = 4 RMS = 5.34% L2 = 0.69 Electrode Spacing = 0.50 m
R
Inverted Resistivity Section Iteration = 4 RMS = 5.49% L2 = 0.68 Electrode Spacing = 0.50 m
S

151215_Spring Tomogram Tidal and Scale Information

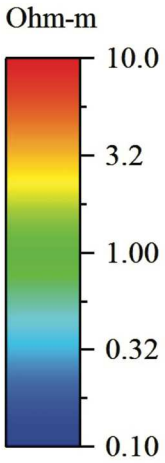

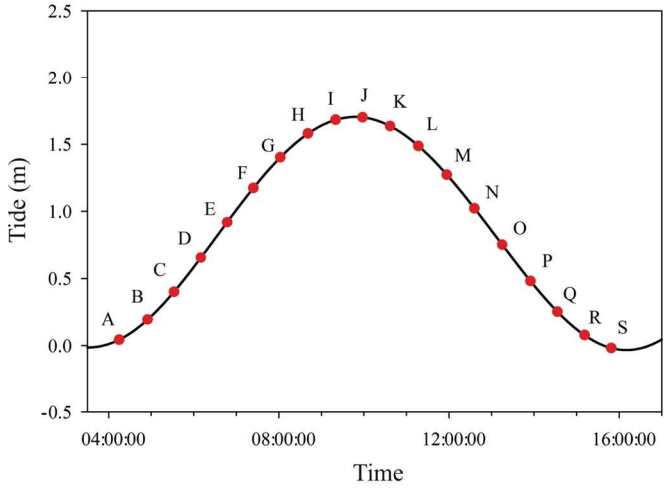

160125_Spring Tomograms A - E

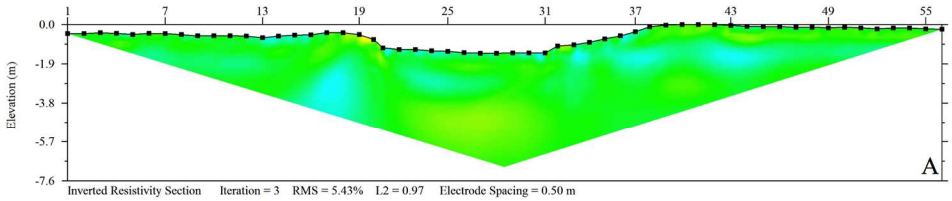

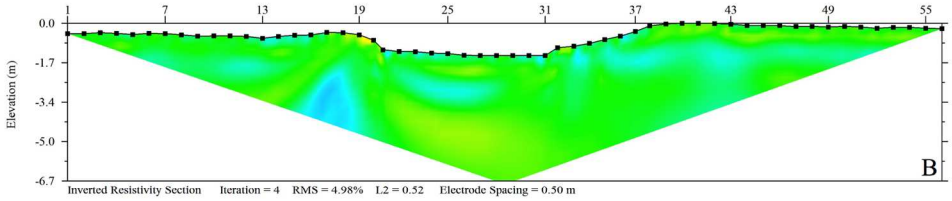

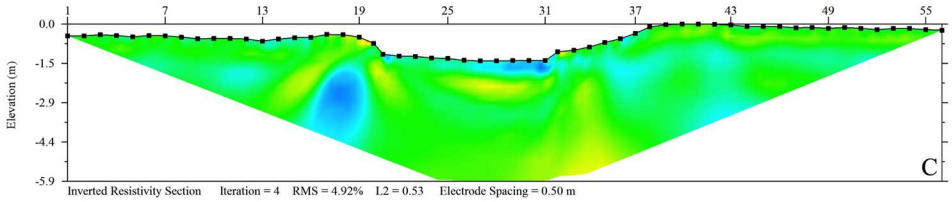

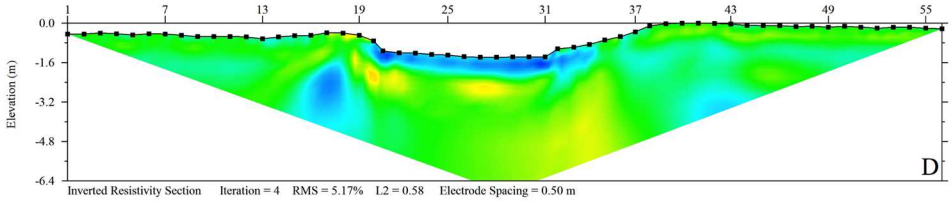

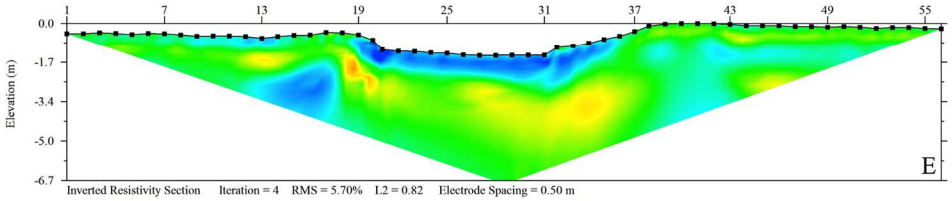

160125_Spring Tomograms F - J

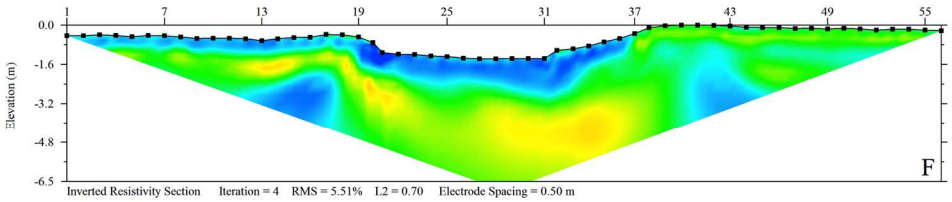

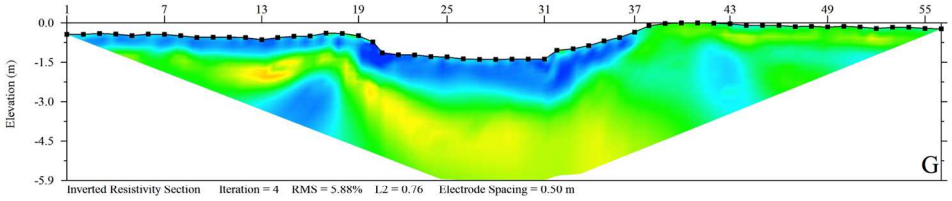

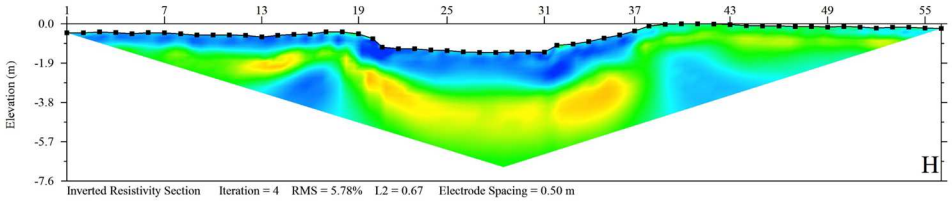

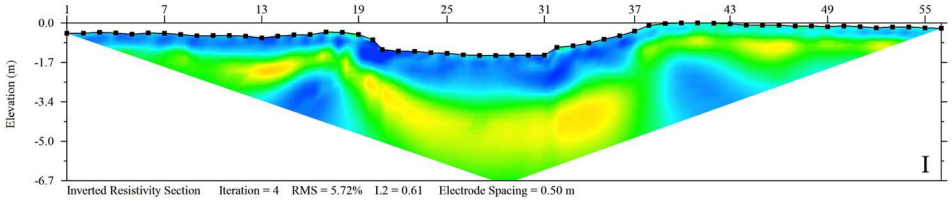

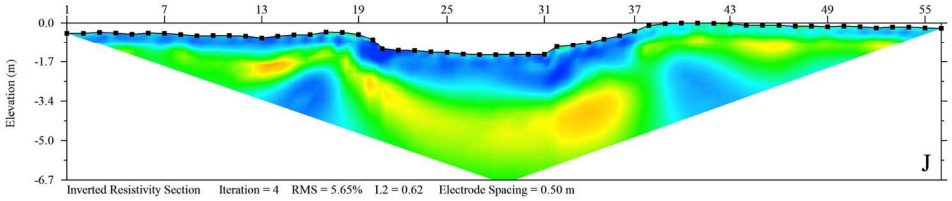

160125_Spring Tomograms K - O

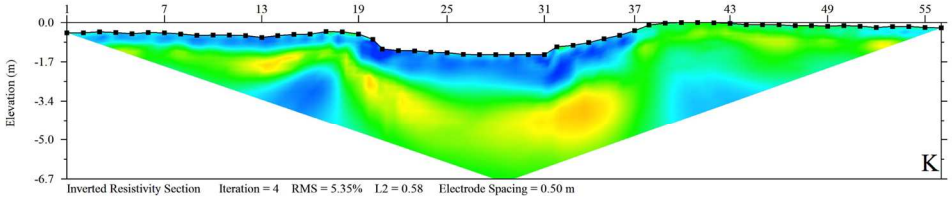

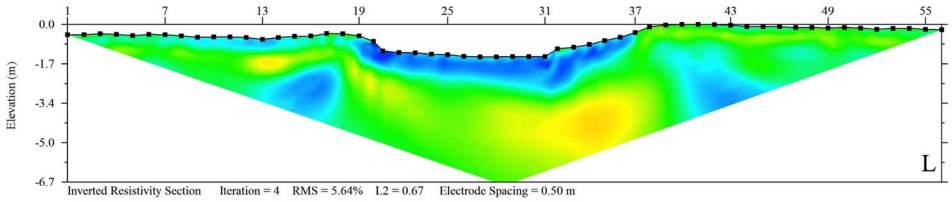

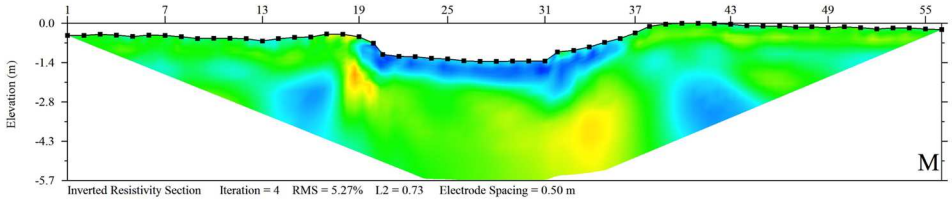

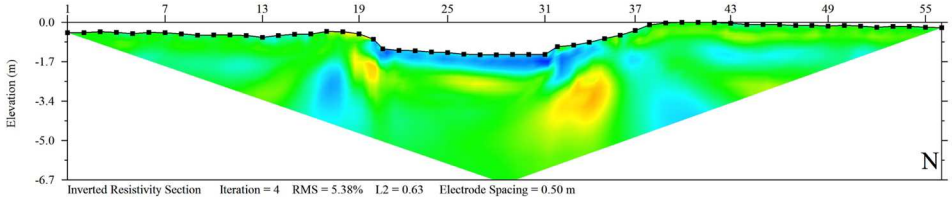

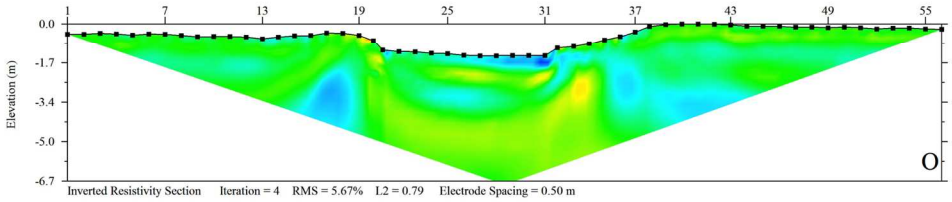

160125_Spring Tomograms P - R

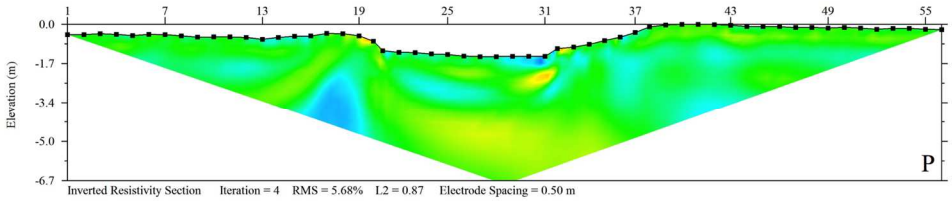

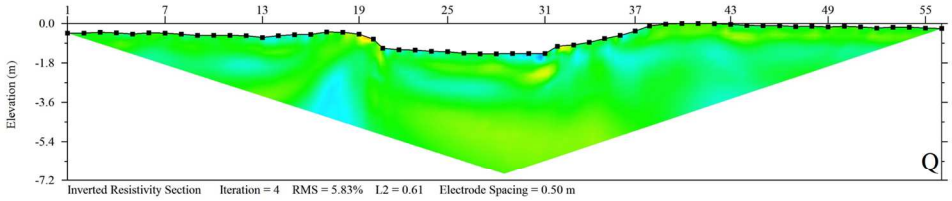

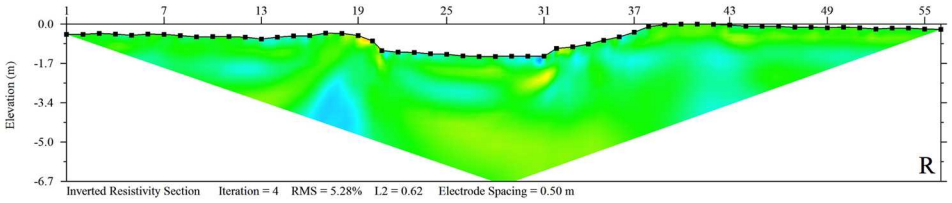

160125_Spring Tomogram Tidal and Scale Information

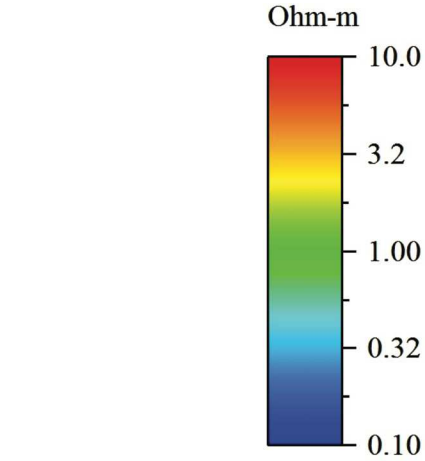

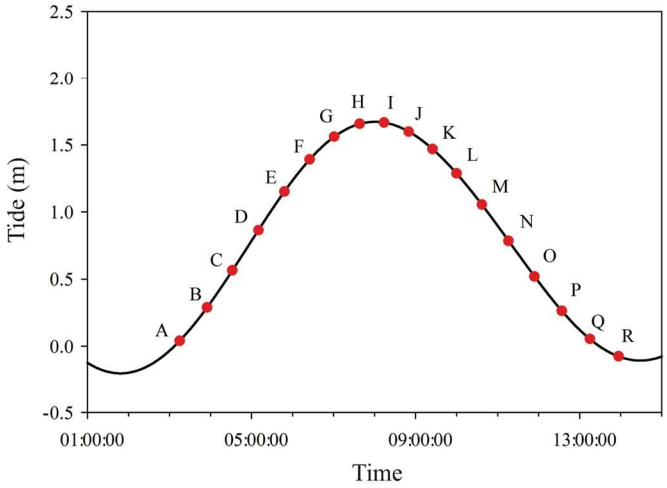

160131_Neap Tomograms A - E

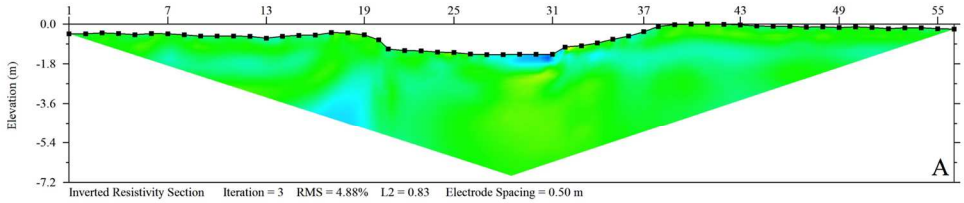

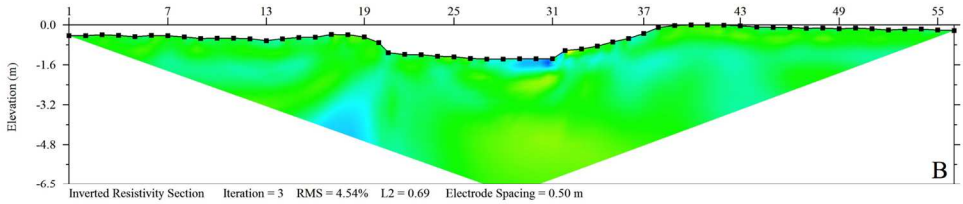

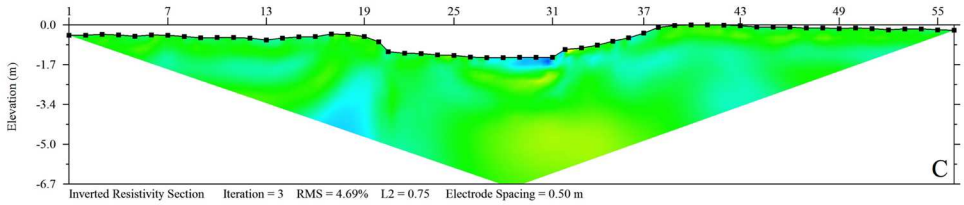

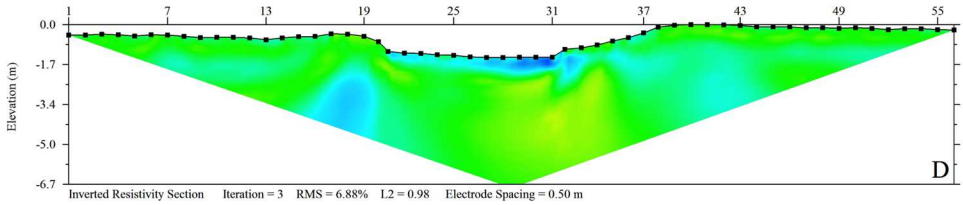

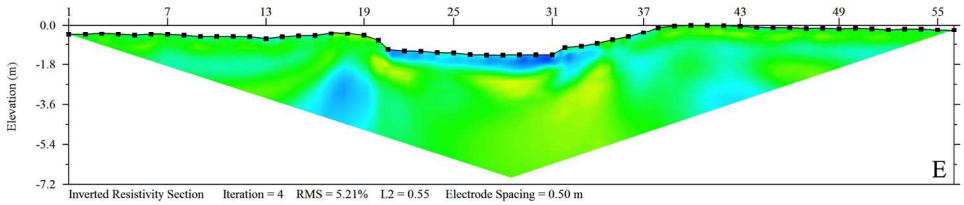

160131_Neap Tomograms F - J

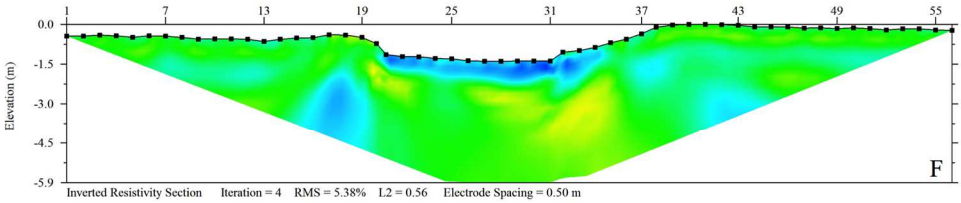

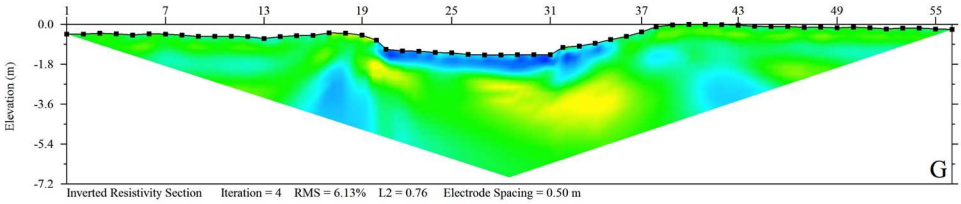

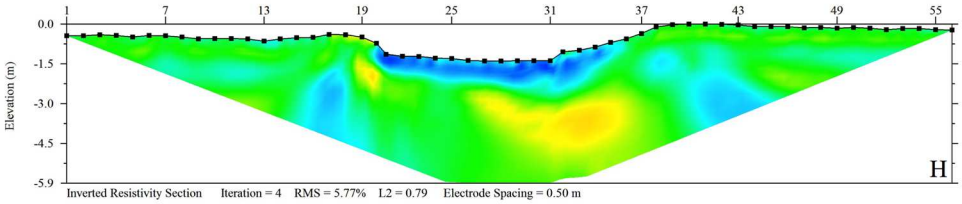

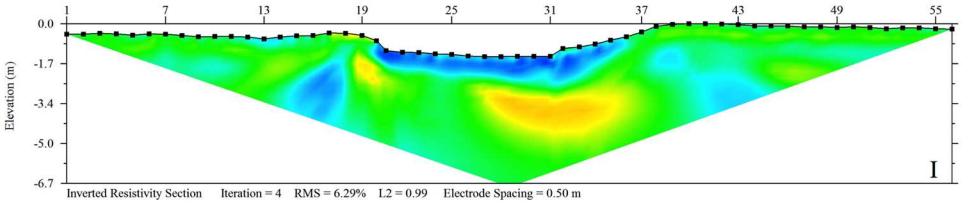

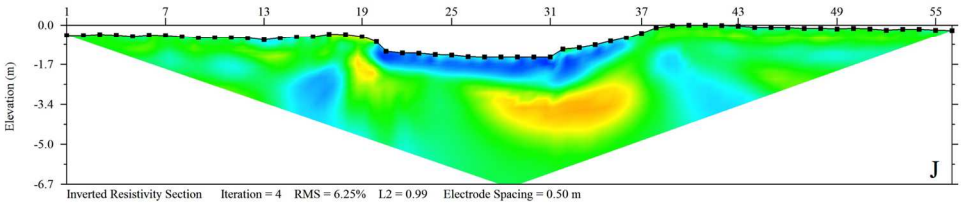

160131_Neap Tomograms K - O

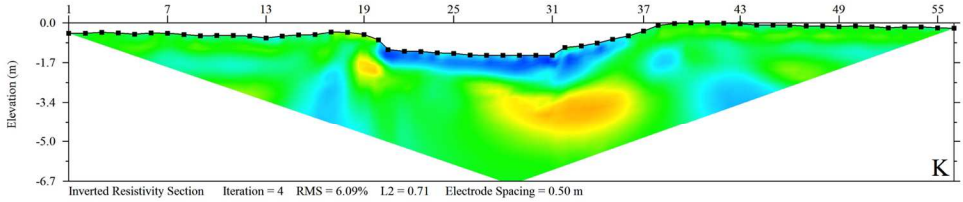

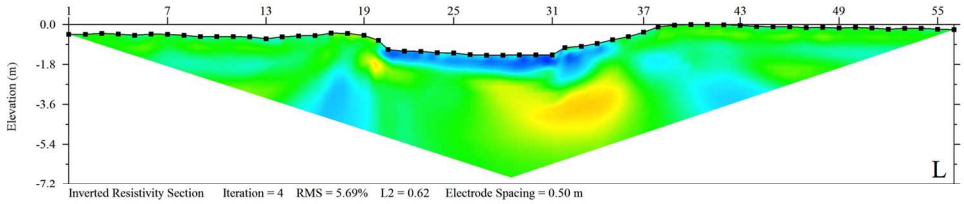

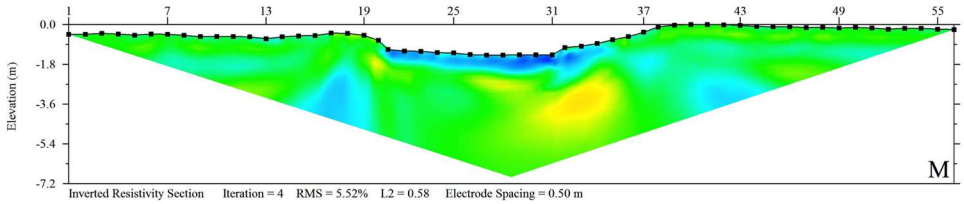

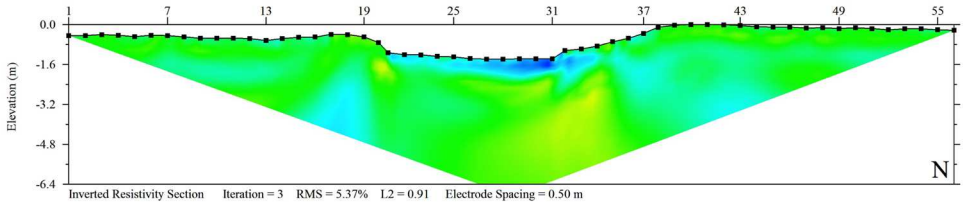

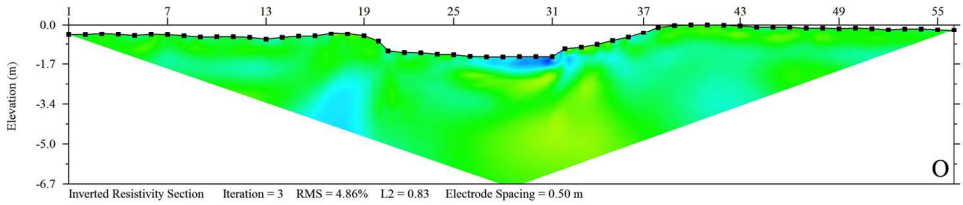

160131_Neap Tomograms P - Q

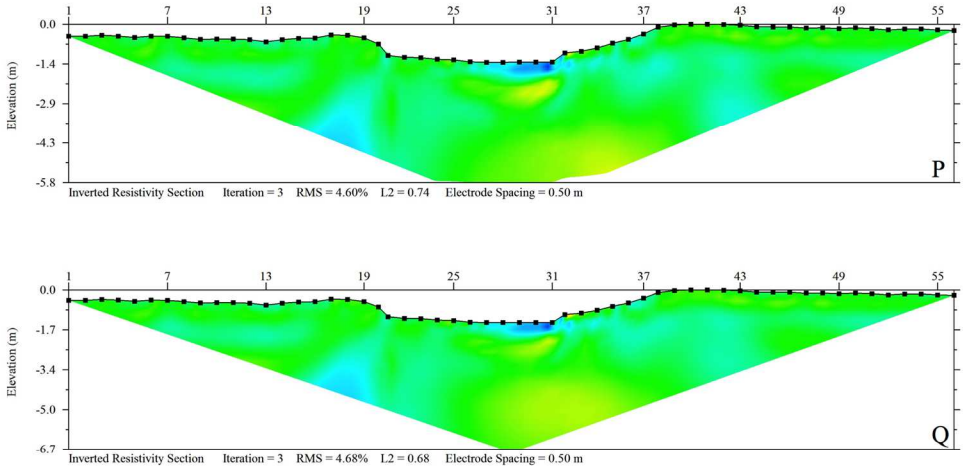

160131_Neap Tomogram Tidal and Scale Information

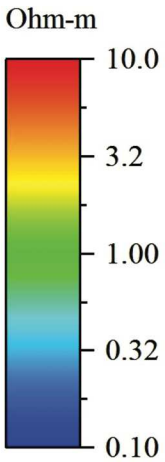

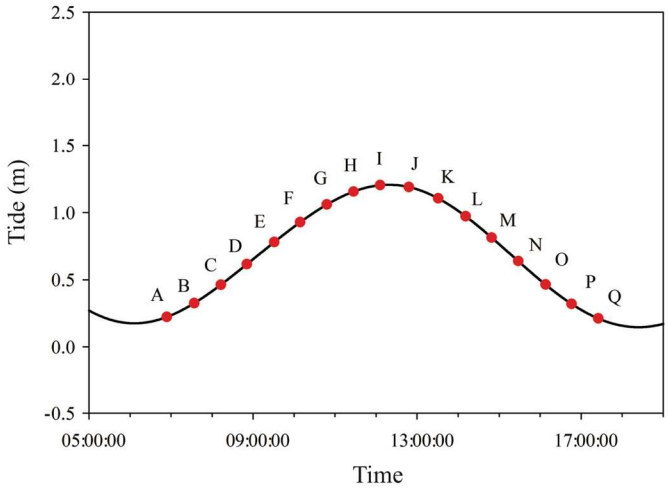

Appendix B

Vibracore Logs

The following appendix is a copy of the five-sediment core logs that were analyzed for the shallow subsurface stratigraphy. The cores were collected after the electrical resistivity surveys. Vibracore 1 was placed on the hammock upland marsh platform; Vibracore 2 was placed on the cut bank side of the creek channel in a muddy sandy upper-layer containing oyster shells. Vibracore 3 was placed in the middle of the creek channel. Vibracore 4 was placed on the point bar side of the channel in a fine sand upper layer. Vibracore 5 was placed on the levee on the other side of the creek, in muddy sandy sediment. This created a high-resolution data set displaying what the underlying stratigraphy looked like, concentrating on the area that is affected by hyporheic zone processes.

CORE DESCRIPTION SHEET

Core ID: 1A | Core Length: 3.65m | Describer: Matt Kestner | Comments:

Location: Waties Island | Core Depth: | Date: 2/24/16

mud | fine sand | med sand | coarse sand | pebbles | roots | wood frag | shells | burrows | bedding | contact

start at: 0 m

avg. grain size (gravel, v. coarse, coarse, medium, fine, v. fine, silt, clay):
mineralogy: texture (org.-rich: peaty; shelly; sandy, muddy sand, sandy mud, mud):
sorting (well, medium, poor):
structures: bedding (type, size, configuration, location), bioturbation (type, size, abundance, location)
components: shell, organic material (type, condition, abundance, size)

page: of

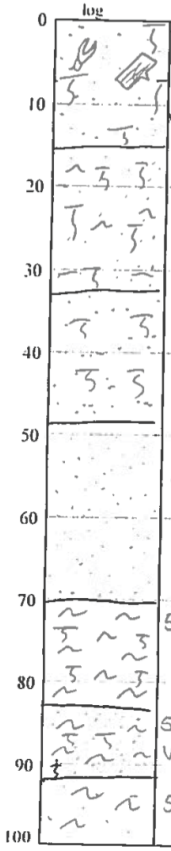

log	color		other/comments
	2.5Y 3/2 very dark grayish brown	0.0 - 0.15m v. fine to fine sand highly organic w/ roots woody fragments and fiddler crab claw. smells bad.	
	2.5Y 3/3 dark olive brown	0.15 - 0.32m muddy v.fine to fine sand visable roots brown color due to redox reactions.	
	2.5Y 3/3 ↓ 5Y 4/1	0.32 - 0.49 2. Gradual transition w/ plenty roots present from 2.5Y 3/3 to 5Y 4/1 dark gray. fine - v. fine sand.	
	5Y 5/1 gray	0.49-0.70 Fine sand w/ quartz and dark minerals massive Sharp bottom contact.	
	5Y 2.5/1 black	0.70 - 0.82 silty muddy black mud some sandy. spartina remnants? organic rich	
	5Y 3/1 V. dark gray	0.82 - 0.91 Sandy mud fine sand contains some plant remnants.	
	5Y 2.5/1 black	0.91 - 1.50	

CORE DESCRIPTION SHEET

Core ID: 1A
Location: Waties Island
Core Length: 3.65 m
Core Depth:
Describer: Matt Kestner
Date: 2/24/16
Comments:

mud – fine sand · med sand ⁘ coarse sand ⁘ pebbles ⁘ roots ⊤ wood frag ⌂ shells ⋎ ⋏ burrows ∿ bedding ≈ contact ∿

start at: 0 m

avg. grain size (gravel, v. coarse, coarse, medium, fine, v. fine, silt, clay):
mineralogy: texture (org.-rich; peaty; shelly; sandy, muddy sand, sandy mud, mud):
sorting (well, medium, poor):
structures: bedding (type, size, configuration, location), bioturbation (type, size, abundance, location)
components: shell, organic material (type, condition, abundance, size)

page: of

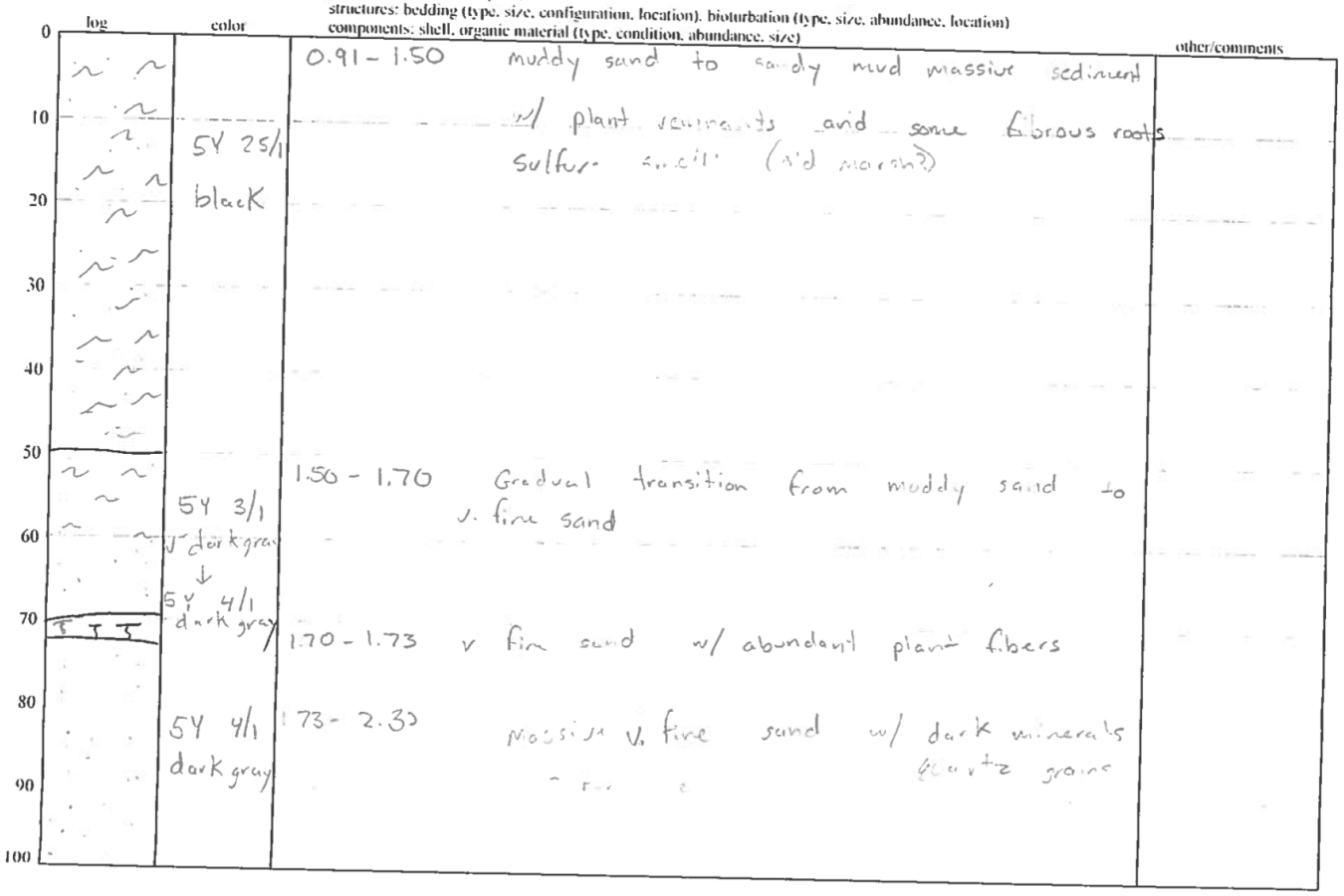

CORE DESCRIPTION SHEET

Core ID: 1B Core Length: 3.65m Describer: MaH Kestner Comments:

Location: Wallis Island Core Depth: Date: 2/24/16

mud fine sand med sand coarse sand pebbles roots wood frag shells burrows bedding contact

start at: 3 m

avg. grain size (gravel, v. coarse, coarse, medium, fine, v. fine, silt, clay):
mineralogy: texture (org.-rich; peaty; shelly; sandy, muddy sand, sandy mud, mud):
sorting (well, medium, poor):
structures: bedding (type, size, configuration, location), bioturbation (type, size, abundance, location)
components: shell, organic material (type, condition, abundance, size)

page: __ of __

log	color		other/comments
0		2.75 - 3.63 Massive fine sand w/ crushed shells (whole cerithium shell) quartz and dark minerals.	
10	5Y 5/1 gray	3.10 - 3.12 dark gray muddy shelly layer	
20			
30		3.31-3.32 dark gray [illegible] layer shelly	
40		3.40 dark brown woody plant [illegible] layer	
		3.45 - 3.47 dark gray/black muddy layer	
50		3.53 - 3.57 muddy orbital / clast	
60		3.63 - dark brown [illegible] clay.	
	5Y 6/1 gray	3.63 - 3.65 Medium sand clean quartz and dark minerals	
70			
80			
90			
100			

CORE DESCRIPTION SHEET

Core ID: 2A Core Length: 3.65 m Describer: Matt Kestner Comments:

Location: Waties Island Core Depth: Date: 2/23/16

mud fine sand med sand coarse sand pebbles roots wood frag shells burrows bedding contact

start at: 0 m

avg. grain size (gravel, v. coarse, coarse, medium, fine, v. fine, silt, clay);
mineralogy: texture (org.-rich; peaty; shelly; sandy, muddy sand, sandy mud, mud);
sorting (well, medium, poor);
structures: bedding (type, size, configuration, location), bioturbation (type, size, abundance, location)
components: shell, organic material (type, condition, abundance, size)

page: of

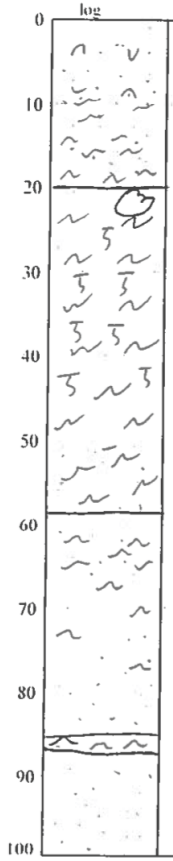

color		other/comments
5Y 3/1 very dark grey	0.0 – 0.20m Gradational contact fine sand, oxidation, some shells grading into a muddy fine very fine sand	
5Y 2.5/1 Black	0.20 – 0.58 Very fine sand mud to mud. root remnants (spartina?) Large ~3cm Oyster shell? Sulfur smell Gradational contact at bottom	
5Y 3/1 very dark grey ↓	0.58 – 0.84 grading from muddy very fine sand w/visable quartz and dark minerals to a very fine to fine sand w/ minimal mud.	
5Y 4/1 dark gray	0.84 – 0.85 muddy v. fine to fine sand	
5Y 2.5/1 black	0.85 – 1.30	

CORE DESCRIPTION SHEET

Core ID: 2A Core Length: 3.65 m Describer: Matt Kestner Comments:

Location: Waties Island Core Depth: Date: 2/23/16

mud fine sand med sand coarse sand pebbles roots wood frag shells burrows bedding contact

start at: 1 m

avg. grain size (gravel, v. coarse, coarse, medium, fine, v. fine, silt, clay):
mineralogy: texture (org.-rich; peaty; shelly; sandy, muddy sand, sandy mud, mud):
sorting (well, medium, poor):
structures: bedding (type, size, configuration, location), bioturbation (type, size, abundance, location)
components: shell, organic material (type, condition, abundance, size)

page: __ of __

log	color		other/comments
0			
	5Y 4/1 dark gray	0.85 - 1.30 Massive v fine to fine sand w/ visable quartz and dark minerals.	
10			
20			
30		1.30 - 1.79 More fine grained well sorted sand w/ visable quartz and dark grains. Massive has some crushed shells.	
40	5Y 5/1 gray		
50			
60			
70			
80	5Y 2.5/1 black	Sharp contact 1.79 - 1.81 muddy sand w/ large ~ 1cm woody fragments	
		1.81 - 2.30	
90	5Y 4/1 dark gray	1.85 woody piece Fine sand w/ visable quartz grains and dark woody pieces and crushed shell fragments	
100			

CORE DESCRIPTION SHEET

Core ID: 2B | Core Length: 3.65m | Describer: Matt Kestner | Comments:

Location: Waties Island | Core Depth: | Date: 7/23/16

mud | fine sand | med sand | coarse sand | pebbles | roots | wood frag | shells | burrows | bedding | contact

start at: 2 m

avg. grain size (gravel, v. coarse, coarse, medium, fine, v. fine, silt, clay):
mineralogy: texture (org.-rich; peaty; shelly; sandy, muddy sand, sandy mud, mud):
sorting (well, medium, poor):
structures: bedding (type, size, configuration, location), bioturbation (type, size, abundance, location)
components: shell, organic material (type, condition, abundance, size)

page: of

log	color		other/comments
0		1.81 - 2.30 fine sand w/ visable quartz and dark minerals crushed shell fragments	
10	5Y 4/1 dark gray	muddy lense @ 2.09 m	
20			
30	5Y 4/1 dark gray	2.30 - 2.36 very large ~6 cm wooden branch some mud associated w/ but mainly fine sand	
40	GLEY1 4/N dark grey	2.36 - 2.98 fine - medium sand w/ visable quartz and dark minerals med/fine	
50		2.43 & 2.45 sample ~1cm wide muddy lenses	
60		larger crushed shells in the upper 30cm.	
70		smaller and fewer farther down.	
80			
90		fine/med	
100			

CORE DESCRIPTION SHEET

Core ID: 2B | Core Length: 3.65m | Describer: Matt Kestner | Comments:

Location: Waties Island | Core Depth: | Date: 2/23/16

mud | fine sand | med sand | coarse sand | pebbles | roots | wood frag | shells | burrows | bedding | contact

start at: 3 m

avg. grain size (gravel, v. coarse, coarse, medium, fine, v. fine, silt, clay);
mineralogy; texture (org.-rich; peaty; shelly; sandy, muddy sand, sandy mud, mud);
sorting (well, medium, poor);
structures: bedding (type, size, configuration, location), bioturbation (type, size, abundance, location)
components: shell, organic material (type, condition, abundance, size)

page: of

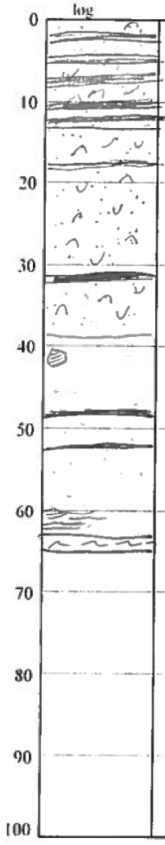

log	color		other/comments
	5Y 5/1 gray 5Y 2.5/1 black	2.98 – 3.13 Alternating muddy sand (dark grey) and v. fine sand layers ~ 0.5cm to 1cm thickness crushed shell fragments throughout.	
	5Y 6/1 gray	3.13 – 3.37 Well sorted fine to med sand visable quartz and dark minerals crushed shell fragments	
		3.18 1cm thick dark gray [illegible] sand 3.31 1cm thick mud [illegible]	
		3.37 – 3.64 fine to med sand visable quartz and dark minerals crushed shell fragments 3.40 – coquina shell? bivalve	
		3.52, 3.49 1cm thick dark grey muddier layers?	
		3.60 – 3.62 Brown / black muddy woody streaks (organics)	
	5Y 2.5/1 Black	3.64 – 3.65 1cm thick muddy v. fine sand	

CORE DESCRIPTION SHEET

Core ID: 3A
Core Length: 3.61 m
Describer: Matt Kestner
Comments:
Location: Wallops Island
Core Depth:
Date: 2/17/2016

mud – fine sand : med sand : coarse sand : pebbles : roots : wood frag : shells : burrows : bedding : contact

start at: 0 m

avg. grain size (gravel, v. coarse, coarse, medium, fine, v. fine, silt, clay):
mineralogy; texture (org.-rich; peaty; shelly; sandy, muddy sand, sandy mud, mud);
sorting (well, medium, poor);
structures: bedding (type, size, configuration, location), bioturbation (type, size, abundance, location)
components: shell, organic material (type, condition, abundance, size)

page: of

log	color		other/comments
0 – 10 – 20 – 30	2.5Y 5/1 gray	0.00 – 0.34 m: Well sorted fine grained sand, quartz grains and dark mineral fragments a few crushed shells 1 cm Eastern Mud Snail Ilyanassa Obsoleta very common on intertidal mud	
40 – 50	2.5Y 2.5/1 Black	0.34 – 0.55 m: Muddy fine sand to silty sand, with a few small roots	
60 – 70 – 80 – 90 – 100	5Y 4/1 dark gray	0.55 – 1.05 m: fine grained sand w/ quartz grains and dark mineral fragments. Has a few darker muddy streaks, flaser bedding?	

CORE DESCRIPTION SHEET

Core ID: 3A
Core Length: 3.61 m
Describer: Matt Kestner
Comments:

Location: Waties Island
Core Depth:
Date: 2/23/2016

mud fine sand med sand coarse sand pebbles roots wood frag shells burrows bedding contact

start at: 1 m

avg. grain size (gravel, v. coarse, coarse, medium, fine, v. fine, silt, clay):
mineralogy; texture (org.-rich; peaty; shelly; sandy, muddy sand, sandy mud, mud):
sorting (well, medium, poor):
structures: bedding (type, size, configuration, location), bioturbation (type, size, abundance, location)
components: shell, organic material (type, condition, abundance, size)

page: of

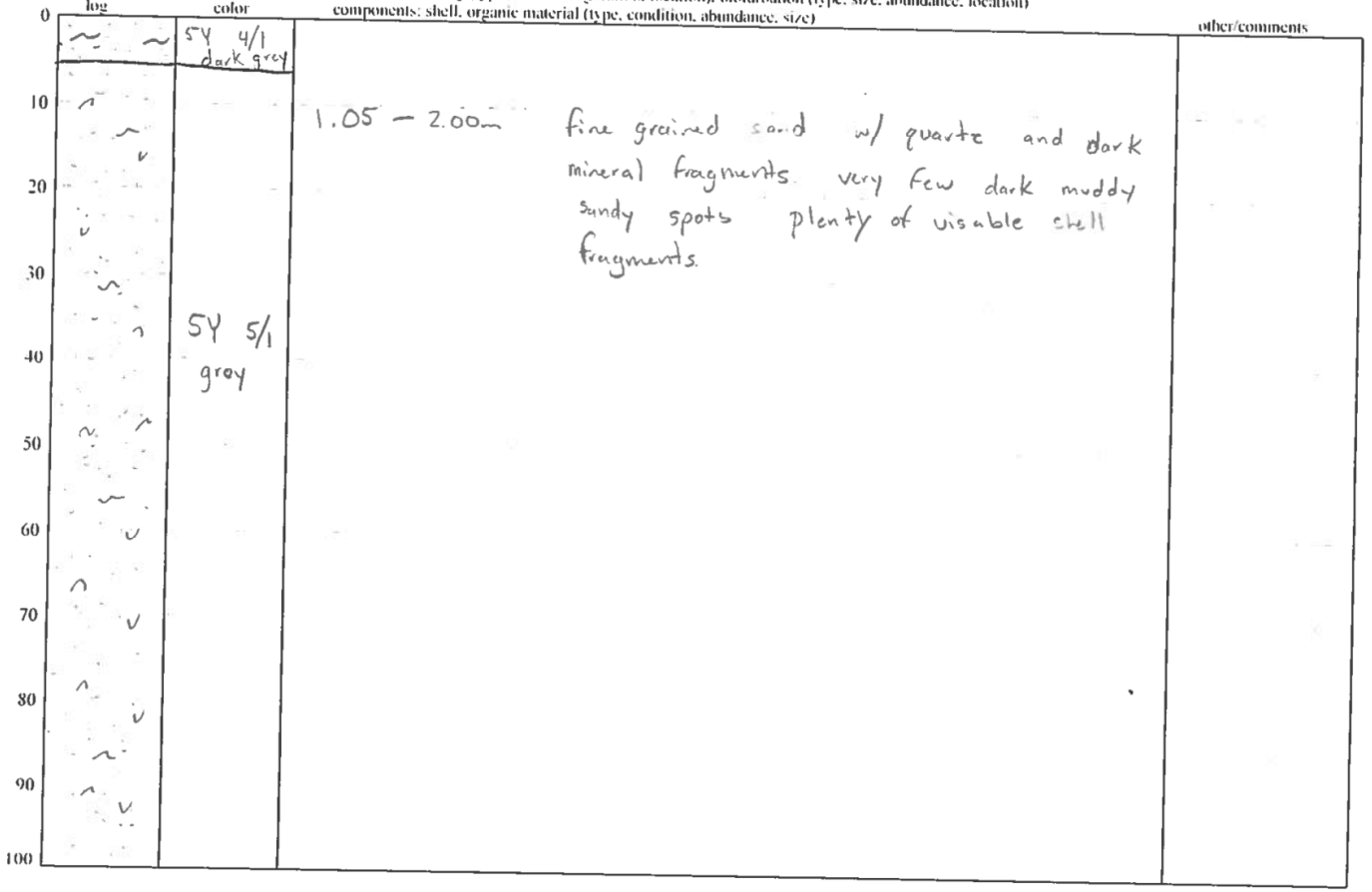

CORE DESCRIPTION SHEET

Core ID: 3B | Core Length: 3.61 m | Describer: Matt Kestner | Comments:

Location: Watie's Island | Core Depth: | Date: 2/23/2016

mud | fine sand | med sand | coarse sand | pebbles | roots | wood frag | shells | burrows | bedding | contact

start at: 2 m

avg. grain size (gravel, v. coarse, coarse, medium, fine, v. fine, silt, clay):
mineralogy; texture (org.-rich; peaty; shelly; sandy, muddy sand, sandy mud, mud):
sorting (well, medium, poor):
structures: bedding (type, size, configuration, location), bioturbation (type, size, abundance, location)
components: shell, organic material (type, condition, abundance, size)

page: of

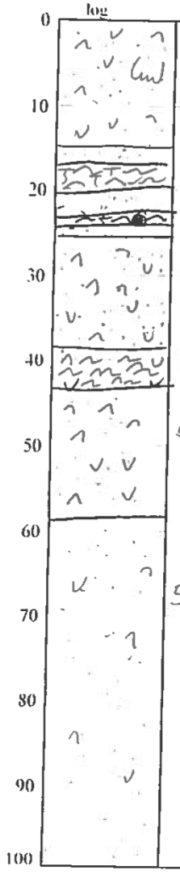

		other/comments
2.00 - 2.14 m	very fine to fine grained sand visable quartz grains and dark minerals lots of shell fragments (visable coquina shells)	
	gradational/ Sharp contact 1 cm black shell fragment severley weathered.	
2.14 - 2.25 m	Inter mixed / layered black muddy silt and very fine gray sand w/ shell fragments mud contains roots and woody fragments organic	sulfur smell
2.25 - 2.38 m	fine sand w/ visable quartz and dark mineral fragments w/ plenty of shell fragments	
2.38 - 2.42 m	Sharp contact sandy mud w/ large shell fragments bivalve (coquina?)	
2.42 - 2.58 m	fine to medium sand w/ visable quartz grains and dark minerals w/ larger shell fragments some darker muddy streaks	
2.58 - 3.00	Massive well worked fine grained sand w/ visable quartz and dark mineral's few crushed shell fragments Sulfury smell	

CORE DESCRIPTION SHEET

Core ID: 3B Core Length: 3.61 m Describer: Matt Kestner Comments:

Location: Watts Island Core Depth: Date: 2/23/2016

mud fine sand med sand coarse sand pebbles roots wood frag shells burrows bedding contact

start at: 3 m page: of

avg. grain size (gravel, v. coarse, coarse, medium, fine, v. fine, silt, clay):
mineralogy: texture (org.-rich; peaty; shelly; sandy, muddy sand, sandy mud, mud):
sorting (well, medium, poor):
structures: bedding (type, size, configuration, location), bioturbation (type, size, abundance, location)
components: shell, organic material (type, condition, abundance, size)

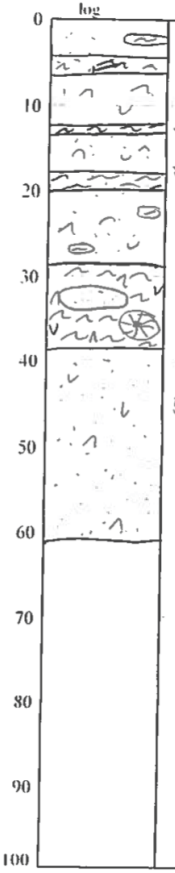

		other/comments
3.00 – 3.29 m	fine grained sand w/ quartz and dark mineral fragments, few shell fragments	
3.02	muddy sandy lense	
3.04 – 3.06	dark gray muddy sandy layer w/ decomposed woody fragments	
3.13 3.18 – 3.20	dark gray muddy sandy layers	
3.23 3.26	muddy sand lenses	
3.29 – 3.38 m	Sharp contact Dark black organic rich mud with large 2cm thick weathered wood fragment, smaller woody fragments sand lense 3.33 – 3.34 fine grained gray sand clean some shell fragments	
3.38 – 3.61	sharp upper contact fine grained sand w/ quartz and dark mineral fragments minimal crushed shell fragments.	

CORE DESCRIPTION SHEET

Core ID: 4A | Core Length: 3.23m | Describer: Matt Kestner | Comments:

Location: Waties Island | Core Depth: | Date: 2/23/16

mud | fine sand | med sand | coarse sand | pebbles | roots | wood frag | shells | burrows | bedding | contact

start at: 0 m

avg. grain size (gravel, v. coarse, coarse, medium, fine, v. fine, silt, clay);
mineralogy; texture (org.-rich; peaty; shelly; sandy, muddy sand, sandy mud, mud);
sorting (well, medium, poor);
structures: bedding (type, size, configuration, location), bioturbation (type, size, abundance, location)
components: shell, organic material (type, condition, abundance, size)

page: of

	log	color		other/comments
0		5Y 5/2	0.00- 0.29m fine sand quarte grains, dark minerals some black grain patches.	
10		Olive gray		
20				
30		5Y 2.5/1 black	0.29-0.39 fine sand black organic rich? lots dark minerals	
40		5Y 4/1 dark gray	0.39-0.57 fine sand dark minerals / quarte grains 2 whole shells some shell fragments. Eastern Mudsnail Ilyanassa obsoleta some bivalve broken	
50				
60		5Y 2.5/1 Black	0.57- 1.15 grodational contact	more fine sand ↓ more mud
70		5Y 4/1 dark gray	0.57- 0.80 intermitten / mixed fine sand and mud: mix sand. few small roots	
80		5Y 2.5/1	0.80- 1.03 organic rich black marsh mud sulfur smell roots oxidized	mainly mud w/ less sand
90				
100				

CORE DESCRIPTION SHEET

Core ID: 4A | Core Length: 3.23m | Describer: Matt Kestner | Comments:

Location: Waties Island | Core Depth: | Date: 2/23/16

mud | fine sand | med sand | coarse sand | pebbles | roots | wood frag | shells | burrows | bedding | contact

start at: 1 m

avg. grain size (gravel, v. coarse, coarse, medium, fine, v. fine, silt, clay):
mineralogy; texture (org.-rich; peaty; shelly; sandy, muddy sand, sandy mud, mud):
sorting (well, medium, poor):
structures: bedding (type, size, configuration, location), bioturbation (type, size, abundance, location)
components; shell, organic material (type, condition, abundance, size)

page: __ of __

log	color		other/comments
0	5Y 25/1 black	1.03 - 1.15 fine sand / mud intermix large 7½ cm Eastern Oyster crossostrea virginica Sharp contact	
20	5Y 4/1 dark gray	1.15 - 1.76 fine sand w/ quartz grains and dark minerals visable some crushed shells some random wood pieces	
30		1.36 - 1.38 darker gray transition	
40	5Y 5/1 gray		
50		1.60 - 1.61 Muddy sand layer v dark gray to black	
60			
70			
80	5Y 4/1 dark gray 5Y 5/1 gray	1.76 - 1.88 intermitten layering dark muddy layers with fine sand gray layers.	
90	5Y 5/1 gray	1.88 - 1.96 fine sand well worked (clean) quartz grains dark minerals 1.96 - 1.98 - Muddy layer w/ brown woody fibers.	
100	5Y 2.5/1 5Y 5/1	1.98 - 2.00 fine sand well worked quartz grains dark minerals	

CORE DESCRIPTION SHEET

Core ID: 4B Core Length: 3.23 m Describer: Matt Kestner Comments:

Location: Watkins Island Core Depth: Date: 2/24/16

mud fine sand med sand coarse sand pebbles roots wood frag shells burrows bedding contact

start at: 2 m

avg. grain size (gravel, v. coarse, coarse, medium, fine, v. fine, silt, clay):
mineralogy: texture (org.-rich; peaty; shelly; sandy, muddy sand, sandy mud, mud):
sorting (well, medium, poor):
structures: bedding (type, size, configuration, location), bioturbation (type, size, abundance, location)
components: shell, organic material (type, condition, abundance, size)

page: of

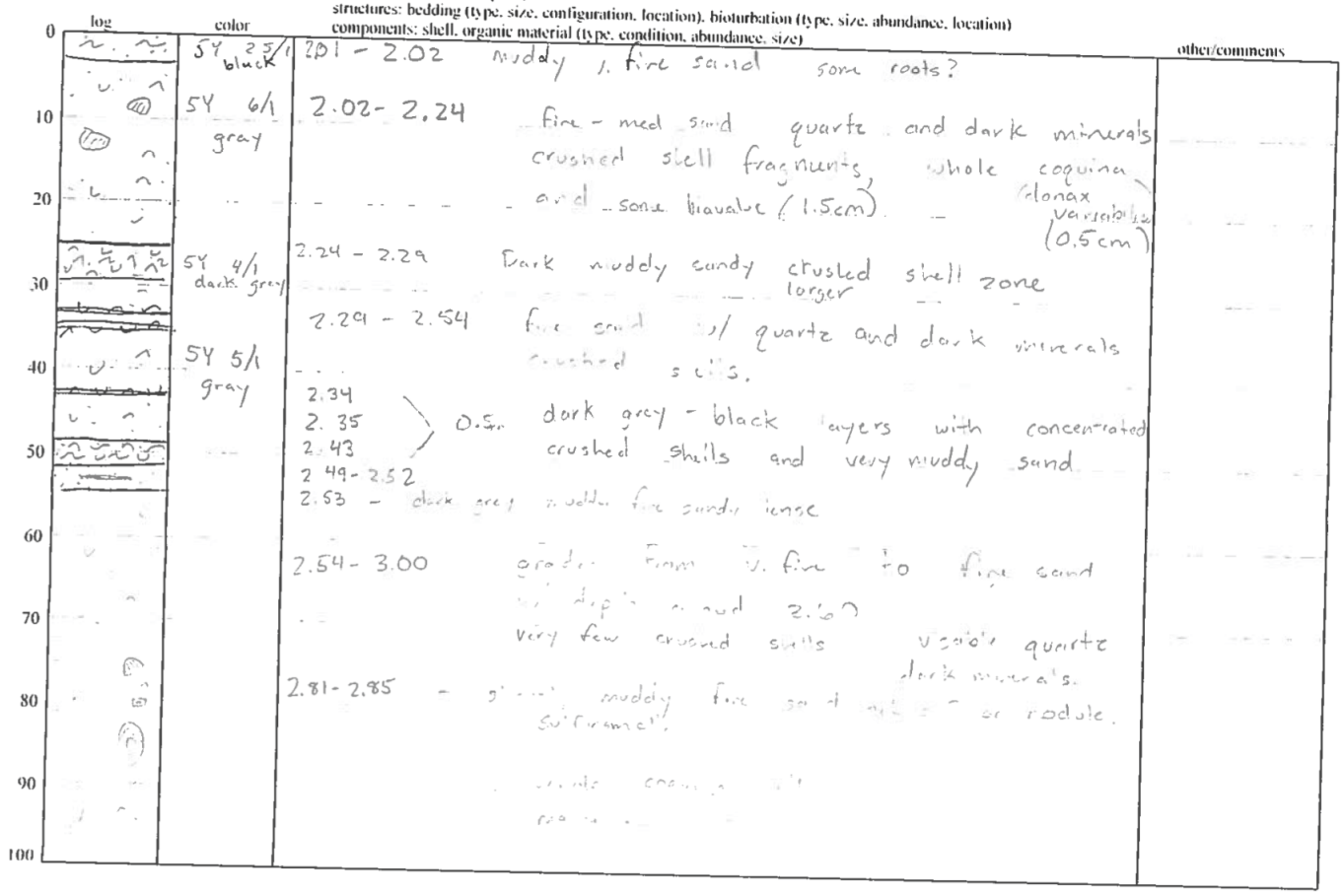

CORE DESCRIPTION SHEET

Core ID: 4B
Core Length: 3.23m
Describer: Matt Kestner
Comments:
Location: Watts Island
Core Depth:
Date: 2/24/2016

mud fine sand med sand coarse sand pebbles roots wood frag shells burrows bedding contact

start at: 3 m

avg. grain size (gravel, v. coarse, coarse, medium, fine, v. fine, silt, clay):
mineralogy; texture (org.-rich; peaty; shelly; sandy, muddy sand, sandy mud, mud);
sorting (well, medium, poor);
structures: bedding (type, size, configuration, location), bioturbation (type, size, abundance, location)
components: shell, organic material (type, condition, abundance, size)

page: of

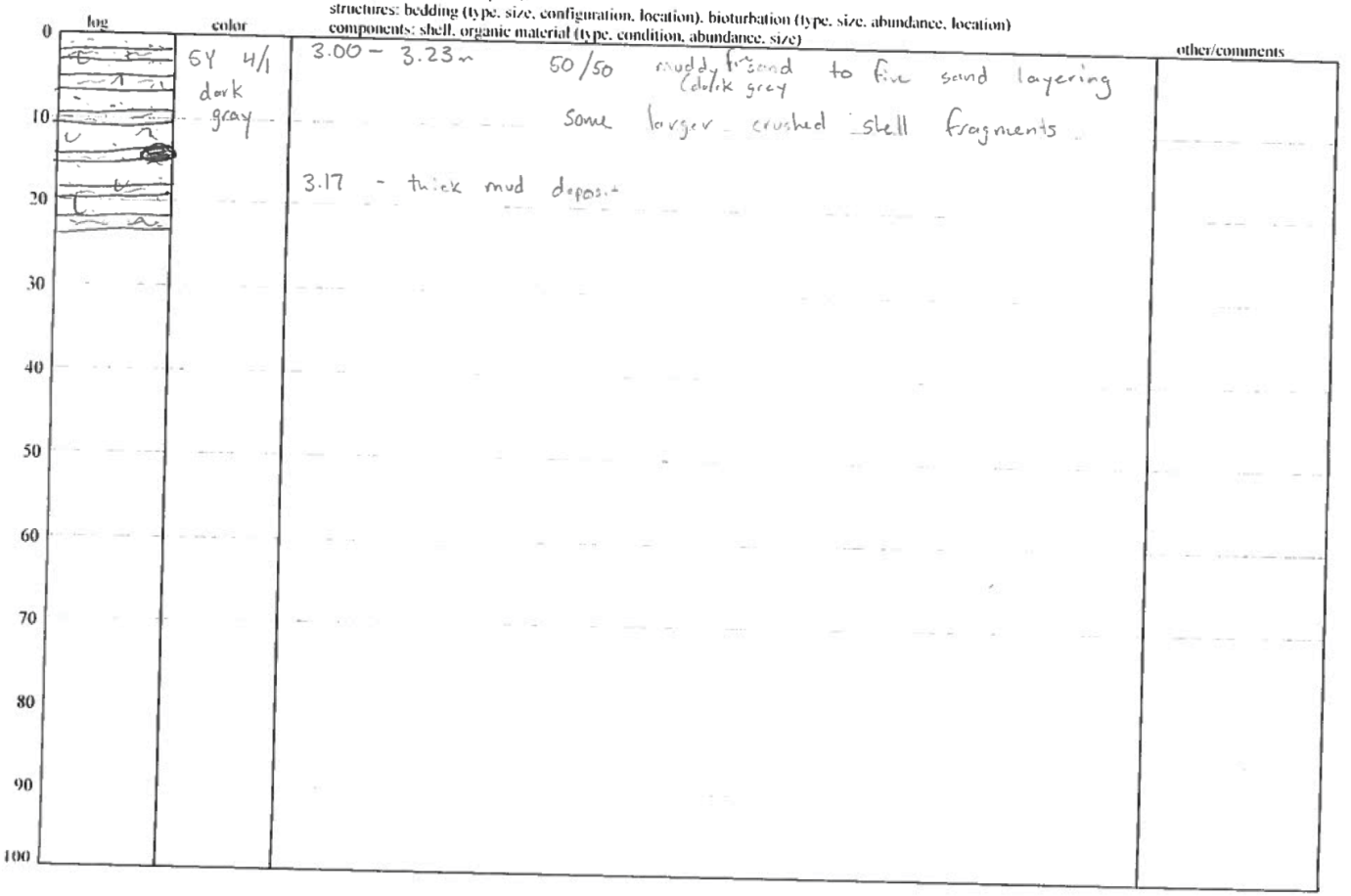

CORE DESCRIPTION SHEET

Core ID: 5A Core Length: 3.78 m Describer: Matt Kestner Comments:

Location: Waties Island Marsh Core Depth: _____ Date: 2/17/2016

mud fine sand med sand coarse sand pebbles roots wood frag shells burrows bedding contact

start at: 0 m

avg. grain size (gravel, v. coarse, coarse, medium, fine, v. fine, silt, clay):
mineralogy: texture (org.-rich; peaty; shelly; sandy, muddy sand, sandy mud, mud):
sorting (well, medium, poor):
structures: bedding (type, size, configuration, location), bioturbation (type, size, abundance, location)
components: shell, organic material (type, condition, abundance, size)

page: of

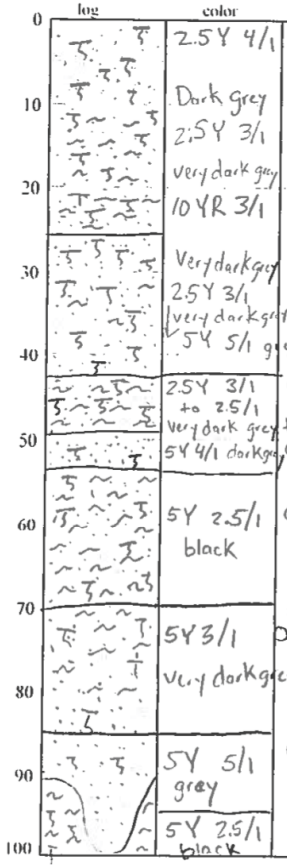

0-0.1 Organic rich, fine to very fine sand; with plenty of spartina remnants, orange and black patches, due to decomposing and oxidation small roots

0.1-0.2 Organic rich, fine sandy mud to muddy sand; with small roots, orange and black patches

0.2-0.3 gradational contact @ 0.25. 0.2-0.25 Organic rich muddy sand with small roots, orange and black patches 0.25-.30 Organic rich fine to very fine sand, spartina remnants orange and black patches

0.3-0.42 spartina remnants small roots organic rich muddy fine sand grading to fine sand sharp contact @ 0.42 less orange and black redox spots

0.42-0.49 Very fine muddy sand / sandy mud, small roots, sharp contact top and bottom.

0.49-0.53 fine sand, small roots, sharp contact top and bottom w/ black minerals

0.53-0.70 muddy sand large and small roots (spartina) Organic rich

0.70-0.84 muddy sand grading to fine sand less roots and organic matter

0.84-1.00 Massive irregular contact. minimal root fragments Very fine to fine sand w/ dark mineral fragments extending into a clay/silt mud (no sand) w/ some root fragments organic rich

other/comments

Surface

Fine sand grading to muddy sand

0.25

CORE DESCRIPTION SHEET

Core ID: 5A Core Length: 3.78m Describer: Matt Kestner Comments:

Location: Waties Island Marsh Core Depth: _____ Date: 2/17/2016

mud fine sand med sand coarse sand pebbles roots wood frag shells burrows bedding contact

start at: 1 m

avg. grain size (gravel, v. coarse, coarse, medium, fine, v. fine, silt, clay):
mineralogy; texture (org.-rich; peaty; shelly; sandy, muddy sand, sandy mud, mud):
sorting (well, medium, poor):
structures: bedding (type, size, configuration, location), bioturbation (type, size, abundance, location)
components: shell, organic material (type, condition, abundance, size)

page: of

log	color		other/comments
0–10	5Y 2.5/1 Black	1.00 - 1.20 Gradual Grading from clay/silty mud to a sandy mud with minimal root fragments very fine	
20–30	5Y 3/1 very dark grey	1.20 - 1.40 Gradual Gradation from sand mud to a very fine to fine sand w/ minimal mud. No organics or roots. black minerals are visable at bottom.	
40–60	5Y 4/1 dark grey	1.40 - 1.65 Massive very fine to fine sand w/ crushed shell fragments and visable black minerals/micas	
70–80	5Y 5/1 grey	1.65 - 1.85 Massive fine sand w/ crushed shell fragments and visable black minerals and mica	
90–100	5Y 5/1 grey	1.85 - 2.00 Alternating dark and light layers of fine sand w/ abundance of crushed shells Dark layers are a muddy fine sand (flaser bedding?)	

CORE DESCRIPTION SHEET

Core ID: 5B Core Length: 3.78 m Describer: Matt Kestner Comments:

Location: Waties Island Core Depth: - Date: 2/17/2016

mud fine sand med sand coarse sand pebbles roots wood frag shells burrows bedding contact

start at: 2 m

avg. grain size (gravel, v. coarse, coarse, medium, fine, v. fine, silt, clay):
mineralogy: texture (org.-rich; peaty; shelly; sandy, muddy sand, sandy mud, mud):
sorting (well, medium, poor):
structures: bedding (type, size, configuration, location), bioturbation (type, size, abundance, location)
components: shell, organic material (type, condition, abundance, size)

page: of

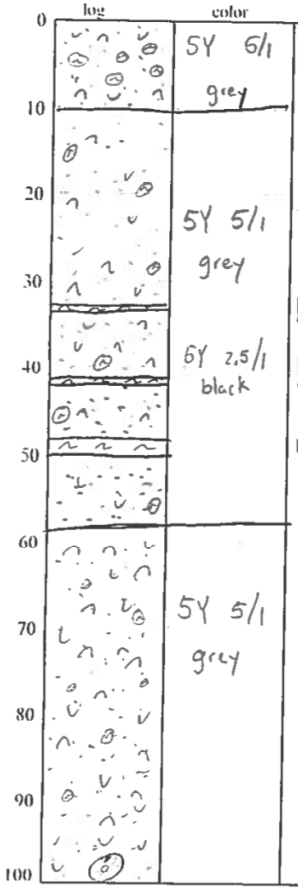

other/comments

2.00 – 2.10 Fine sand w/ an abundance of crushed shell fragments w/ visable dark minerals + mica. Has orbitals or pockets of dark muddy sand ≈ 0.5 cm.

2.10 – 2.58 Massive fine grained sand with some crushed shell fragments visable quartz grains, dark minerals, and mica

½ cm

Muddy fine sand bands ½ cm

Some intermitten dark muddy patches >0.25 cm

1cm thick

2.58 – 3.02 Fine to Medium sand medium grained quartz visable dark minerals and mica fragments large crushed shell fragments to whole bivalves (Coquina) (~1cm)

A few Splotchy darker muddy orbitals.

@ 2.97 – 3.01 large circular dark muddy sand deposit.

CORE DESCRIPTION SHEET

Core ID: 5B Core Length: 3.78m Describer: Matt Kestner Comments:

Location: Wallies Island Core Depth: Date: 2/17/2016

mud fine sand med sand coarse sand pebbles roots wood frag shells burrows bedding contact

start at: 3 m

avg. grain size (gravel, v. coarse, coarse, medium, fine, v. fine, silt, clay):
mineralogy: texture (org.-rich: peaty: shelly: sandy, muddy sand, sandy mud, mud):
sorting (well, medium, poor):
structures: bedding (type, size, configuration, location), bioturbation (type, size, abundance, location)
components: shell, organic material (type, condition, abundance, size)

page: of

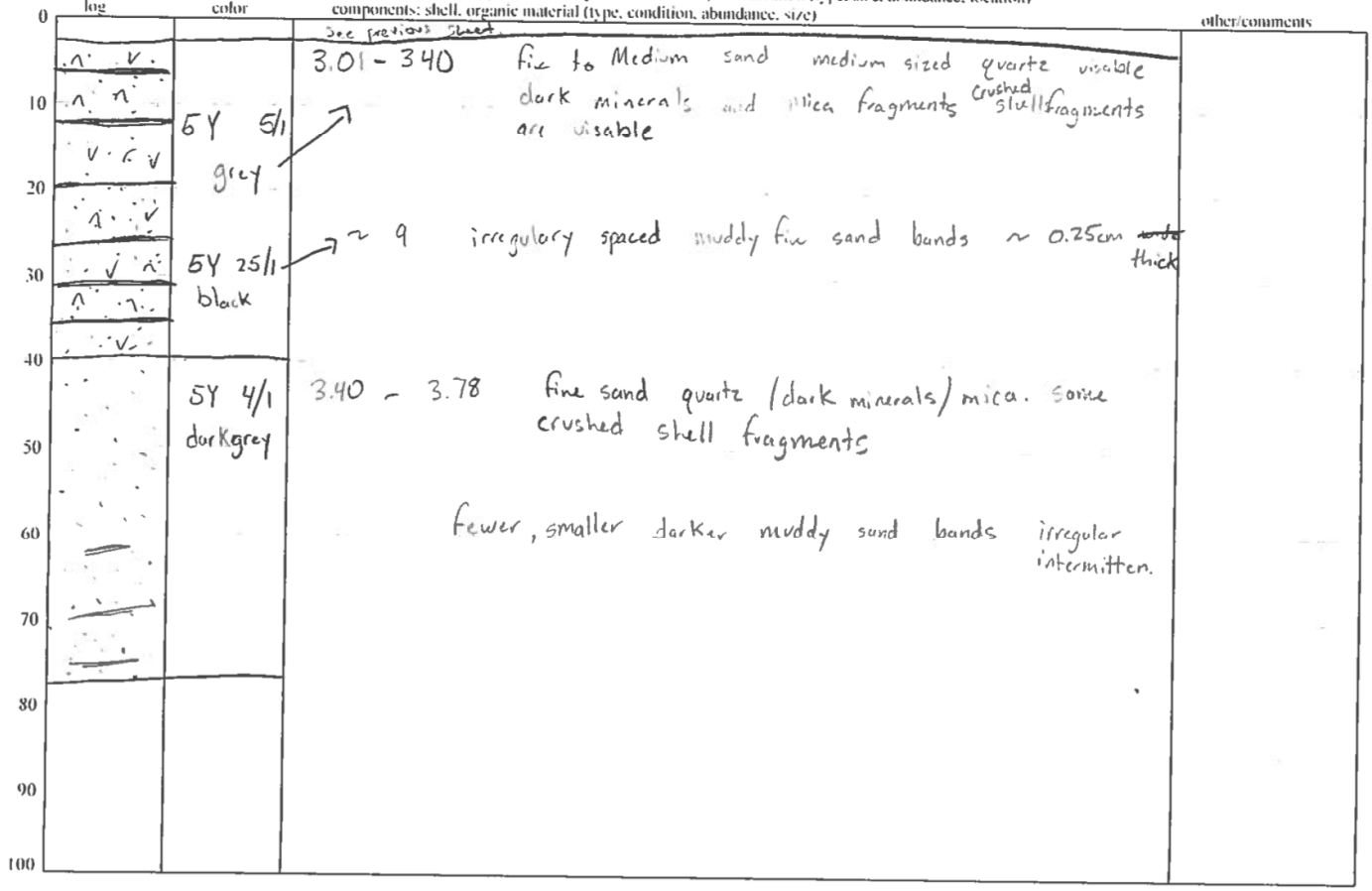

Appendix C

Hand Auger sediment samples:

The following table and formulas provide a comprehensive list of sediment analysis. Hand Auger samples were collected for the ERT transect along the creek channel. Laboratory analysis of the sediment samples was carried out in Coastal Carolina University's Sediment Laboratory. Coastal Carolina University's Laser Particle Size Analyzer and the supplementary software were used to calculate Grain Size, Sorting, Kurtosis, and Skewness. Analysis of bulk density, water content, and porosity where done with simple lab experiments.

The fully saturated sediment samples were massed, and then dried, to measure the amount of water lost. To calculate the bulk density of the sediment, a graduated cylinder was filled to a specific volume, while a known amount of dry sediment was placed in the cylinder. The mass of the dry sediment added to the graduated cylinder, divided by the amount of water displaced, gave the bulk density of the sediment sample. The density of fresh or salt water was used to give a range of porosity. The amount of water lost in the initial drying process, divided by the density of salt water or fresh water, gave the volume of the void space in the sediment. The volume of the sediment was calculated by using the mass of the dry sediment divided by the density of each sediment sample. From there, the calculation is the volume of the voids divided by the total volume to give the porosity of each sediment sample. The porosity can be used to calculate a realistic volume of water entering or leaving the creek sediment along the transect site. Gaining a robust

understanding of the sediment surrounding the creek channel can validate the interpretation of the ERT data.

Hand Auger Sediment Analysis								
			Water Density (1.0 or 1.035 g/ml)					
Sediment Sample	**Water Content (%)**	**Bulk Density (g/ml)**	**Porosity (%)**	**Porosity (%)**	**Average Grain Size (Φ)**	**Skewness**	**Kurtosis**	**Sorting**
1A	15.11	3.88	0.41	0.40	2.87	0.27	2.07	2.27
1B	21.83	2.72	0.43	0.42	2.53	0.25	1.17	2.40
1C	22.26	2.44	0.41	0.40	2.37	0.32	2.70	0.98
1D	18.25	2.62	0.37	0.36	2.30	0.30	2.65	0.93
1E	27.81	2.62	0.50	0.49	2.91	0.40	1.55	2.19
1F	29.48	2.13	0.47	0.46	3.61	0.53	0.86	2.40
1G	26.35	2.51	0.47	0.46	3.40	0.60	1.35	2.14
1H	25.77	1.82	0.47	0.46	2.94	0.47	2.41	1.91
1I	28.50	2.91	0.54	0.53	3.33	0.57	1.23	2.20
1J	26.81	2.61	0.49	0.48	3.56	0.52	1.00	2.41
1K	25.41	2.31	0.44	0.43	3.83	0.66	0.93	2.19
1L	24.89	2.39	0.44	0.43	3.20	0.64	2.65	1.68
1M	26.29	2.26	0.45	0.44	3.67	0.66	1.42	2.13
2A	26.94	2.10	0.44	0.43	3.18	0.56	1.45	1.51
2B	30.20	2.33	0.50	0.49	3.28	0.55	1.39	1.57
2C	33.79	1.94	0.50	0.49	3.62	0.52	1.14	1.97
2D	29.93	1.48	0.39	0.38	3.74	0.54	1.04	2.09
2E	28.68	1.88	0.43	0.42	3.54	0.57	1.17	2.03
2F	25.60	2.42	0.45	0.45	3.33	0.56	1.47	1.90
3A	23.24	2.63	0.44	0.43	2.71	0.46	2.36	0.94
3B	22.55	2.39	0.41	0.40	2.59	0.38	2.35	0.81
3C	22.18	2.69	0.41	0.40	2.90	0.54	2.14	1.36
3D	24.02	2.02	0.39	0.38	3.14	0.60	2.65	1.77
3E	20.28	2.87	0.42	0.41	2.82	0.51	2.28	1.16
3F	22.34	2.61	0.43	0.42	2.55	0.31	1.95	0.73
4A	24.26	2.46	0.44	0.43	2.68	0.38	2.42	0.90
4B	26.31	4.50	0.47	0.46	2.63	0.39	2.48	0.91
4C	23.10	3.14	0.49	0.48	2.80	0.51	2.35	1.13
4D	22.40	2.97	0.46	0.45	2.64	0.44	2.42	1.01
4E	22.77	2.64	0.44	0.43	2.71	0.47	2.45	1.07
5A	26.81	2.55	0.48	0.47	2.85	0.51	2.38	1.09
5B	28.71	2.07	0.45	0.45	2.89	0.56	2.24	1.19
5C	25.44	2.27	0.44	0.43	2.75	0.52	2.31	1.14
5D	25.97	2.26	0.44	0.43	3.49	0.69	1.32	1.76
5E	44.02	2.23	0.64	0.63	3.22	0.63	1.83	1.42

5F	26.47	2.29	0.45	0.44	2.93	0.57	2.46	1.17
5G	25.30	2.25	0.43	0.42	3.23	0.60	1.83	1.56
5H	22.74	2.30	0.40	0.40	2.57	0.12	1.93	2.38
Averages	25.60	2.49	0.45	0.44	3.03	0.49	1.89	1.59
					Very Fine Grained	Strongly Fine Skewed	Very Leptokurtic	Poorly Sorted